EFFECT OF CARBON FIBER REINFORCED POLYMER RETROFITTING ON RECYCLED BRICK AGGREGATE CONCRETE COLUMN

MD. MUNIRUZZAMAN

M. Sc. ENGINEERING THESIS

DEPARTMENT OF CIVIL ENGINEERING
MILITARY INSTITUTE OF SCIENCE AND TECHNOLOGY
DHAKA, BANGLADESH

DECEMBER 2023

EFFECT OF CARBON FIBER REINFORCED POLYMER RETROFITTING ON RECYCLED BRICK AGGREGATE CONCRETE COLUMN

MD. MUNIRUZZAMAN (SN. 0420110001)

A Thesis Submitted in Partial Fulfillment of the Requirements for the Degree of Master of Science in Civil Engineering

DEPARTMENT OF CIVIL ENGINEERING
MILITARY INSTITUTE OF SCIENCE AND TECHNOLOGY
DHAKA, BANGLADESH

DECEMBER 2023

EFFECT OF CARBON FIBER REINFORCED POLYMER
RETROFITTING ON RECYCLED BRICK
AGGREGATE CONCRETE COLUMN

M.Sc. Engineering Thesis

By

MD. MUNIRUZZAMAN (SN. 0420110001)

Approved as to style and content by the Board of Examination on 03 December 2023:

Lt Col Md Jahidul Islam, PhD, Engrs Associate Professor of Civil Engineering MIST, Dhaka	Chairman (Supervisor) Board of Examination
Dr Raquib Ahsan Professor of Civil Engineering BUET, Dhaka	Member (External) Board of Examination
Dr Tanvir Mustafy Associate Professor of Civil Engineering MIST, Dhaka	Member Examination
Col Nasir Uddin Ahmed Dean of Civil Engineering Faculty MIST, Dhaka	Dean, Faculty of CE, MIST Member (Ex-officio)

Department of Civil Engineering MIST, Dhaka

EFFECT OF CARBON FIBER REINFORCED POLYMER RETROFITTING ON RECYCLED BRICK AGGREGATE CONCRETE COLUMN

DECLARATION

I hereby declare that the study reported in this thesis entitled as above is my own original work and has not been submitted before anywhere for any degree or other purposes. Further, I certify that the intellectual content of this thesis is the product of my own work and that all the assistance received in preparing this thesis and sources have been acknowledged and cited in the reference section.

____

Md. Muniruzzaman

Department of Civil Engineering MIST, Dhaka

EFFECT OF CARBON FIBER REINFORCED POLYMER RETROFITTING ON RECYCLED BRICK AGGREGATE CONCRETE COLUMN

A Thesis

By

Md. Muniruzzaman

DEDICATION

Dedicated to my family for supporting and
Encouraging me to believe in myself.

ABSTRACT

Effect of Carbon Fiber Reinforced Polymer Retrofitting on
Recycled Brick Aggregate Concrete Column

Most old structures in Bangladesh are found to be made of poor-quality materials, low-strength concrete (about 17 MPa), and brick aggregate because of the acute scarcity of natural stones in the early days. Moreover, some of them were constructed without proper compliance with the existing codes, and the updated building code demands a more stringent design philosophy. Hence, strengthening the structures to comply with the recent design guidelines becomes an issue of utmost significance. The study examined the feasibility of using CFRP jacketing to retrofit inferior-quality columns in Bangladesh.

In this study, one-third scale columns made of low-strength recycled brick aggregate concrete (17 MPa and 10 MPa), with square and rectangular shapes having dimensions of 150 mm x 150 mm x 950 mm (kl/r = 21.94, l/h = 6.33) and 150 mm x 225 mm x 950 mm (kl/r = 14.63, l/h = 4.22), respectively are tested. Columns are evaluated to find out the effect on axial capacity, moment capacity, dilation, ductility, and toughness with discrete and continuous CFRP confinement under eccentric loading. Columns of similar sizes with no CFRP confinement are also tested under concentric and eccentric loading to compare their behavior. One square column having no transverse reinforcement was tested to observe the effect of confinement by tie bars.

The results indicate that CFRP wrapping enhanced the axial capacity, moment capacity, deformation responses, ductility, and toughness of the columns. It is observed that the discrete and continuous wrapping increased the axial capacity of a column by at least 27% and 49%, respectively, and the corresponding moment capacity increased by at least 32% and 54%. The confined compressive strength (f'_{cc}) of the concrete cylinders increased by a minimum of 41% and 91%, respectively, due to adding one and two CFRP layers. The ACI 440.2R-17 code is not recommended for FRP systems for concrete with compressive strength (f'_c) less than 17 MPa, but a minimum of 65% higher compressive strength is found for a lower strength (10 MPa) concrete. Thus, the ACI 440.2R-17 code can be conservatively used to predict the capacity of a CFRP-confined recycled brick aggregate concrete column.

সারসংক্ষেপ

Effect of Carbon Fiber Reinforced Polymer Retrofitting on Recycled Brick Aggregate Concrete Column

বাংলাদেশের অধিকাংশ পুরাতন কাঠামো নিম্ন-মানের উপকরণ, নিম্ন-শক্তির কংক্রিট (প্রায় 17 MPa) এবং ইটের সমষ্টি দ্বারা তৈরি বলে পাওয়া যায় কারণ আদিকালে প্রাকৃতিক পাথরের তীব্র ঘাটতি ছিল। তদুপরি, তাদের মধ্যে কিছু বিদ্যমান কোডগুলির যথাযথ সম্মতি ছাড়াই নির্মিত হয়েছিল এবং আপডেট করা বিল্ডিং কোডটি আরও কঠোর নকশা দর্শনের দাবি করে। তাই, সাম্প্রতিক নকশা নির্দেশিকা মেনে চলার জন্য কাঠামোকে শক্তিশালী করা অত্যন্ত তাৎপর্যপূর্ণ একটি বিষয় হয়ে দাঁড়ায়। গবেষণায় বাংলাদেশে নিম্নমানের কলামগুলিকে পুনরুদ্ধার করতে CFRP জ্যাকেটিং ব্যবহারের সম্ভাব্যতা পরীক্ষা করা হয়েছে।

এই সমীক্ষায়, কম-শক্তির পুনর্ব্যবহৃত ইটের সমষ্টিগত কংক্রিট (17 MPa এবং 10 MPa) দিয়ে তৈরি এক-তৃতীয়াংশ স্কেলের কলামগুলি বর্গাকার এবং আয়তক্ষেত্রাকার আকারের যার মাত্রা ১৫০ মিমি x ১৫০ মিমি x ৯৫০ মিমি (kl/r = 21.94, l/h = 6.33) এবং ১৫০ মিমি x ২২৫ মিমি x ৯৫০ মিমি (kl/r = 14.63, l/h = 4.22), যথাক্রমে পরীক্ষা করা হয়। অক্ষীয় ক্ষমতা, মুহূর্ত ক্ষমতা (moment capacity), প্রসারণ, নমনীয়তা এবং বিচ্ছিন্ন এবং ক্রমাগত CFRP সীমাবদ্ধতার সাথে এককেন্দ্রিক লোডিংয়ের উপর প্রভাব খুঁজে বের করার জন্য কলামগুলি মূল্যায়ন করা হয়। কোন CFRP সীমাবদ্ধতা ছাড়া অনুরূপ আকারের কলামগুলিও তাদের আচরণের তুলনা করতে কেন্দ্রীভূত এবং উদ্ভট (eccentric) লোডিংয়ের অধীনে পরীক্ষা করা হয়। একটি বর্গাকার কলাম যার কোন তির্যক শক্তি বৃদ্ধি নেই তা টাই বার দ্বারা বন্দিত্বের প্রভাব পর্যবেক্ষণ করার জন্য পরীক্ষা করা হয়েছিল।

ফলাফলগুলি ইঙ্গিত দেয় যে CFRP মোড়ানো অক্ষীয় ক্ষমতা, মুহূর্ত ক্ষমতা, বিকৃতি প্রতিক্রিয়া, নমনীয়তা এবং কলামগুলির কঠোরতা (toughness) বৃদ্ধি করেছে। এটি দেখা যায় যে বিচ্ছিন্ন এবং অবিচ্ছিন্ন মোড়কের ফলে একটি কলামের অক্ষীয় ক্ষমতা যথাক্রমে কমপক্ষে ২৭% এবং ৪৯% বৃদ্ধি পেয়েছে এবং সংশ্লিষ্ট মুহূর্ত ক্ষমতা কমপক্ষে ৩২% এবং ৫৪% বৃদ্ধি পেয়েছে। এক এবং দুটি CFRP স্তর যুক্ত করার কারণে কংক্রিট সিলিন্ডারের সীমাবদ্ধ সংকোচন শক্তি ($f'cc$) যথাক্রমে ন্যূনতম ৪১% এবং ৯১% বৃদ্ধি পেয়েছে। ACI 440.2R-17 কোড 17 MPa-এর কম কমপ্রেসিভ শক্তি ($f'c$) কংক্রিটের জন্য FRP সিস্টেমের জন্য সুপারিশ করা হয় না, তবে কম শক্তি (10 MPa) কংক্রিটের জন্য ন্যূনতম ৬৫% বেশি সংকোচন শক্তি পাওয়া যায়। এইভাবে, ACI 440.2R-17 কোডটি রক্ষণশীলভাবে একটি CFRP- সীমাবদ্ধ পুনর্ব্যবহৃত ইটের সমষ্টি কংক্রিট কলামের ক্ষমতার পূর্বাভাস দিতে ব্যবহার করা যেতে পারে।

ACKNOWLEDGEMENTS

First and foremost, I would like to thank Allah (SWT) with the blessings of Whom all the good deeds are fulfilled.

I would like to express my deepest gratitude and most humbly enunciate my sincere appreciation to my supervisor, Lt Col Md Jahidul Islam, Ph.D., Engrs., Associate Professor, Department of Civil Engineering, Military Institute of Science & Technology (MIST), for his constant and acute supervision, continuous encouragement, suggestions, instructions, and compelling discussions. Without his relentless, kind, and diligent perseverance, this thesis would not have been able to be concluded by me alone. I would also like to thank Assistant Professor Md. Shahjalal and Research Assistant Tasnia Ahmed for their advice and assistance needed for the research. I acknowledge the generosity of the Head of the Department for the financial allocation that made this study possible.

I would like to express my gratitude to all the lab assistants of the Civil Engineering Department of MIST for their constant technical access and help, without which it would have been difficult to conduct the experimental work of my study.

Lastly, I am also indebted to the Department of Civil Engineering of MIST for allowing me to conduct the research successfully. I also acknowledge my family members for their loving support and encouragement, and I thank our friends and well-wishers for always supporting and helping me throughout the journey.

TABLE OF CONTENTS

LIST OF FIGURES

LIST OF TABLES

NOTATION

A_c	Cross-sectional area of concrete in compression member
A_e	Cross-sectional area of an effectively confined concrete section
A_g	Gross area of a concrete section
A_{st}	Total area of longitudinal reinforcement
b	Short side dimension of a compression member of prismatic cross-section
C	Distance from extreme compression fiber to the neutral axis
C_E	Environmental reduction factor
D	Diameter of equivalent circular column
d	Distance from extreme compression fiber to centroid of the tension reinforcement
d_i	Distance from centroid of the *i*-th layer of longitudinal steel reinforcement to the geometric centroid of cross-section
E_2	Slope of the linear portion of stress-strain model for FRP-confined concrete
E_c	Modulus of elasticity of concrete
E_f	Tensile modulus of elasticity of CFRP
E_s	Modulus of elasticity of steel
f'_c	Specified compressive strength of concrete
f'_{cc}	Compressive strength of confined concrete
f_{fu}	Design ultimate tensile strength of CFRP
f_l	Maximum confining pressure due to CFRP
f_{si}	Stress in the *i*-th layer of longitudinal steel reinforcement
f_y	Specified yield strength of non-prestressed steel reinforcement
h	Long side cross-sectional dimension of a rectangular compression member
M_n	Nominal bending moment strength
M_{max}	Experimental bending moment capacity

P_n	Nominal axial compressive strength of a concrete section
P_{peak}	Experimental maximum axial load capacity
r_c	Radius of edges of a prismatic cross section confined with CFRP
t_f	Nominal thickness of one ply of FRP reinforcement
y_t	Vertical coordinate within compression region measured from neutral axis position. It corresponds to transition strain ε'_t
Δ	Lateral deflection at the peak load
ε_c	Strain in concrete
ε'_c	Compressive strain of unconfined concrete corresponding to f'_c
ε_{ccu}	Ultimate axial compressive strain of confined concrete corresponding to 0.85f'cc in a lightly confined member or ultimate axial compressive strain of confined concrete corresponding to failure in a heavily confined member
ε_{fe}	Effective strain in CFRP reinforcement attained at failure
ε_{fu}	Ultimate rupture strain of CFRP reinforcement
ε_{sy}	Strain corresponding to yield strength of non-prestressed steel reinforcement
ε'_t	Transition strain in stress-strain curve of CFRP-confined concrete
κ_a	Efficiency factor for CFRP reinforcement in determination of f'_{cc}
κ_b	Efficiency factor for CFRP reinforcement in determination of ε_{ccu}
κ_ε	Efficiency factor equal to 0.55 for CFRP strain to account for the difference between observed rupture strain in confinement and rupture strain determined from tensile tests
ρ_g	Ratio of area of longitudinal steel reinforcement to cross-sectional area of a compression member.
φ	Strength reduction factor
ψ_f	CFRP strength reduction factor

CHAPTER 1
INTRODUCTION

1.1 General

The most recent major earthquake striking the regions of Turkey and Syria caused colossal failures of structures and resulted in the loss of thousands of lives. Previous studies by seismologists revealed that Turkey was at severe risk of earthquakes due to several actively moving tectonic plates (Kelam et al., 2022). In addition, some experts remarked that the age and quality of the building construction caused the structures to be more prone to catastrophic failure during earthquakes. In the context of recent earthquakes, researchers have anticipated that an earthquake of magnitude 8 may hit Bangladesh anytime in the coming years (Momin, 2023). If an earthquake of 7 Mw hits Bangladesh, it would wreak havoc on the entire façade of the country, with the deadliest impacts occurring in those cities that may not have followed the standard building codes (Apu and Das, 2020). Evaluating the past records shows that Bangladesh has already faced tragic losses due to the collapse of the Spectrum Sweater factory (Miller, 2013) and Rana Plaza (Yardley, 2013) in the last 20 years. Therefore, taking necessary precautions to protect the existing structures against the foreseen calamity is essential. With current technological advances, using fiber-reinforced polymer (FRP) composites to retrofit structures is being studied extensively and practiced gradually. FRP jacketing systems were developed as alternatives to traditional external retrofitting methods such as steel plate bonding and steel or concrete column jacketing.

1.2 Background

Most old structures in Bangladesh are found to be made of poor-quality materials, low-strength concrete (about 17 MPa), and brick aggregate because of the acute scarcity of natural stones in the early days. The buildings were constructed without proper compliance with the existing codes, making them vulnerable to natural disasters (Ahmed et al., 2019). Besides, the updated building codes are more stringent with the earthquake-resistant detailing of the structural elements. However, demolishing and reconstructing those structures may not always be financially feasible. Moreover, many of these buildings hold significant cultural and historical value. Instead, strengthening and retrofitting the columns of these structures is more sustainable since it conserves resources and has a lower carbon impact (Jena and Kaewunruen, 2021). As the columns are the essential structural element, retrofitting the columns has become a key priority in recent years (Islam et al., 2016). Brick coarse aggregate is one of Bangladesh's most popular materials for constructing concrete structures. Thus, due to fatigue, creep, and environmental effects, this structure needs strengthening to improve stiffness, strength, ductility, and durability. Furthermore, Bangladesh updated its building code recently. Structures built before 2021 might require retrofitting to meet current code provisions and loading situations if an addition or alteration is made to the existing structure.

Fig. 1.1: Traditional external retrofitting through concrete column jacketing.

Traditional external retrofitting (Fig. 1.1) methods change the column's cross-sectional area, thereby changing the structure's mass and stiffness and reducing the structure's natural period, consequently resulting in higher seismic demands on the structure. In contrast, the FRP system increases the structure's mass very negligibly (Fig. 1.2). It has become widely accepted due to its very high strength-to-weight ratio, improved resistance to fatigue stress, enhanced ductility, high resistance to corrosion, requiring the least maintenance, faster installation, and less space requirement, etc. The coefficient of thermal expansion of FRP is close to that of concrete. Thus, the two materials are compatible, and there are no problems of expansion or shrinkage. The traditional reinforced concrete jacketing requires the occupants to evacuate the residence during the surface preparation, casting and curing period, generally lasting about 28 days and reducing the available floor space. In contrast, the installation of FRP is much easier and faster, requiring only surface preparation. Being only a few millimeters thick, the installation process can be completed in 2 to 3 days, including the curing time. Furthermore, FRP confinement provides additional strength when loaded. It provides passive confinement to the concrete and only activates when the concrete cracks and dilates under axial load (Lam and Teng, 2002). Once it is activated, it can enhance the capacity of the columns. However, FRP is relatively costly and shows poor properties when exposed to high temperatures or wet environments (ACI 440.2R-17, 2017).

Fig. 1.2: Alternative external retrofitting through CFRP confinement.

Experimental work using FRP to retrofit concrete structures was reported in Germany in 1978. FRP systems were first applied to reinforced concrete (RC) columns for additional confinement in Japan in 1980 and flexural strengthening of RC bridges in Switzerland. The first published codes and standards appeared in Japan and Europe in 2001 (ACI 440.2R-17, 2017). Carbon fiber reinforced polymer (CFRP) reinforced columns perform better over Glass FRP in steel-reinforced columns under eccentric loading (Hadi, 2005).

1.3 Significance of the Study

When columns are wrapped with FRP, concrete's apparent compressive strength and capacity are increased due to the confinement effect of the FRP. It also improves the ductility of the columns significantly. However, most past studies focused on the behavior of FRP-confined specimens under uniaxial compression. Except for a few interior columns, most columns located around the edge or at the corners are subjected to uniaxial and biaxial bending because of the discontinuity of the floor beam. Even the interior columns experienced bending due to different stiffness of beams at the column-beam joint, non-uniform floor panel size under a column, and for pattern live loading on uniform panels. The guide ACI 440.2R-17 (2017) does not recommend an FRP system for concrete with a compressive strength (f'_c) of less than 17 MPa and does not account for concrete masonry units. Only limited studies have been done on the effect of FRP jacketing, particularly CFRP, on low-strength, sub-standard square and rectangular columns made of recycled brick aggregates. Besides, no appropriate design guidelines are found for FRP-confined brick aggregate columns. Also, due to the lack of availability of code data, the true behavior of brick aggregate columns is hard to predict. This research investigates the axial capacity enhancement, axial and lateral strain in concrete and reinforcement, failure modes, moment capacity, toughness, and ductility of CFRP-confined recycled brick aggregate square and rectangular columns under eccentric loading. In addition, the effect of lateral ties on the axial capacity, deformation response, failure modes of columns, and the capacity of low-quality brick aggregate columns under concentric loading are examined. The nominal axial load-carrying capacity equation for columns does not incorporate the effect of shear reinforcement (ACI 318-14, 2014). However, it plays a vital role in a column's capacity and behavior under loading.

1.4 Objectives

The present study aims to fulfill the following objectives:

(i) To investigate the compressive strength, axial strain, and lateral strain of recycled brick aggregate rectangular columns before and after the carbon fiber reinforced polymer (CFRP) retrofitting.

(ii) To examine the confinement effect of CFRP retrofitting of the recycled brick aggregate rectangular concrete column.

1.5 Scope of the Study

The present study was designed to explore the behavior of CFRP-wrapped square and rectangle recycled brick aggregate columns using low-strength concrete under concentric and eccentric loads. The columns tested were scaled down to one-third of a prototype column that measures 400 mm x 400 mm x 3000 mm. This prototype was selected for compatibility with column-beam joint capacity and standard floor height. Two different cross-sectional sizes were used in the experimental model: 150 mm x 150 mm (aspect ratio, h/b = 1) and 150 mm x 225 mm (aspect ratio, h/b = 1.5), both maintaining a consistent height of 950 mm (kl/r = 21.94, l/h = 6.33 and kl/r = 14.63, l/h = 4.22). The study used two combinations of CFRP confinement, one discrete layer and one continuous layer of CFRP. One column of each size was also tested under concentric loading to compare the effect of eccentricity on the behavior of the column. One square column having no transverse reinforcement was prepared to observe the effect of the bar confinement on axial capacity, dilation, ductility, and toughness. Cylinders of two sizes, 100 mm x 200 mm and 150 mm x 300 mm, were confined with one and two layers of CFRP to notice the effect of CFRP confinement on the compressive strength of concrete.

1.6 Methodology

The focal point of this study is to examine the effect of CFRP retrofitting on recycled brick aggregate concrete columns; hence, recycled brick aggregate has been used here as coarse aggregate. Recycled brick was collected from around a 40-year-old 4-storied load-bearing wall-type building to get coarse aggregate. The CFRP fabric was purchased from a chemical company that sourced them from South Korea. For reinforcing bars, 40-grade mild steel bars were used. Seventeen columns of two sizes and two different strengths (17 MPa and 10 MPa) were prepared for this study. Out of which, eight columns were 17 MPa, and nine columns were 10 MPa strengths. Three 150 mm x 150 mm columns (one with no transverse ties) and two 150 mm x 225 mm columns were tested under concentric loading with no CFRP confinement. One 150 mm x 150 mm column and one 150 mm x 225 mm column of each strength group were cast for each of the following wrapping combinations: no wrapping, one ply of discrete wrapping, and one ply of continuous wrapping, all of which were subjected to eccentric loading. The 150 mm x 150 mm columns were tested with 45 mm (30% of h =150 mm) eccentricity, and the 150 mm x 225 mm columns with 90 mm (40% of h =225 mm) eccentricity.

The standard ACI 440.2R-17 (2017) does not provide any minimum dimensions regarding the overlapping of CFRP fibers along their length, rather than suggesting sufficient overlap to promote FRP failure before debonding the overlapped FRP laminates. As such, the required overlap for an FRP system needs to be provided to adhere to the material manufacturer guidelines and substantiated through testing. On the other hand, ACI 440.2R-17 (2017) provided an equation for development length, $l_{df} = \sqrt{\frac{nE_f t_f}{\sqrt{f'_c}}}$ to develop the effective FRP stress at a section, and suggesting to provide more anchorage length rather than the calculated by this equation. The calculated development was found to be 75 mm - 85 mm, but 100 mm - 150 mm was suggested by the manufacturer. Finally, a CFRP overlapping length of 150 mm was used for columns. In a study conducted by Guo et al. (2018) used 150 mm overlapping for all the wrapped specimens.

Eighty-four 100 mm x 200 mm cylinders were cast to determine the fresh and hardened properties of the concrete. In addition, twenty-one 150 mm x 300 mm cylinders were also fabricated to find the CFRP-confined compressive strength of the concrete with an overlapping length of 100 mm. All the columns were tested using a Universal Testing Machine (UTM) using a displacement-controlled loading rate of 1 mm/min. The columns were fixed at the top and bottom prior to testing in the case of concentric loading. On the other hand, hinge support was provided for eccentric loading. The applied load and its corresponding axial deformation were collected from UTM. To determine the midpoint lateral deflection, four linear variable differential transformers (LVDT) were attached to the columns at mid-height. Concrete and steel strain gauges were affixed to obtain the concrete and reinforcement strain data. A data logger was used to collect data from LVDTs and strain gauges. Finally, a high-resolution video camera was used to observe the failure mode.

1.7 Outline of the Thesis

The thesis is outlined in five separate chapters. Below is a brief description of the scope of these sections.

Chapter 1 (Introduction):

This chapter summarizes the fundamental concepts of this research work. This chapter covers the study context, the problem statement, the research goal, the analysis scope, and a brief methodology of the thesis procedure.

Chapter 2 (Literature Review):

A review of the findings of past research conducted on similar topics all over the world is presented in this section. This includes studies on FRP-confined specimens using different aggregates, FRP types, and loading conditions.

Chapter 3 (Materials and Methodology):

This section describes the experimental procedure of this study. Physical properties of aggregates and materials, mix design, preparation of the specimens, test set-up, fresh properties, and hardened properties of the concrete are included herein.

Chapter 4 (Results and Discussion):

This section shows the results of the experiments, the result explanation, and compares the experimental results with the code prediction.

Chapter 5 (Conclusions and Recommendations):

The conclusions drawn out from this study and the recommendations for future research are discussed herein.

CHAPTER 2
LITERATURE REVIEW

2.1 General

Across the globe, many buildings are not adequately equipped to meet current demands. These structures may have been originally under-designed, built without proper adherence to building codes, or can't handle increased loads due to expansion. Considering sustainability, reinforcing these structures rather than demolishing and rebuilding them is often more practical. This is particularly pertinent for developing countries, where the substantial cost of demolition and reconstruction presents a significant obstacle. One such effective method of revamping these structures is by strengthening the columns, which play a crucial role in the structural integrity of a building. In many developing nations such as Bangladesh, India, Pakistan, Egypt, and others, buildings were often constructed with brick aggregates, primarily due to the unavailability of stone aggregates (Mohammed et al., 2015). Reinforced concrete (RC) jacketing is a common, cost-effective method used to strengthen columns. However, this technique has drawbacks, including reduced usable space, the increased overall weight of the structure, and the necessity of drilling into columns, which can further compromise their integrity (Ranjan and Dhiman, 2016). Consequently, researchers have been exploring the use of Fiber-Reinforced Polymer (FRP) composites as a potential alternative for strengthening columns. The benefits of FRP composites are numerous - they offer enhanced resistance to fatigue stress, a high strength-to-density ratio, increased deformability and ductility, and more (Pendhari et al., 2008). As such, these materials are being studied for their viability as a new method of enhancing the strength and confinement of columns.

2.2 Brick Aggregates in Concrete

While stone aggregates are the preferred choice for constructing heavy structures, countries with limited natural stone resources, such as Bangladesh, often use brick chips as coarse aggregates in concrete. According to a 2017-2018 study, only 11% of the stone aggregates used in construction in Bangladesh came from local sources, mainly from the northern part of the country (Islam et al., 2020). The rest was imported from international sources like India, the United Arab Emirates, Oman, Thailand, and Vietnam. The major local suppliers of stone aggregates are Sylhet, Dinajpur, and Panchagarh.

The type of aggregate significantly impacts the resultant properties of concrete. Concrete produced with brick aggregates, as opposed to stone aggregates, has a lower unit weight and modulus of elasticity. This is primarily due to the porosity, micro-defects, and lower density associated with bricks (Khalaf, 2006, Debieb and Kenai, 2008, Cachim, 2009, Hasnat et al., 2016). The porous nature of bricks leads to weaker concrete strength and increased water absorption capacity (Khalaf and DeVenny, 2004). However, a study by Mohammed et al. (2015) revealed that recycled brick aggregate properties resemble those of recycled stone aggregate. One notable benefit of brick aggregate is its impressive fire resistance owing to its superior refractory properties (Khalaf and DeVenny, 2004).

An investigation by Paul et al. (2018) suggested that concrete of adequate strength can be achieved by using first-class brick aggregate and reducing the water-cement ratio. In their experimental study, the researchers used three different types of normal brick aggregates, which were categorized as 1^{st}, 2^{nd}, and 3^{rd} classes. These aggregates had distinct characteristics. The fineness modulus for the three types were 6.69, 6.70, and 6.73, respectively. The specific gravity values were 2.2, 2.0, and 2.0, while the absorption capacities were 17.43%, 22.78%, and 25.24%. The water-cement ratios of 0.55, 0.45, and 0.40 were used for each aggregate type, and among the mix designs using the water-cement ratio of 0.40 with the 1st class normal brick aggregate resulted in concrete with a compressive strength of 26 MPa at 28 days. In contrast, 3rd-class normal brick aggregate with a water-cement ratio of 0.55 concrete exhibited the least compressive strength, 15 MPa. Modulus of elasticity was found to range from 12.5 to 17 GPa, and it was also increased with a decrease in the water-cement ratio. In a study by Mohammed et al. (2015) also revealed that reducing the water-cement ratio with 3rd to 1st-class brick aggregate improves the compressive strength and modulus of elasticity of concrete.

The modulus of elasticity is a measure of the stiffness or rigidity of a material. It quantifies the ability of a material to deform under stress and return to its original shape when the stress is removed. The modulus of elasticity of brick aggregate concrete can vary depending on several factors, including the properties of the brick aggregates, the mix design, and the curing conditions (Mia et al., 2015). The modulus of elasticity is influenced by factors such as the aggregate size, shape, and grading, as well as the cementitious materials and their proportions in the concrete mix. Brick aggregates typically have a lower modulus of elasticity compared to natural aggregates like crushed stone (Amin and Choudhury, 2015).

This is due to the inherent properties of bricks, such as their porosity and lower strength compared to natural stones. The modulus of elasticity significantly influences Poisson's ratio of the concrete. A lower modulus of elasticity leads to increased dilation properties of the concrete. This enhanced dilation activates the passive confinement of the Fiber-Reinforced Polymer (FRP), only achieving improved concrete strength after the concrete has expanded and dilated.

A case study was conducted, and Fig. 2.1 displays an existing 2-story R.C. soap processing factory building, covering an aggregate floor area of around 16,900 sq ft, constructed around 1965. The building's main structural elements comprised R.C. isolated pile foundations, columns, beams, and two-way and one-way slabs. The floor heights of the building were 18'-10" on the ground floor, 19'-2" on the first floor, and some portions were 38'-0". A total of 22 columns out of 47 columns (47%) were found physically severely distressed at the ground floor level. Re-bars of distressed columns were rusted, drastically reducing the cross-sectional area due to high corrosive exposure. Alongside, the propagation of corrosion was progressive. Concrete core sample tests were done to determine the existing concrete's durability and strength. The equivalent specified concrete was found to be 6.23 MPa for columns, beams, and slabs 6.80 MPa as per American Concrete Institute (ACI 562-21, 2021), which was much below the minimum value of structural concrete strength of 17 MPa up to four storied building recommended by Bangladesh National Building Code (BNBC, 2020). Brick coarse aggregate was used, which is strictly prohibited for use in corrosive environments or other severe exposure conditions (BNBC, 2020). Carbonation-induced corrosion was detected in the concrete, resulting in swelling of the reinforcement and causing the development of cracks in the concrete. Furthermore, carbonation destroys the passive film around the steel reinforcement and reduces the strength and durability of the concrete. The tested yield strength of the re-bar was found to be 193 MPa, where at least 227 MPa were available at that time as per code reference (ACI 562-21, 2021). Therefore, most columns and floor beams were overstressed against the anticipated gravity load. Moreover, the story drifts and sway of the building against environmental loads exceeds the recommended allowable limits (BNBC, 2020). Generally, the building codes suggest the strong column-weak beam principle for both directions (ACI 318-14, 2014), but this principle was not followed here.

Fig. 2.1: Deteriorated column of an existing soap factory building.

2.3 Behavior of FRP Confined Specimens

2.3.1 Failure Modes

Many researchers have explored the influence of Fiber-Reinforced Polymer (FRP) confinement on different kinds and sizes of specimens, including cylinders and columns. Nadim et al. (2019) experimented with two sizes of circular specimens (100 mm x 200 mm and 150 mm x 300 mm) using a single layer of Carbon Fiber-Reinforced Polymer (CFRP), comparing the performance of stone and brick aggregates. Both aggregate types displayed similar failure modes with CFRP wrapping; the CFRP ruptured with a loud noise and showed strong bonding with the specimen without failure at the overlap zone. A similar study by Jiang et al. (2020) using cylindrical specimens with CFRP confinement showed that unconfined cylinders failed with a large vertical crack, while the CFRP hoops in the confined samples ruptured at failure. This was similar to the behavior seen in circular specimens tested by Teng et al. (2015), which contained different amounts of recycled concrete lumps and were confined with E-Glass FRP. Chen et al. (2016) demonstrated that when 150 mm x 300 mm cylinders containing recycled aggregate were confined with CFRP, the jacket ruptured suddenly at mid-height, away from the overlapping portion. Gao et al. (2016) constructed cylindrical specimens containing a blend of recycled aggregate and recycled clay brick aggregate, comparing the effects of Glass Fiber Reinforced Polymer (GFRP) and CFRP. They observed distinct failure patterns with GFRP confinement, including discontinuous tearing sounds, cracks' gradual appearance, and FRP layer hunching until tension failure. However, CFRP-confined specimens displayed brittle and sudden failures. Choudhury et al. (2016) investigated the failure of the CFRP-confined cylinder and cube made of stone, brick, and recycled aggregates using high-quality video imaging. They noted that the brick aggregate cylinder confined with CFRP failed more rapidly than those made of stone aggregates. This rapid failure was due to the greater dilation properties of brick aggregates. In a study by Ilki et al. (2008), they tested R.C columns with different cross-sections (250 mm diameter, 250 mm square and 150 mm x 300 mm rectangle for a constant height of 500 mm) with a length-to-diameter (L/D) ratio of around 2 under monotonic or cyclic uniaxial compressive loading. They noticed that the failure generally happened by abrupt tearing of CFRP sheets at mid-height and that the number of cuts in the CFRP jacket increased with the number of plies. However, the failure pattern was similar for low (10.94 MPa) and medium strength (23.86 MPa) specimens made from gravel. Hadi and Widiarsa (2012) studied square columns (cross-section with a side dimension of 200 mm and a height of 800 mm) with an L/D ratio of 4, wrapped with CFRP, and loaded both concentrically and eccentrically. High-strength concrete (79.50 MPa) was used. The failure of columns initiated with the formation of ripples in the CFRP sheets, which was followed by the rupture of the FRP strap-by-strap with loud snapping noises at peak load. Investigating the core of the column revealed that the concrete dilated at the places where the CFRP ruptured, which was at the corners of the column. The failure was also accompanied by buckling of the longitudinal reinforcement and crushing of the concrete. In the study conducted by Guo et al. (2018), the researchers investigated the behavior of square concrete columns with specific dimensions: a width of 200 mm and a height of 500 mm. These columns were subjected to concentric loading and were partially wrapped with carbon fiber-reinforced polymer (CFRP). The concrete used in the study had a strength of 34.74 MPa. To analyze the effect of CFRP reinforcement, the researchers considered various clear spacing configurations of the CFRP, ranging from 20 mm to 60 mm. Additionally, they varied the width of the CFRP from 40 mm to 120 mm. Furthermore, they applied different numbers of CFRP layers, ranging from 1 to 3, to the specimens. The study's findings revealed that the partially wrapped specimens generally experienced failure of the CFRP material. This failure occurred either near or at the mid-height of the column, particularly close to the transition points between the corner and flat sides of the column.

During the loading process, cracks in the concrete appeared at the clear spacing at an earlier stage. These cracks then gradually expanded until the CFRP ruptured, which was accompanied by concrete crushing failure. Cascardi et al. (2020) examined the behavior of masonry columns with discontinuous CFRP confinement under uniaxial compressive loading. The failure was identified by the cracking noise of the masonry column core during the early stages of loading, and sounds of CFRP rupture were heard multiple times near the failure point. However, the failure was primarily driven by the cracking of the unconfined masonry regions.

2.3.2 Compressive Strength

Globally, researchers have been investigating the application of Fiber-Reinforced Polymer (FRP) composites as a viable alternative for enhancing the strength of columns. Table 2.1 shows detailed results on confined compressive strength from various authors.

Table 2.1: Confined compressive strength increments of different sizes cylinders

Author	Size of cylinder	Aggregate type	FRP type & No. of ply	Average f'_c (MPa)	Average $f'cc$ (MPa)	Strength increase
Jiang et al. (2020)	150 x 300	Recycled brick	CFRP-1	31.10	43.90	41%
			CFRP-2	31.10	59.00	90%
			CFRP-3	31.10	74.80	141%
Nadim et al. (2019)	100 x 200	Brick	CFRP-1	18.23	54.48	199%
	100 x 200	Stone		21.30	61.44	188%
	150 x 300	Brick		14.31	45.61	219%
	150 x 300	Stone		22.83	49.83	118%
Choudhury et al. (2016)	100 x 200	Recycled brick	CFRP-1	25.58	49.26	93%
	150 x 300			31.23	42.89	37%
	200 x 400			28.16	33.89	20%
	100 x 200		GFRP-1	25.58	53.27	108%
	150 x 300			31.23	47.80	53%
	200 x 400			28.16	34.88	24%

Jiang and Teng (2007) conducted experiments using various natural aggregate concrete specimens of different sizes and Fiber-Reinforced Polymer (FRP) types. For the 150 mm x 300 mm specimens confined with Carbon Fiber-Reinforced Polymer (CFRP), they found that adding 1, 2, and 3 plies of CFRP sheets enhanced the compressive strength by 21.6%, 45.5% and 77.6%, respectively. Chen et al. (2016) conducted a similar study but observed larger increments of 40.4%, 77.5%, and 116% for natural aggregate concrete specimens. Further aligning with these findings, Chen et al. (2018) reported strength increases of 22.5%, 85.4%, and 137.1% for 1, 2, and 3 layers of CFRP wrapping, respectively. Lim and Ozbakkaloglu (2015) used specimens made from various concrete strengths (51.6 MPa~128 MPa using natural aggregate), FRP types, and varying numbers of layers. One and two layers of CFRP resulted in confined compressive strength increases of 87.7% and 192.5%, respectively. However, they reported even larger strength increases with 1 and 2 layers of Glass Fiber Reinforced Polymer (GFRP) at 96.1% and 196.5%, respectively. An even further increase was observed with Aramid Fiber-Reinforced Polymer (AFRP), where similar confinements led to percentage increments of 102.3% and 226.6% by GFRP.

2.3.3 Axial Load-Deformation Responses

Applying Fiber-Reinforced Polymer (FRP) confinement enhances columns' axial load and deformation. Cascardi et al. (2020) analyzed the behavior of square masonry columns under various confinement conditions. They discovered that columns wrapped with continuous glass fiber reinforced polymer (GFRP) nearly doubled the compressive load-bearing capacity. Moreover, the ratio of ultimate axial deformations between confined and unconfined columns reached 450%. However, discontinuous wrapping resulted in a 20% reduction in load-bearing capacity, with no significant decrease in ultimate axial deformation compared to continuous wrapping.

Hadi and Widiarsa (2012) investigated the performance of high-strength concrete (79.50 MPa) square columns under concentric loading, 25 mm and 50 mm eccentricity, and pure flexural conditions, with 0, 1, and 3 layers of CFRP. Given the brittle nature of high-strength concrete, slight load enhancements were observed. CFRP-confined concentric columns with 1 and 3 layers increased peak load by 1% and 10.4%, respectively. Under 25 mm eccentricity, CFRP contributed to a better load enhancement, achieving 6.5% and 16.4% higher capacity for 1 and 3 layers, respectively. Increasing the eccentricity to 50 mm led to even better results, causing a 7.3% increase in peak load for one layer and a 14.8% increase for three layers of CFRP wrapping. Notably, an increase in axial displacements at the ultimate load under concentric loading was detected due to the confinement effect. On the other hand, decrement is also observed for eccentric loading, and the same pattern is followed for the increasing eccentricity on account of the non-uniform distribution of the applied load.

In a study by Ilki et al. (2008), different types of columns (250 mm diameter circular, 250 mm square, and 150 mm x 300 mm rectangular) were subjected to monotonic or cyclic uniaxial compressive loading. The specimens had varying strengths: low (10.94 MPa) and medium (23.86 MPa), and were reinforced with CFRP jackets consisting of 0, 1, 3, or 5 layers. For the low-strength specimens, the average ratios of confined concrete compressive strength to unconfined concrete member strength were as follows: 3.0, 1.9, and 1.4 for circular, square, and rectangular columns with one ply of CFRP; 5.5, 3.6, and 2.8 for three plies; and 8.7, 4.6, and 3.9 for five plies of CFRP jackets, respectively. In the case of medium-strength specimens, these ratios were 3.2, 1.9, and 1.8 times for three plies and 4.0, 2.5, and 2.4 times for five plies of CFRP jackets. The results indicated that CFRP jackets were more effective in enhancing the strength of columns with low-strength concrete. Circular columns experienced the most significant strength gain among the different column shapes due to superior confinement. However, rectangular columns exhibited the largest deformations, followed by square columns. This can be attributed to higher axial and transverse plastic deformations caused by less effective confinement pressure. An exception to these findings was observed in the case of 1 ply jacketed specimens with low-strength concrete, where circular, square, and rectangular specimens showed similar deformability's. The enhancement in deformability was significantly more remarkable in the case of low strength concrete. CFRP jackets prevented buckling of longitudinal bars and maintained the dual confinement effect provided together with internal transverse bars, as well as preventing spalling of cover concrete. Therefore, the contribution of cover concrete to axial strength and the contribution of longitudinal reinforcement to the axial strength and ductility were maintained until very large axial deformations, making the specimens benefit from the strain hardening of longitudinal bars at the ultimate state.

Guo et al. (2018) investigated the performance of the partial wrapping confinement effect on a square column having a concrete strength of 34.74 MPa under concentric loading. They found the strength increment is highly related to the FRP strip clear spacing rather than the FRP strip width. For CFRP strips with a width of 80 mm and clear spacing of 40 mm, the strength increments were 1%, 19%, and 32% when applying 1, 2, and 3 plies, respectively. However, when the width was increased to 120 mm while keeping the same number of plies and clear spacing, the strength increments were 7%, 12%, and 37% for 1, 2, and 3 plies. In the case of full wrapping, the strength increments were 7%, 33%, and 79% for applying of 1, 2, and 3 plies of CFRP, respectively. Overall, the study revealed that the clear spacing of the CFRP strips played a significant role in determining the strength enhancement, while the width of the strips had a less pronounced effect on the column's performance under concentric loading.

2.3.4 Dilation Effects

When concrete is subject to uniaxial loading, cracks can form as the concrete core attempts to expand laterally. FRP confinement subsequently restricted this expansion (Lam and Teng, 2002). A study by Jiang and Teng (2007) evaluated stress-strain models for FRP-confined concrete, finding that most stress-strain curves displayed a bi-linear, ascending characteristic influenced by both the confinement ratio and the stiffness of the confining material. In their research, Nadim et al. (2019) noticed that CFRP confinement led to substantial dilation of specimens under uniaxial compression. Moreover, the brick-based ones demonstrated higher lateral strains between stone and brick aggregate concrete specimens. This observation aligns with previous research by Islam et al. (2016), which found that brick aggregate columns confined with CFRP displayed 17.2% higher lateral strain compared to their stone aggregate counterparts. Similarly, Choudhury et al. (2016) found that concrete with aggregates that dilated more effectively displayed a greater stiffness gain from both GFRP and CFRP confinement.

Gao et al. (2016) studied concrete made with recycled clay brick aggregate and encased in GFRP and CFRP. They observed that the type of FRP didn't significantly affect the dilation rate for a given number of layers. However, when the number of layers increased from two to four, the dilation rate decreased by 33.3%. Further confinement of four to six layers led to an additional decrease of 30%. Regarding the impact of FRP thickness on dilation, a study by Jiang et al. (2020) found that as confined concrete dilates under pressure, the confining pressure rises, potentially leading to a reversal of volumetric expansion if the FRP sheets are very stiff. Ilki et al. (2008) conducted experiments on low (10.94 MPa) and medium strength (23.86 MPa) columns retrofitted with CFRP sheets. Their experiment exhibits that the transverse strain on CFRP jackets at failure was between 0.007 and 0.018

regardless of the jacket thickness, with an average value of 0.012 for low strength specimens. For the medium strength specimens, the transverse strain was between 0.012 and 0.015, with an average value of 0.014. These average values are about 80 – 93% CFRP's ultimate rupture strain of 0.015. Their results also demonstrated that the Poisson's ratio followed a similar trend when varying the number of CFRP layers (3 and 5 plies) for both the low and medium strength columns. Nonetheless, for the same number of layers, the low-strength columns displayed a smaller Poisson's ratio, and the Poisson's ratio decreased with an increased number of layers.

2.3.5 Ductility

Substantial research conducted over recent years has demonstrated that FRP materials significantly enhance the ductility of concrete. As evidenced by Ilki et al. (2008) research, CFRP confinement delayed the buckling of longitudinal reinforcement to higher strains up until the failure of CFRP jackets. This delayed buckling preserved the contribution of the concrete cover and reinforcement to the axial strength, allowing for larger ultimate deformations and thus improving the material's ductility. In their work, Islam et al. (2016) found that both GFRP and CFRP increased the maximum axial strain of square concrete columns using various types of aggregate. Implementing CFRP and GFRP wraps for brick aggregate columns resulted in a 23.5% and 29.4% increase in ultimate axial strain, respectively, indicating an enhancement in ductility. Cascardi et al. (2020) suggested that FRP is particularly effective in enhancing ductility in poor-quality masonry or concrete with low compressive strength. In their experiment, Hadi and Widiarsa (2012) tested square columns under eccentric loading with different configurations of CFRP wrapping. They found that columns wrapped with three layers of CFRP demonstrated superior ductility to those with one vertical and two horizontal layers of CFRP. Under both concentric and eccentric loading conditions, the increase in ductility was 0.7%, 63.3%, and 152.4%, respectively, for 1-ply, 2-ply, and 1-vertical and 2-horizontal ply configurations. Under a 25 mm eccentric load, these ductility enhancements were 15.6%, 84.4%, and 149.6%, respectively. Pantazopoulou et al. (2001) compared various repair methods for corrosion-damaged columns with FRP wraps, concluding that two plies of GFRP used in repair resulted in a 122.2% increase in ductility compared to conventional patch or coating methods. If two plies of GFRP were applied over the patch during repair, ductility improved by an impressive 159.3%.

2.3.6 Comparison with Models

Hadi and Widiarsa (2012) observed disparities between the experimental compressive strength of CFRP-wrapped columns and the theoretical predictions derived from the Lam and Teng (2002) model. Their results showed that Teng's model consistently underestimated the compressive strength of confined columns, with experimental values exceeding predicted results by 15.9%, 9.5%, and 15.7% for columns confined with one layer of CFRP, three layers of CFRP, and one vertical and two horizontal layers of CFRP, respectively.

Islam et al. (2016) analyzed the dilation effects in FRP-confined square columns using various types of aggregate. They proposed a model to predict both the confined compressive strength and the ultimate confined compressive strain. This model provided notably reliable results in predicting confined compressive strength. For stone aggregates, their model closely aligned with predictions from both the Lam and Teng (2003) model and the ACI 440.2R-08 (2008) guidelines. However, in the case of brick aggregates, their model's results were closest to predictions by the Kumutha et al. (2007) model and the ACI 440.2R-08 (2008) guidelines, even though the differences were still greater than 10%.

Gutiérrez et al. (2021) conducted experiments on various FRP-wrapped columns under axial compression. They compared their experimental results with predictions from four international codes and guidelines, including (TR55, 2000, fib, 2001, CNR, 2013, ACI 440.2R-17, 2017). The strength predictions offered by these four guidelines showed considerable variation, particularly when applied to rectangular and square columns. Furthermore, the experimentally determined effective strain in FRP did not align with the recommendations given by these guidelines.

2.4 Comparison with ACI 440.2R-17 and ACI 318-14 Standards

The ACI 440.2R-17 (2017) standard does not recommend an FRP system for concrete with a compressive strength ($f'c$) of less than 17 MPa and does not account for concrete masonry units. Using the stress-strain behavior model proposed by ACI 440.2R-17 (2017), the analytical axial load-moment (P-M) interaction diagrams for CFRP-confined columns (for continuous wrapping) can be developed. This process is achieved by satisfying strain compatibility and force equilibrium. The strain distribution for FRP-confined columns proposed by ACI 440.2R-17 (2017) is presented in Fig. 2.2.

As per ACI 440.2R-17 (2017), the section of the confined P-M diagrams relating to compression-controlled failure can be simplified into two bilinear curves. These curves pass through the following three critical points:

Point A: Pure compression at a uniform axial compressive strain of confined concrete ε_{ccu};

Point B: Strain distribution corresponding to zero strain at the layer of longitudinal steel reinforcement nearest to the tensile face, and a compressive strain ε_{ccu} on the compression face;

Point C: Strain distribution corresponding to balanced failure with a maximum compressive strain ε_{ccu} and a yielding tensile strain ε_{sy} at the layer of longitudinal steel reinforcement nearest to the tensile face.

The flowchart of calculation steps is presented in Fig. 2.3, and a detailed calculation of the theoretical axial and bending capacities of continuous CFRP confined in four experimental columns is presented in Appendix A. Fig. 2.4 is the representative interaction diagram proposed by ACI 440.2R-17 (2017).

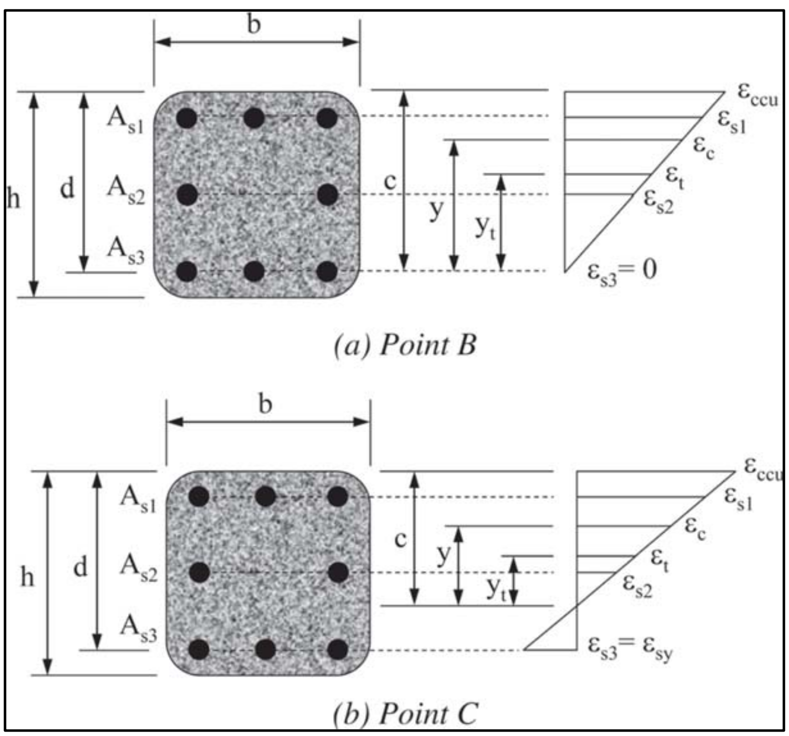

Fig. 2.2: Strain distribution for FRP-confined columns by ACI 440.2R-17 (2017).

For confined concrete, the value of φP_n corresponding to Point A is given in Eq. 2.1.

$$\Phi P_{n(A)} = \varphi 0.80(0.85f'_{cc}(A_g - A_{st}) + f_y A_{st}) \quad (2.1)$$

The coordinates of Points B and C can be computed using Eq. 2.2 and 2.3

$$\Phi P_{n(B,C)} = \varphi[\mathrm{A}(y_t^3) + B(y_t^2) + C(y_t) + D + \sum A_{si} f_{si}] \quad (2.2)$$

$$\Phi M_{n(B,C)} = \varphi[\mathrm{E}(y_t^4) + F(y_t^3) + G(y_t^2) + H(y_t) + I + \sum A_{si} f_{si}\, d_i] \quad (2.3)$$

Where,

$$A = \frac{-b(E_c - E_2)^2}{12f'_c} (\frac{\varepsilon_{ccu}}{c})^2 \quad (2.4a)$$

$$B = \frac{b(E_c - E_2)}{2} (\frac{\varepsilon_{ccu}}{c}) \quad (2.4b)$$

$$C = -bf'_c \quad (2.4c)$$

$$D = bcf'_c + \frac{bcE_2}{2}(\varepsilon_{ccu}) \quad (2.4d)$$

$$E = \frac{-b(E_c - E_2)^2}{16f'_c} (\frac{\varepsilon_{ccu}}{c})^2 \quad (2.4e)$$

$$F = [b\left(c - \frac{h}{2}\right)\frac{(E_c - E_2)^2}{12f'_c}\left(\frac{\varepsilon_{ccu}}{c}\right)^2 + \frac{b(E_c - E_2)}{3}\left(\frac{\varepsilon_{ccu}}{c}\right)] \quad (2.4f)$$

$$G = -[(\frac{b}{2}f'_c + b\left(c - \frac{h}{2}\right)\frac{(E_c - E_2)}{2}\left(\frac{\varepsilon_{ccu}}{c}\right)] \quad (2.4g)$$

$$H = bf'_c\left(c - \frac{h}{2}\right) \quad (2.4h)$$

$$I = [\frac{bc^2}{2}f'_c - bcf'_c\left(c - \frac{h}{2}\right) + \frac{bc^2E_2}{3}(\varepsilon_{ccu}) - \frac{bcE_2}{2}\left(c - \frac{h}{2}\right)(\varepsilon_{ccu})] \quad (2.4i)$$

$C = d$, for point B and $C = d\frac{\varepsilon_{ccu}}{\varepsilon_y + \varepsilon_{ccu}}$ for point C (2.5)

$$y_t = c\frac{\varepsilon'_t}{\varepsilon_{ccu}} \quad (2.6)$$

$$\varepsilon'_t = \frac{2f'c}{E_c - E_2} \quad (2.7)$$

$$E_2 = \frac{f'cc - f'c}{\varepsilon_{ccu}} \quad (2.8)$$

$$f_l = \frac{(2\mathrm{x}\ E_f\ \mathrm{x}\ n\ \mathrm{x}\ t_f\ \mathrm{x}\ \varepsilon f_e)}{D} \quad (2.9)$$

$$f'_{cc} = f'_c + \psi_f\ \mathrm{x}\ 3.3\ \mathrm{x}\ ka\ \mathrm{x}\ f_l \quad (2.10)$$

$$\varepsilon_{cuu} = \varepsilon'_c \text{ x } (1.50 + 12 \text{ x } k_b \text{ x } \frac{f_l}{f'_c} \text{ x } \left(\frac{\varepsilon f_e}{\varepsilon'_c}\right)^{0.45}) \qquad (2.11)$$

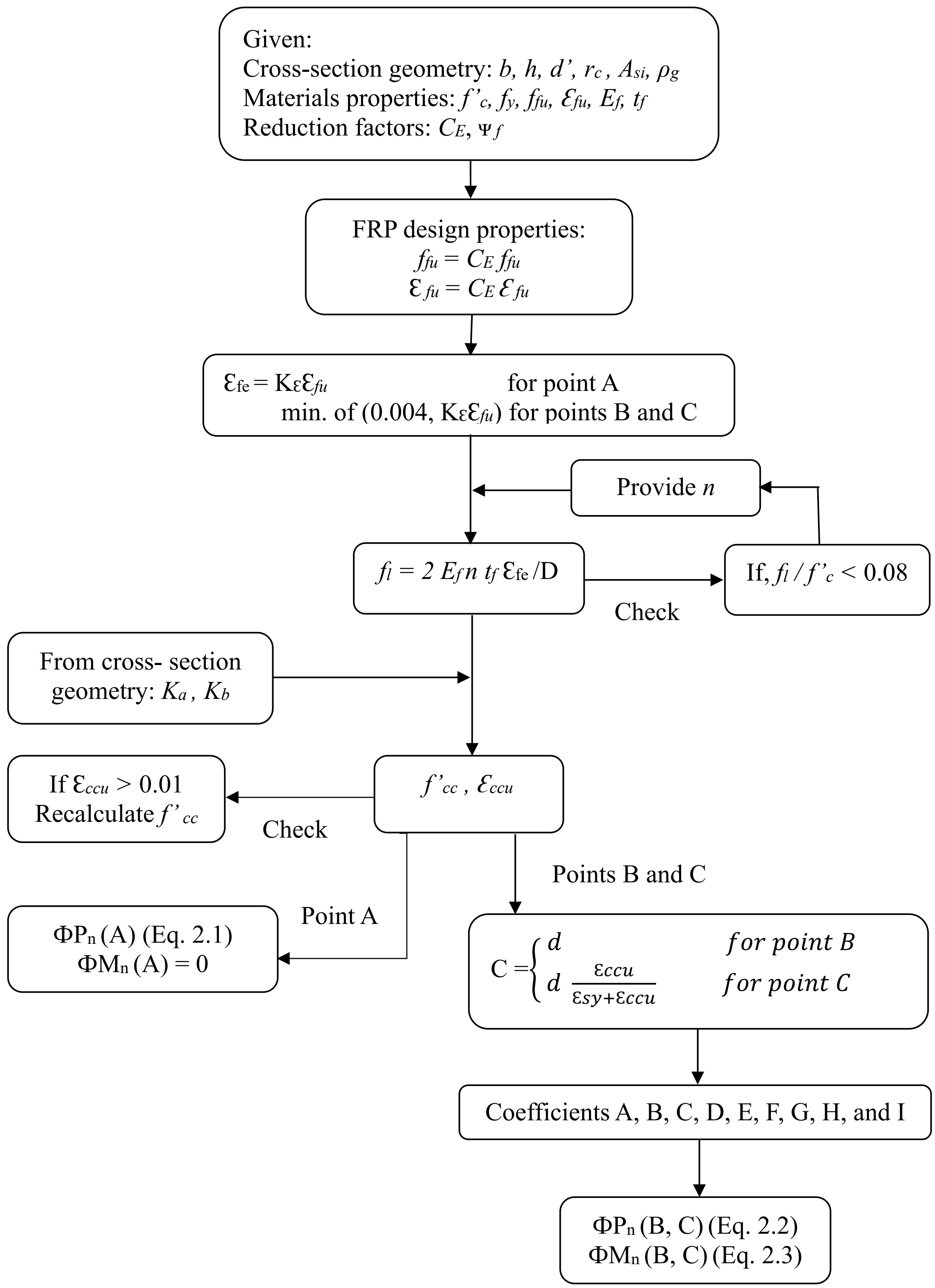

Fig. 2.3: Flowchart for calculation steps.

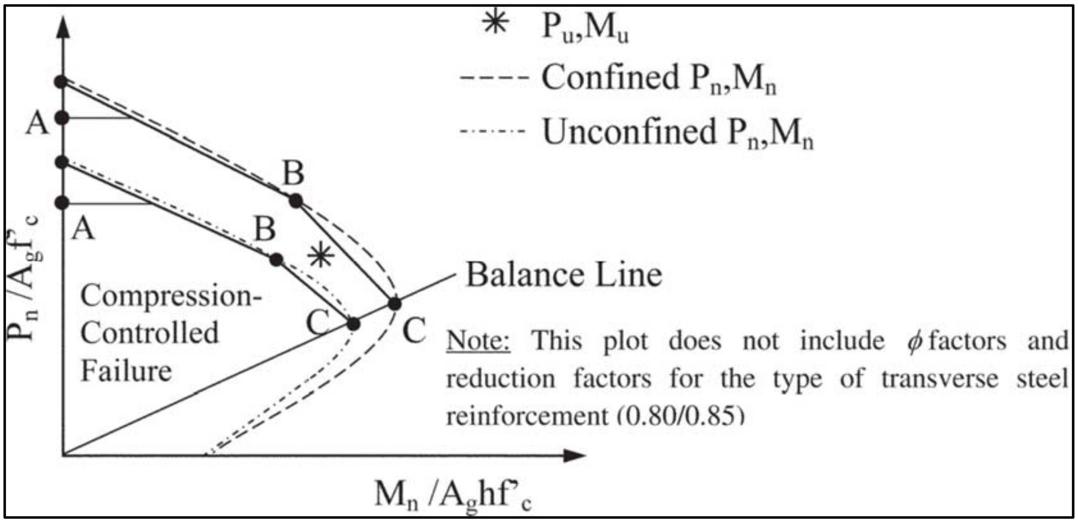

Fig. 2.4: Representative interaction diagram by ACI 440.2R-17 (2017).

The ACI 318-14 (2014) code also suggested the minimum concrete strength be 17 MPa, both normal weight and lightweight concrete. The analytical axial load-moment (P-M) interaction diagrams for unconfined columns can be developed using the stress-strain behavior model, satisfying strain compatibility and force equilibrium. The strain distribution for unconfined columns on the corresponding P-M diagram followed by spColumn (2021) is presented in Fig. 2.5. These curves pass through the following critical points:

Point 1: Maximum compression (compressive strength at zero eccentricity);

Point 2: Bar stress near tension face equal to zero, ($f_s = 0$);

Point 3: Bar stress near tension face equal to 0.5 f_y ($f_s = 0.5 f_y$);

Point 4: Bar stress near tension face equal f_y ($f_s = f_y$). This strain distribution is called the balanced failure case and the compression-controlled strain limit. It marks the change from compression failures originating by crushing the section's compression surface, to tension failures initiated by yield of longitudinal reinforcement. It also marks the start of the transition zone for ϕ for columns in which ϕ increases from 0.65 (or 0.75 for spiral columns) up to 0.90;

Point 5: Bar strain near tension face equal to $\varepsilon_y + 0.003$. In ACI 318-19 (2019) provisions, this control point corresponds to the tension-controlled strain limit of $\varepsilon_y + 0.003$, used to be 0.005 in ACI 318-14 (2014). It is the strain at the tensile limit of the transition zone for ϕ, used to define a tension-controlled section;

Point 6: Pure bending. This corresponds to the case where the nominal axial load capacity, P_n, equals zero. An iterative procedure is used to determine the nominal moment capacity;

Point 7: Maximum tension. The final loading case to be considered is concentric axial tension. The strength under pure axial tension is computed by assuming that the section is completely cracked through and subjected to a uniform strain greater than or equal to the yield strain in tension. The strength under such a loading is equal to the yield strength of the reinforcement in tension.

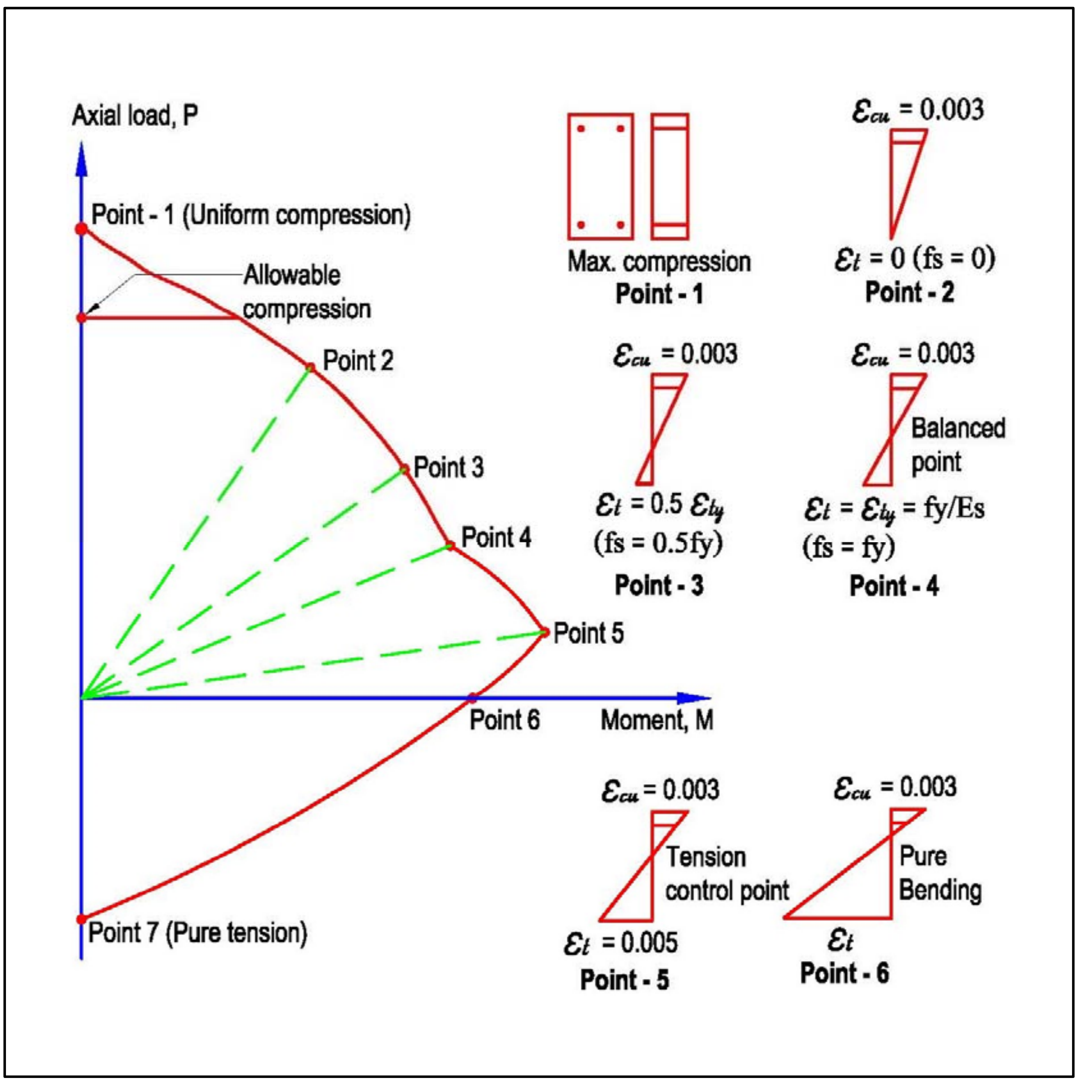

Fig. 2.5: Strain distribution for unconfined columns for ACI 318-14 (2014).

2.5 Summary

In recent years, comprehensive research has been conducted to explore the properties and potential applications of Carbon Fiber-Reinforced Polymer (CFRP) composites in structural engineering. These studies span a broad spectrum, considering a variety of scales and behaviors of CFRP, along with many combinations of experimental variables. Although there is numerous research on the performance of FRP-confined columns under concentric loading - which has evaluated aspects such as axial capacity, stress-strain behavior, and comparisons with established models - there is a noticeable lack of studies investigating the performance of CFRP-confined recycled brick aggregate columns under eccentric loading. Furthermore, there is a limited agreement between the experimental capacities of CFRP-confined recycled brick aggregate square and rectangular columns and the equations provided in standard building codes. This highlights a potential area for further exploration in order to reconcile these discrepancies and improve the understanding of CFRP's performance under varied conditions.

CHAPTER 3
MATERIALS AND METHODOLOGY

3.1 General

The present study was designed to explore the behavior of CFRP-wrapped square and rectangle recycled brick aggregate columns using low-strength concrete under concentric and eccentric loads. Thus, laboratory experiments were conducted to look into specific material qualities and the mechanical characteristics of concrete to evaluate the seventeen columns' experimental behavior under eccentric and concentric loads. In this study, recycled brick was used for coarse aggregate and collected from around a 40-year-old 4-storied load-bearing wall-type building (Fig. 3.1). Fine aggregate was used to fill the interstices in coarse aggregate, and Portland Composite Cement (PCC) was used for binding materials. For reinforcing bars, 40-grade mild steel bars were used. The CFRP fabric was purchased from a chemical company that sourced them from Korea. The 150 mm x 150 mm columns were tested with 45 mm (30% of h=150 mm) eccentricity, and the 150 mm x 225 mm columns with 90 mm (40% of h=225 mm) eccentricity. Eighty-four 100 mm x 200 mm cylinders were cast to determine the fresh and hardened properties of the concrete and to examine the CFRP confinement effect. In addition, twenty-one 150 mm x 300 mm cylinders were also fabricated to find the CFRP-confined compressive strength of the concrete. This chapter will cover the outcomes of such experiments as well as a detailed description of the experimental process. The study's factors include the column aspect ratio, concrete strength, CFRP application method, and loading type.

3.2 Materials

Materials such as recycled brick coarse aggregate, fine aggregate, Portland Composite Cement (PCC), and water have been used in this study to prepare the two different concrete mixes. A detailed discussion of the tests conducted to investigate the properties of these constituents, along with the results, is provided in the following section. Potable water was used and is a crucial component of concrete. When mixed with cement, it initiates a chemical reaction called hydration. During hydration, cement particles react with water, forming a paste that coats and binds the aggregates together, creating a solid and durable material. As the target concrete strength was low (17 MPa and 10 MPa), admixtures were not used to modify the concrete’s properties. Steel reinforcement was used to enhance the tensile strength of the concrete mix, resist tensile forces and prevent cracking under bending or tension. Carbon Fiber Reinforced Polymer (CFRP) is a high-strength composite material made of carbon fibers embedded in a polymer matrix used as a retrofitted material.

3.2.1 Aggregates

Fine aggregates are natural sand passing through a 4.75 mm sieve and retained on a 0.075 mm sieve, used as filler material in concrete. This study used Sylhet sand was used as the fine aggregate (Fig. 3.2a). The focal point of this study is to examine the behavior of the recycled brick aggregate concrete columns; hence, recycled brick aggregate was used here as coarse aggregate (Fig. 3.2b). Coarse aggregate is retained on a 4.75 mm sieve and is coarser than 4.75 mm. The maximum and minimum sizes used are 19 mm and 2.37 mm, respectively. A brick crusher machine was used to convert recycled bricks into aggregate. The physical properties of fine and coarse aggregate were determined according to ASTM standards and summarized in Table 3.1. The gradation curve of aggregates, which can be seen in Fig. 3.3, is compared against the upper and lower limits defined by ASTM. It is seen that the gradation curves of the fine aggregates comply satisfactorily with the range specified by ASTM C136/C136M-19 (2019), and can be defined as well graded, but coarse aggregate shows poorly gradation. The corresponding tested values of fineness modulus, specific gravity, absorption capacity and unit weight were within the limit specified by ASTM standards. Under the testing procedure ASTM C535-16 (2016), the Los Angeles abrasion value of coarse aggregate was found to be 45%.

Fig. 3.1: Collection of recycled brick for the source of coarse aggregate.

(a) Fine aggregate

(b) Coarse aggregate

Fig. 3.2: Aggregates used in concrete.

Table 3.1: Physical properties of aggregates

Variables	Unit	FA	CA	Standard
Fineness modulus	-	2.16	6.99	ASTM C136-19
Apparent specific gravity	-	2.75	2.47	(ASTM C128-22, 2022)
Bulk specific gravity (SSD)	-	2.66	2.01	
Bulk specific gravity (OD)	-	2.62	1.69	
Absorption capacity (%D)	%	1.80	18.68	
Loose condition unit weight (SSD)	kg/m^3	1521	1093	(ASTM C29/C29M-17a, 2017)
Compact condition unit weight (SSD)	kg/m^3	1607	1262	
Loose condition % of voids	%	39	46	
Compact condition % of voids	%	36	37	
L.A. abrasion value	%	-	45	ASTM C535-16

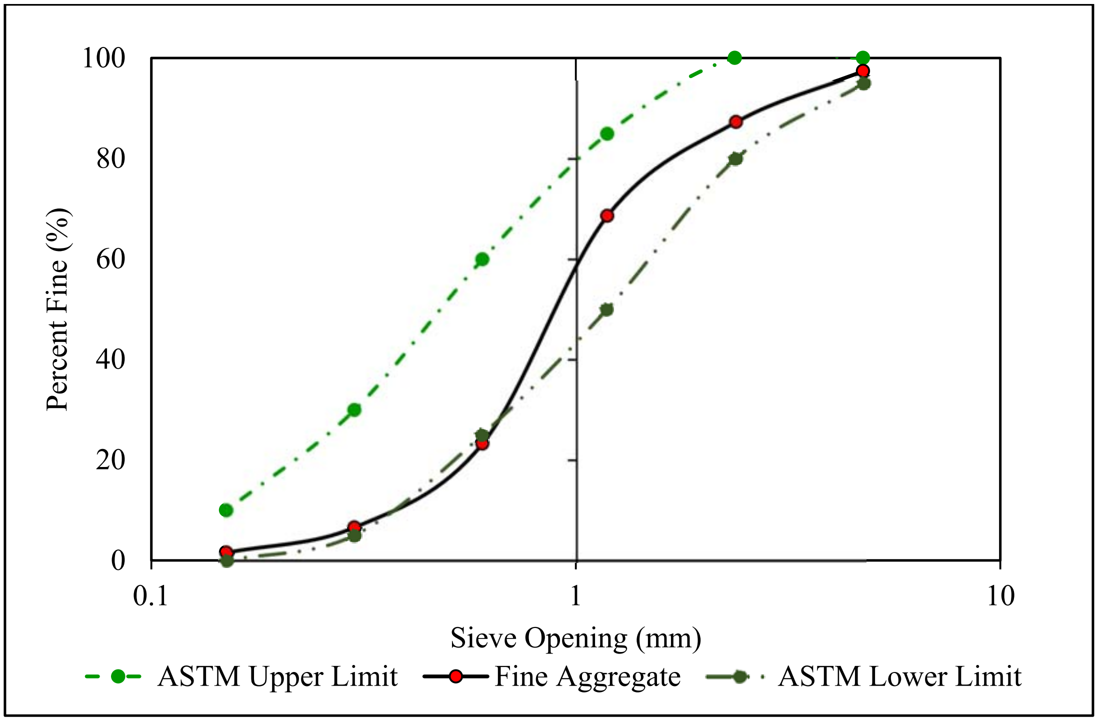

(a) Gradation curve of fine aggregate

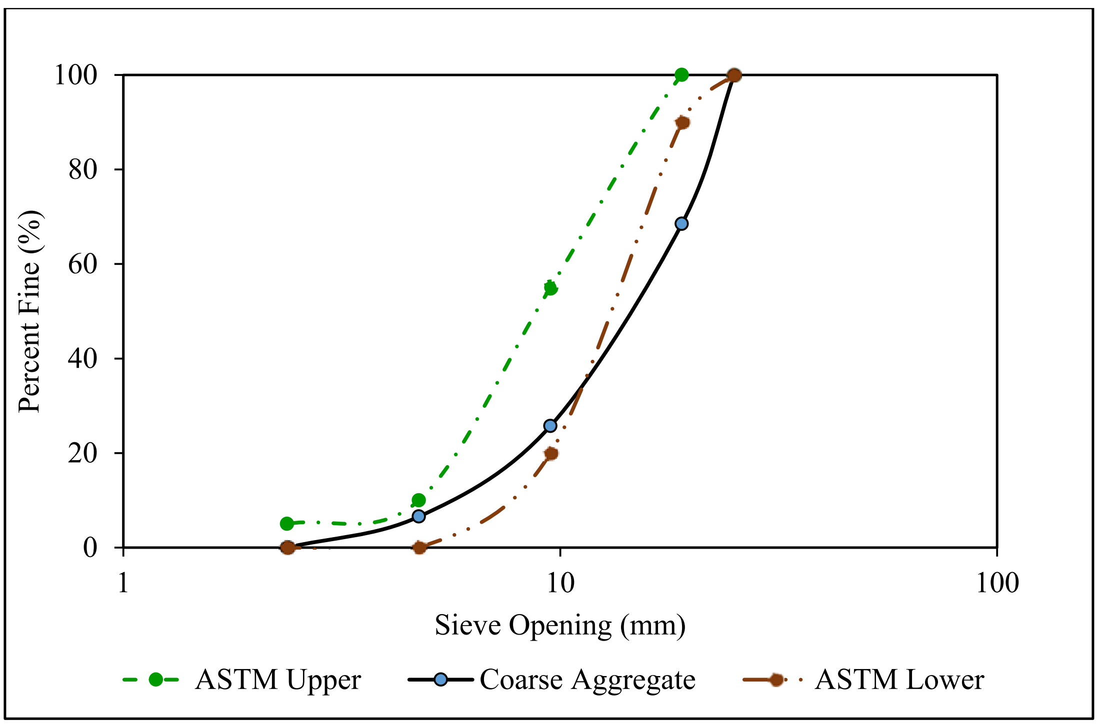

(b) Gradation curve of coarse aggregate

Fig. 3.3: Gradation curve of aggregates.

3.2.2 Recycled Brick

Samples of full-sized bricks were selected and prepared as per the specifications of ASTM C67/C67M-21 (2021). The average compressive strength of the ten samples of bricks was found to be 9.42 MPa. A unit weight test was also carried out on ten samples in the Saturated Surface Dry (SSD) condition. It was found that the average unit weight of the bricks was 536 kg/m^3, which is relatively low compared to standard bricks. The absorption capacity of the full-sized bricks was calculated using the SSD and OD weights, and the average absorption capacity was 18.68%. The physical properties of recycled brick are presented in Table 3.2. A compressive strength machine with a minimum capacity of 2000 kN and a 4.7 kN/sec loading rate was employed. The preparation of brick samples, before and after test conditions are presented in Fig. 3.4.

Table 3.2: Physical properties of full-sized bricks

Variables	Unit	Value	Standard
Compressive strength	MPa	9.42	(ASTM C67/C67M-21, 2021)
Unit weight (Based on SSD)	kg/m^3	536	
Absorption capacity	%	18.68	

Fig. 3.4: Compressive strength test of recycled brick.

3.2.3 Reinforcement

The mechanical properties of the longitudinal reinforcement used in the columns were tested using a Universal Testing Machine (UTM), following the ASTM A615/A615M-22 (2022) standard. Mild steel with 10 mm and 12 mm diameters was used as the longitudinal reinforcement. Three samples from each diameter were subjected to the tensile test. The resulting mechanical properties and stress-strain curves can be seen in Table 3.3 and Fig. 3.5, respectively.

Table 3.3: Mechanical properties of reinforcing steel

S/N	Bar Type	Unit Weight (kg/m)	d_{actual} (mm)	Average Yield Strength (YS) in MPa	Average Tensile Strength (TS) in MPa	TS/YS	Elongation (%)	Standard
1	Steel 10 mm Ø	0.66	10.35	391	541	1.38	36%	(ASTM A615/A615M-22, 2022)
2		0.64	10.19				40%	
3		0.63	10.11				44%	
1	Steel 12 mm Ø	0.81	11.47	333	450	1.35	35%	
2		0.80	11.40				33%	
3		0.79	11.32				33%	

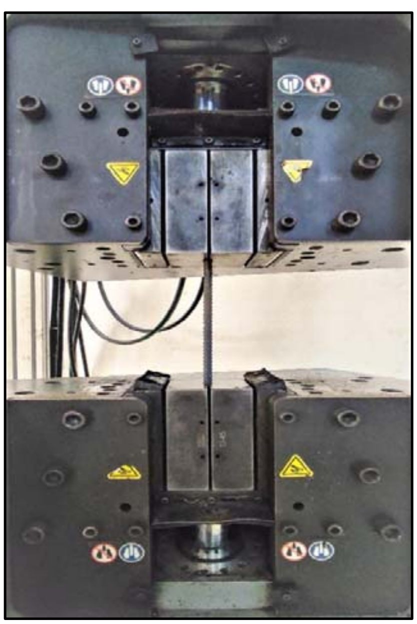

(a) Test set-up

(b) Sample after test

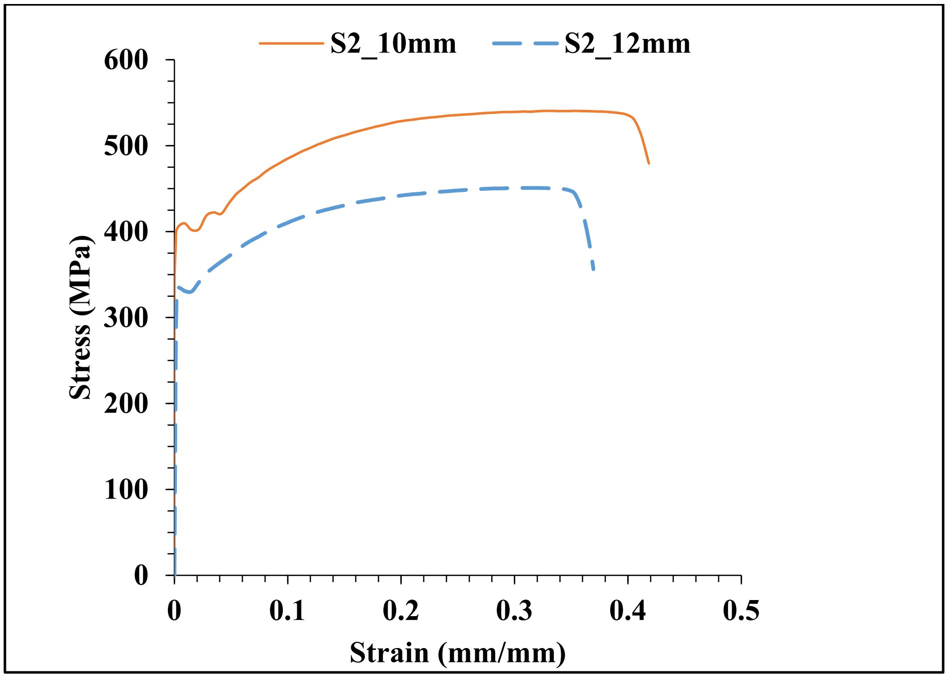

(c) Stress- strain relationship

Fig. 3.5: Tensile test of mild steel.

3.2.4 Cement

Portland Composite Cement (PCC), the brand SHAH was used in concrete mixtures whose physical and mechanical properties were determined according to ASTM standards and are presented in Table 3.4. The normal consistency of PCC was determined to be 26.50%, adhering to ASTM C187-16 (2016) standards. The initial setting time of 154 minutes exceeds the minimum requirement of 45 minutes, while the final setting time of 225 minutes falls within the acceptable limit of not more than 420 minutes, as specified by ASTM C595/C595M-21 (2021). PCC exhibits a specific gravity of 2.95 gm/cm^3, which aligns with ASTM C188-17 (2017) standards. After 3 days of curing, the compressive strength of PCC was measured at an impressive 20.18 MPa, surpassing the ASTM C595/C595M-21 (2021) standard of 13.0 MPa. Furthermore, at 7 days, the compressive strength increased to 24.21 MPa, exceeding the standard value of 20.0 MPa. Finally, at 28 days, the compressive strength of PCC reached a remarkable 29.69 MPa, again surpassing the standard requirement of 28.0 MPa. The test results possess exceptional properties, with good normal consistency, adequate setting times, and high specific gravity. Its impressive compressive strength at various curing periods shows its suitability for construction applications.

Table 3.4: Physical and mechanical properties of cement

Variables	Unit	Value	Standard	Standard values, ASTM C595-21
Normal consistency	%	26.50	ASTM C187	-
Initial setting time	Minutes	154	(ASTM C191-21, 2021)	Not less than 45 minutes
Final setting time	Minutes	225		Not more than 420 minutes
Specific gravity	gm/cm^3	2.95	ASTM C188	-
Compressive strength, 3 Days	MPa	20.18	(ASTM C109/C109M-21, 2021)	13.0 MPa
Compressive strength, 7 Days	MPa	24.21		20.0 MPa
Compressive strength, 28 Days	MPa	29.69		28.0 MPa

3.2.5 CFRP Fabric

The main aim of this study is to scrutinize the impact of Carbon Fiber Reinforced Polymer (CFRP) retrofitting on recycled brick aggregate concrete columns; thus, CFRP has been employed as the retrofitting material. The CFRP samples were tested following the ASTM D3039/D3039M-17 (2017) standard to verify the tensile properties of CFRP fabric provided by the manufacturer. Five samples were used, each measuring 250 mm in length and 15 mm in width, with a 0° unidirectional fiber orientation Fig. 3.6. To ensure a firm grip during testing, 56 mm x 20 mm x 1.5 mm steel plates were affixed at both ends of the samples. These samples were tested using a Universal Testing Machine (UTM) set to a standard head displacement rate of 2 mm/min. The mechanical and physical properties of CFRP can be seen in Table 3.5 and Table 3.6. The manufacturer provided the mechanical properties of carbon wrap encapsulation resin (a mixture of 2 parts of base and 1 part of hardener by weight ratio) and presented in Table 3.7. This innovative resin combines high-strength carbon fibers and a durable epoxy matrix, creating a versatile and robust solution for reinforcing and rehabilitating various structures. Carbon wrap encapsulation resin forms a strong, lightweight, and corrosion-resistant layer around structural components when applied. Its remarkable tensile strength and flexibility make it ideal for enhancing the load-bearing capacity of deteriorating structures and extending their lifespan. The carbon wrap primer (a mixture of 2 parts of base and 1 part of hardener by weight ratio) was tested for its pot life by the manufacturer, Korea RE & T Co., Ltd., according to KS M6030-2004 standard, and the result found to be 74 minutes.

Table 3.5: Mechanical properties of CFRP fabric

Variables	Unit	Value	Standard
Fabric tensile strength	MPa	4,900	(ASTM D3039/D3039M-17, 2017)
Fabric tensile modulus	Gpa	240	
Elongation at break	%	2.1	

Table 3.6: Physical properties of CFRP fabric

Variables	Unit	Value
Fabric design thickness	Mm	0.111
Fiber areal weight	g/m^2	210
Fabric length/roll	M	100
Fabric width	Mm	500

Table 3.7: Mechanical properties of carbon wrap encapsulation resin

Variables	Unit	Value	Standard
Pot life	Minutes	74	KS M6030-2004
Tensile strength	MPa	49	KS M3015-2003
Flexural strength	MPa	70	
Compressive strength	MPa	140	ASTM D695-2002
Shear strength	MPa	24	KS M3734-2001

(a)

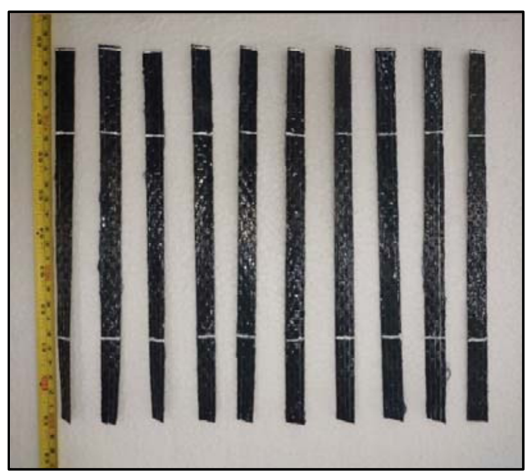

(b)

Fig. 3.6: Preparation of CFRP specimen.

3.3 Methodology

Seventeen columns of two sizes and two different strengths (17 MPa and 10 MPa) were prepared for this study. Out of which, eight columns were 17 MPa, and nine columns were 10 MPa strengths. Three 150 mm x 150 mm columns (one with no transverse ties) and two 150 mm x 225 mm columns were tested under concentric loading with no CFRP confinement. One 150 mm x 150 mm column and one 150 mm x 225 mm column of each strength group were cast for each of the following wrapping combinations: no wrapping, one ply of discrete wrapping, and one ply of continuous wrapping, all of which were subjected to eccentric loading. The 150 mm x 150 mm columns were tested with 45 mm (30% of h =150 mm) eccentricity, and the 150 mm x 225 mm columns with 90 mm (40% of h =225 mm) eccentricity. Eighty-four 100 mm x 200 mm cylinders were cast to determine the fresh and hardened properties of the concrete. In addition, twenty-one 150 mm x 300 mm cylinders were also fabricated to find the CFRP-confined compressive strength of the concrete. Fig. 3.7 shows the experimental parameters and methodology used for this study.

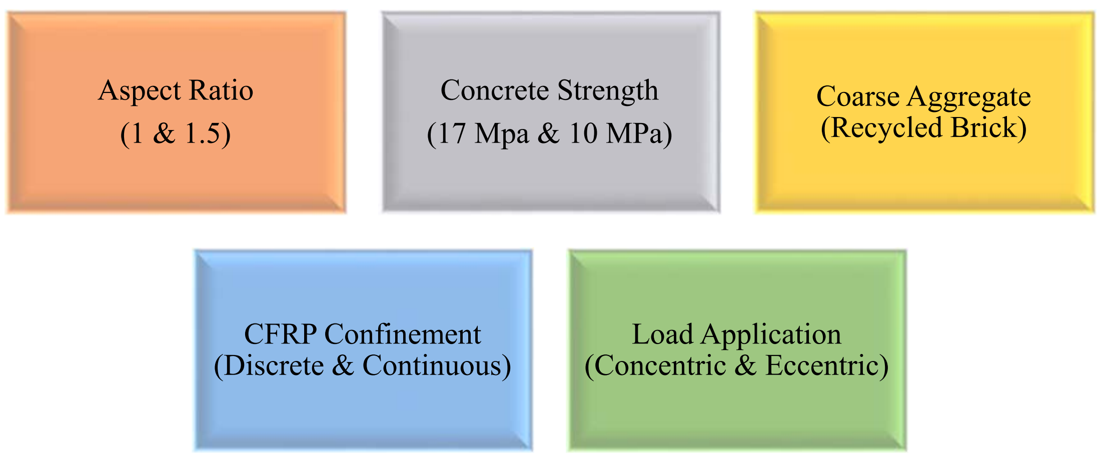

Fig. 3.7: Experimental parameters and methodology.

3.3.1 Concrete Mix Design

To investigate the effect of CFRP retrofitting on recycled brick aggregate concrete column's strength behavior, two different concrete mixes were prepared with a design compressive strength of 17 MPa and 10 MPa at 28 days. The mix design for the concrete was created following the ACI 211.1-91 (1991) code and the data gleaned from the material tests. Both the coarse and fine aggregates used were in saturated surface dry (SSD) conditions. A water-cement ratio of 0.50 and 0.65 was established, with no admixtures added to the mix. Table 3.8 presents the weight-based proportions of the materials for a single-volume unit of concrete. A detailed calculation of the mix design is presented in Appendix B.

Table 3.8: Mix proportion for 1 m^3 of concrete

W/C Ratio	Water (kg)	Cement (kg)	Coarse Aggregate (kg)	Fine aggregate (kg)	Fresh Density (kg/m^3)	Slump (mm)
0.5	190	380	862	618	2105	110
0.65	190	292	862	697	2085	115

3.3.2 Specification and Fabrication of Specimens

The subsection presents the specifications and fabrication procedures of the specimens.

3.3.2.1 Column Specifications for Testing Under Concentric and Eccentric Loading

Seventeen column specimens were prepared in accordance with ACI 318-14 (2014) specifications to commence the experimental study. These specimens were scaled down to around one-third of a prototype column (Fig. 3.8a) that measures 450 mm x 450 mm x 3000 mm (aspect ratio, h/b = 1 and kl/r = 23, l/h = 6.66). This prototype was selected for compatibility with column-beam joint capacity and standard floor height of a structure. Two different cross-sectional sizes (Fig. 3.9) were used in the experimental model: 150 mm x 150 mm (aspect ratio, h/b = 1) and 150 mm x 225 mm (aspect ratio, h/b = 1.5), both maintaining a consistent height of 950 mm (kl/r = 21.94, l/h = 6.33 and kl/r = 14.63, l/h = 4.22). The aspect ratio of 1.5 was chosen from the ACI 440.2R-17 (2017) standard, where aspect ratios greater than 1.5 are not recommended for jacketing concrete structural members with FRP in seismic applications. In order to prevent localized failure due to high-stress concentration in the end regions of the columns and to ensure uniform load distribution, enlarged heads measuring 250 mm x 250 mm x 100 mm and 250 mm x 325 mm x 100 mm were used, respectively. While model columns may not replicate all the complexities of a full-scale structure, they provide valuable insights and a physical representation that aids in the decision-making process during the early stages of design and development. Table 3.9 shows a comparison of the geometrical properties of a prototype and model column, and Table 3.10 summarizes the column test matrix.

Table 3.9: Comparison of the geometrical properties of a prototype and model column

S/N	Variables	Prototype	Model
1	Cross-sectional dimension (b x h)	450 mm x 450 mm	150 mm x150 mm
2	Aspect ratio, h/b	450/450 = 1	150/150 = 1
3	Height of the column	3000 mm	950 mm
4	Height to depth ratio, l/h	3000/450 = 6.66	950/150 = 6.33
5	Radius of gyration, r	129.9 mm	43.3 mm
6	Effective length factor, k	1	1
7	Slenderness ratio, kl/r	1x3000/129.9 = 23	1x950/43.3 = 21.94
8	longitudinal reinforcement, A_{st}	8-Ø20 mm	4-Ø10 mm
9	longitudinal reinforcement ratio, A_{st}/A_g	1.24%	1.45%
10	Tie reinforcement, A_v	Ø10 = 78 mm^2	Ø6 = 28 mm^2
11	Intermediate moment frame (IMF) detailing criteria:		
	(a) Tie spacing, S_o over a length ℓ_o shall not exceed the smallest of:		
	(i) 8 times the diameter of the smallest longitudinal bar.	8 x 20 = 160 mm	8 x 10 = 80 mm
	(ii) 24 times the diameter of the tie bar	24 x 10 = 240 mm.	24 x 6 = 144 mm.
	(iii) ½ of the smallest cross-sectional dimension	½ x 450 = 225 mm.	½ x 150 = 75 mm.
	(iv) 300 mm.	300 mm	300 mm
	Tie spacing considered within the length ℓ_o at both ends	Ø10 @ 150 mm c/c	Ø6 @ 75 mm c/c
	(b) Length ℓ_o shall not be less than the largest of:		
	(i) ⅙ of the clear span	⅙ x 3000 = 500 mm	⅙ x 950 = 158 mm
	(ii) Maximum cross-sectional dimension of the member	450 mm	150 mm
	(iii) 450 mm	450 mm	450 mm
	Length ℓ_o considered at both ends	500 mm	250 mm
	(c) The first tie shall be located not more than $S_o/2$ from joint face.	150/2 = 75 mm	75/2 = 37.5 mm
	(d) Tie spacing shall not exceed $2S_o$ outside the length ℓ_o	2 x 150 = 300 mm.	2 x 75 = 150 mm.

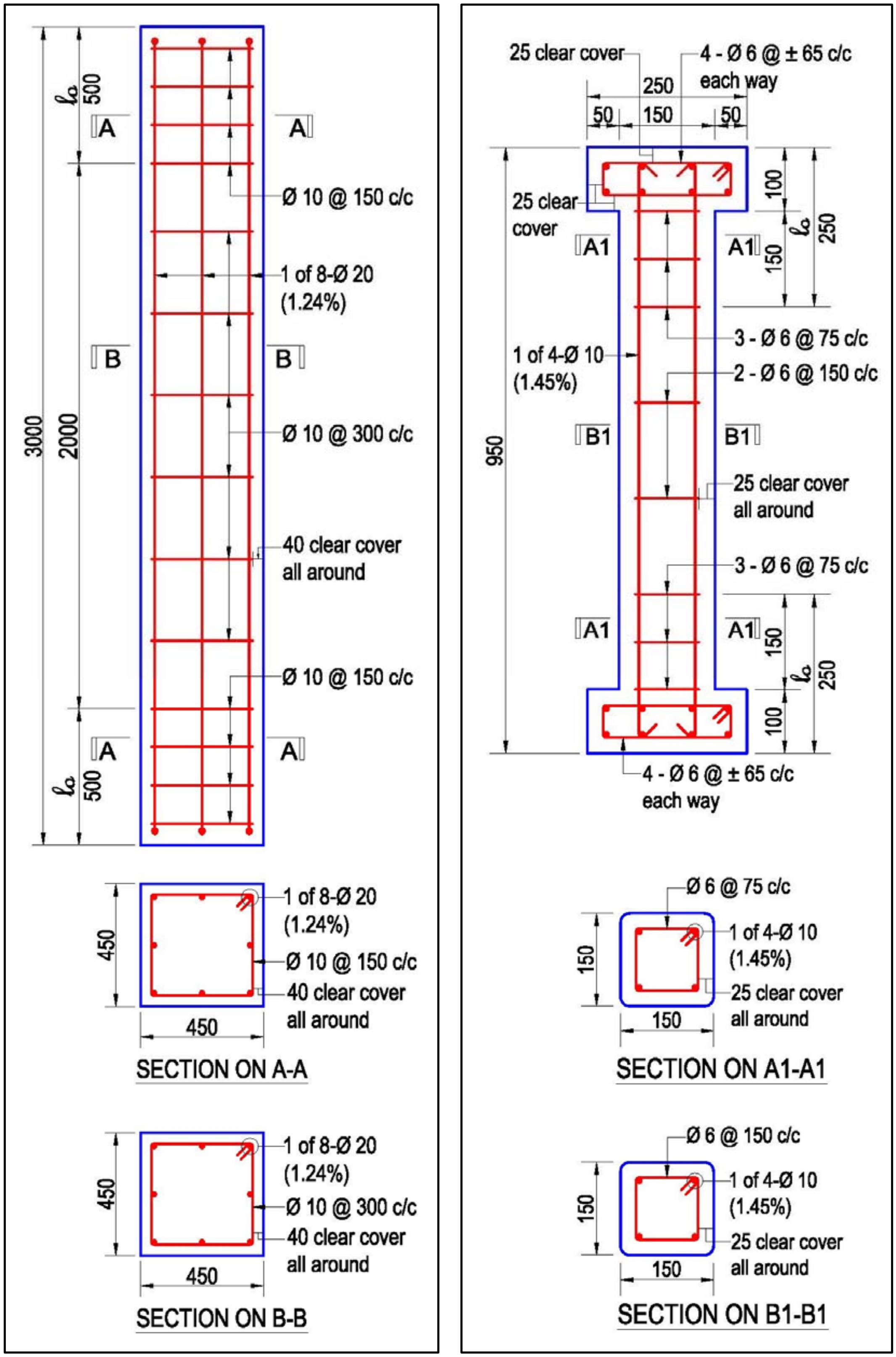

(a) Details of a 450 mm x 450 mm prototype column

(b) Details of a 150 mm x 150 mm model column

Fig. 3.8: Configuration and re-bar details of the prototype and model column.

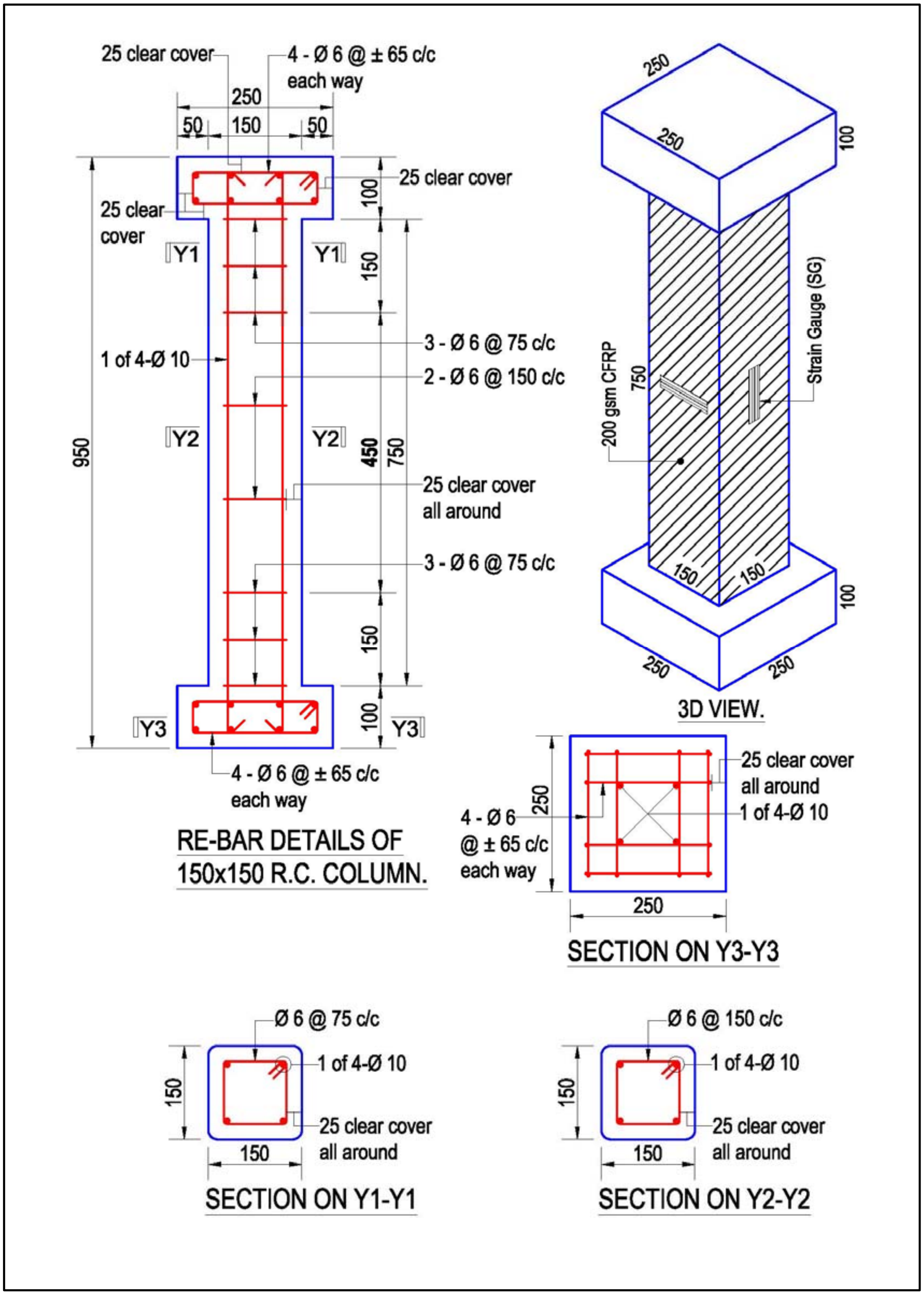

(a) Details of 150 mm x 150 mm column.

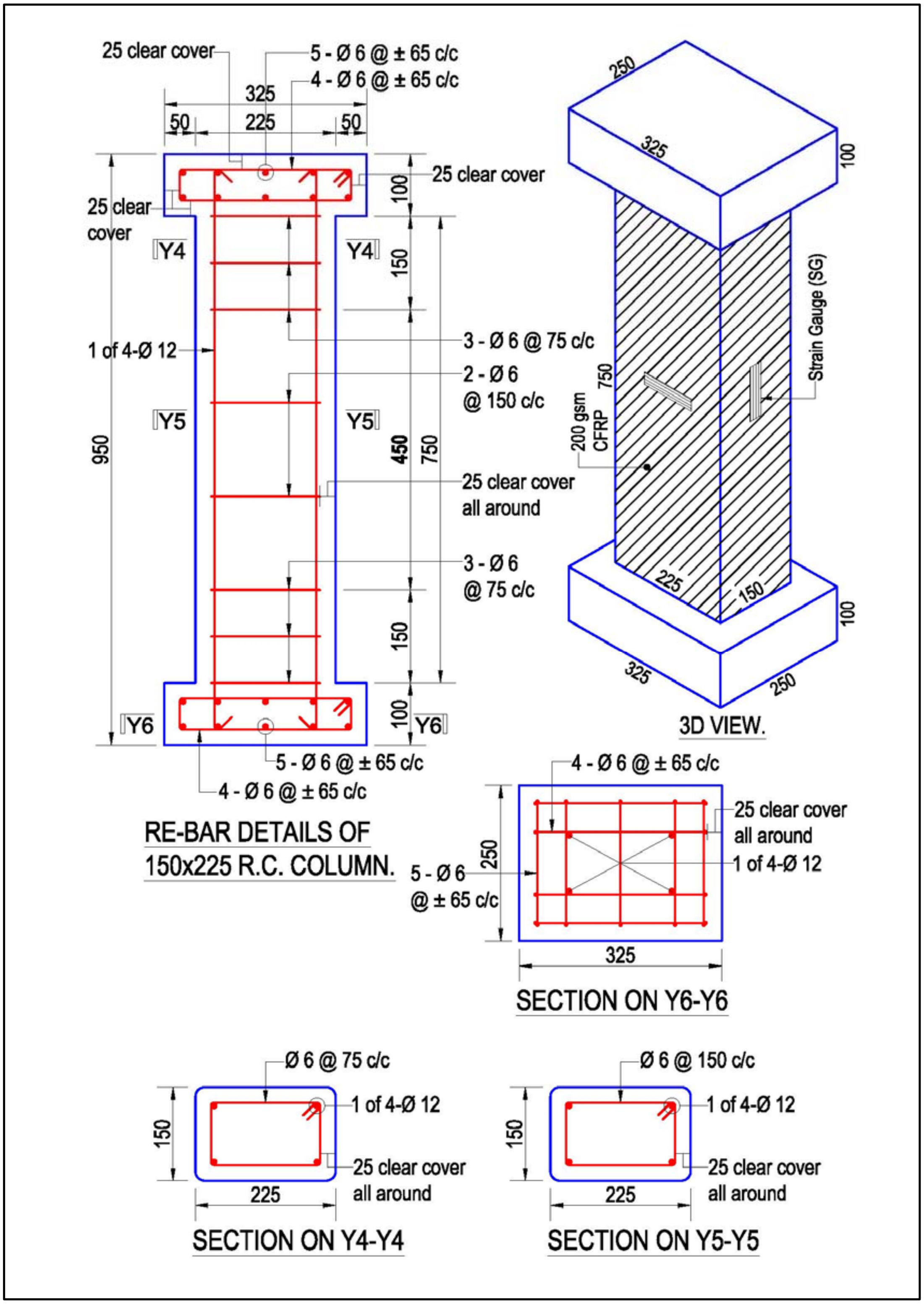

(b) Details of 150 mm x 225 mm column.

Fig. 3.9: Configuration and re-bar details of the column specimen.

3.3.2.2 Fabrication of Reinforcement

In the 150 mm x 150 mm x 950 mm columns, four 10 mm diameter re-bars were used, while four 12 mm diameter re-bars were used in the 150 mm x 225 mm x 950 mm columns as the longitudinal reinforcement (Fig. 3.9 and Fig. 3.10), maintaining a reinforcement ratio of 1.45% and 1.20% respectively which are beyond the limit of 1% - 8% (ACI 318-14, 2014). The specimens were laterally reinforced with 6 mm diameter plain bars, spaced 150 mm center-to-center in the mid-region and 75 mm center-to-center in the potential plastic hinge end regions. To restrain longitudinal re-bar buckling, the vertical spacing of ties should not exceed 16 times of longitudinal bar diameters, and to obtain adequate concrete confinement, the ties should not exceed 48 tie bar diameters or the least dimension of the compression member (ACI 318-14, 2014). Thus, 150 mm tie spacing was selected for the mid-height (450 mm) portion. The other spacing, 75 mm, was chosen for the end zones to minimize the likelihood of column failure in those areas inspired by intermediate moment frame detailing, corresponding to one-half of the smallest cross-sectional dimension of the column extended over the length 250 mm. One of the specimens with dimensions 150 mm x 150 mm x 950 mm was made without lateral ties (Fig. 3.10b and Fig. 3.11) to study the effect of a lack of confinement. Prior to casting, one electrical resistance steel strain gauge was affixed to the longitudinal reinforcement (Fig. 3.10) at mid-height using a special adhesive to collect axial reinforcement strain readings.

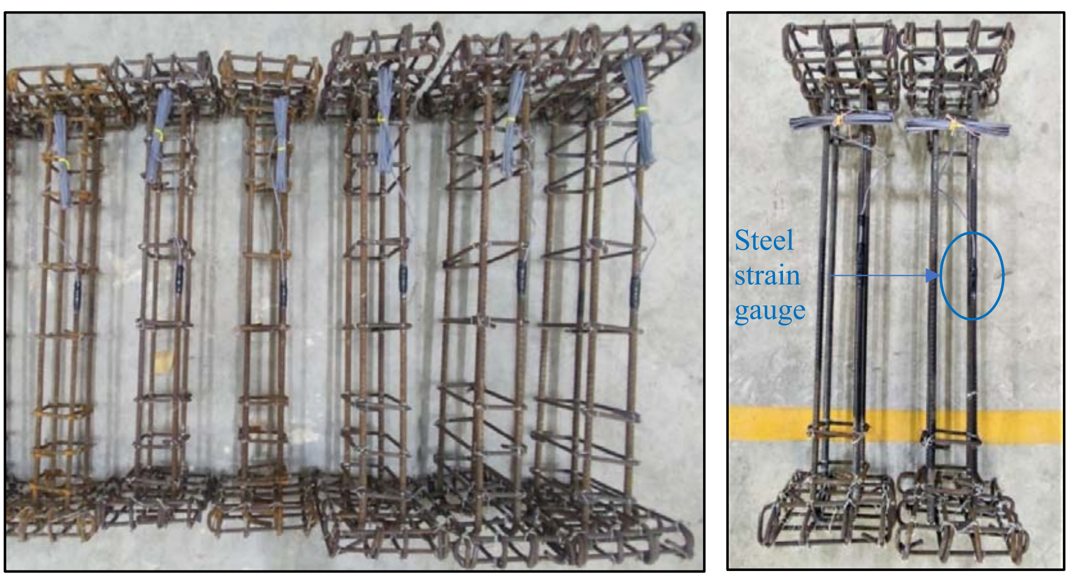

(a) Confined column re-bar cage with steel strain gauge (b) Unconfined columns

Fig. 3.10: Prepared column re-bar cage before casting.

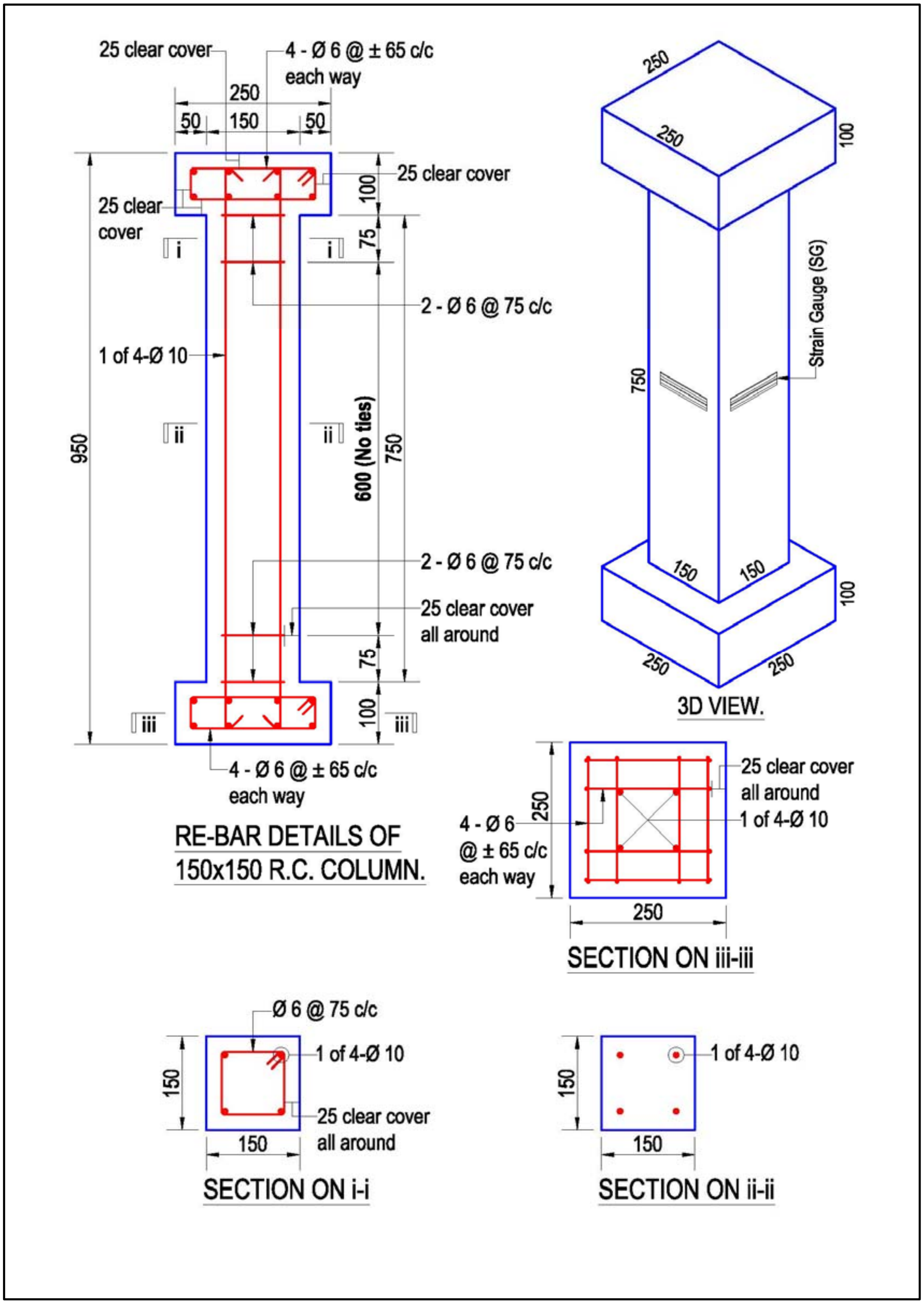

Fig. 3.11: Configuration and re-bar details of the unconfined column.

Table 3.10: Column Test Matrix

S/N	Designation of Column	Strength (f'c)	Sizes of column		Longitudinal Re-bar	CFRP Wrapping Type	Loading Type
			Main Body (b x h x lu)	Top and Bottom Head			
1	17RW1-00	17 MPa	150x150x950	250x250x100	4-10 mm Ø (ρ = 1.45%)	-	Concentric
2	17RW1-45					-	Eccentric (e = 45 mm)
3	17RD1-45					Discrete	
4	17RC1-45					Continuous	
5	17RW2-00		150x225x950	250x325x100	4-12 mm Ø (ρ = 1.20%)	-	Concentric
6	17RW2-90					-	Eccentric (e = 90 mm)
7	17RD2-90					Discrete	
8	17RC2-90					Continuous	
9	10RW1-00	10 MPa	150x150x950	250x250x100	4-10 mm Ø (ρ = 1.45%)	-	Concentric
10	10RW1-45					-	Eccentric (e = 45 mm)
11	10RD1-45					Discrete	
12	10RC1-45					Continuous	
13	10RW2-00		150x225x950	250x325x100	4-12 mm Ø (ρ = 1.20%)	-	Concentric
14	10RW2-90					-	Eccentric (e = 90 mm)
5	10RD2-90					Discrete	
16	10RC2-90					Continuous	
17	10RU1-00	10 MPa	150x150x950	250x250x100	4-10 mm Ø	-	Concentric

Notes: 17 and 10 = Specified concrete strength, R = Recycled brick aggregate, W = Without wrapping, D = Discrete wrapping, C = Continuous wrapping, U = Unconfined by ties, 1 = Type 150 x 150 column, 2 = Type 150 x 225 column, 00, 45 and 90 = Corresponding eccentricity.

3.3.2.3 Concrete Casting

Following the mix design, ingredients were prepared on weight-based proportions for a specific strength of column. In order to coat the surface of all coarse and fine aggregate particles with cement paste and to blend all the ingredients of concrete into a uniform mass, an electrical power based concrete mixer machine was used. Mixer machine hopper was properly watered prior to poring the different ingredients, to avoid absorb water from designated mix design quantities. Firstly, designated amounts of coarse aggregate were poured, thereafter fine aggregate followed by cement was poured and mixed them by dry condition. When the ingredients being uniformly mixed, then the designated quantities of water were added. At least 25 revolution was used over a time period of 3 minutes for each batch of concrete mixing. After mixing, the fresh concrete was poured into the previously prepared water tight formwork with maintaining 25 mm clear cover on ties all around. Casting operation was done by laying of two successive layers of concrete. A mechanical vibrator was used to compact the fresh concrete properly during the casting of specimens. The fabrication of different specimens can be seen in Fig. 3.12.

(a) Formwork with re-bar cage

(b) Mixer machine for concrete mixing

(c) Mixed concrete

(d) Compaction of concrete mix

(e) Casted column specimens

(f) Preparation of cylinder molds

(g) Pouring of concrete mix

(h) Casted cylinder specimens

Fig. 3.12: Preparation of the column and cylinder specimens.

3.3.2.4 Curing of the Specimens

Hydration of cement at a maximum rate can proceed only under condition of saturation. For promoting the hydration of cement and consists of control of temperatures and off the moisture movement from and into the concrete, the specimens were cured for 28 days following the standard practice outlined by ASTM C31/C31M-22 (2022), allowing the concrete to gain strength. The cylinders were submerged in a water tank, while the column specimens were moist-cured under damp hessian cloths. Throughout this process, a consistent curing temperature of 25°C was maintained. Procedures of curing of the cylinder and column specimen are presented in Fig. 3.13.

(a) Curing of the cylinder specimen

(b) Curing of the column specimen

Fig. 3.13: Curing of the cylinder and column specimen.

3.3.2.5 Specimens for Testing Mechanical Properties of Concrete

In line with the ASTM C31/C31M-22 (2022) specifications, a total of eighty-four 100 mm x 200 mm cylinders and twenty 150 mm x 300 mm cylinders were cast. Three of the 100 mm x 200 mm cylinders for each specified strength were wrapped with single and double layers of CFRP. Similarly, two of the 150 mm x 300 mm cylinders for each specified strength were encased in single and double layers of CFRP. The CFRP-wrapped cylinders were set aside for the compressive strength test to compare strength gains with unwrapped cylinders. The remaining cylinders were used to gauge the compressive strength and other hardened properties of the concrete.

3.3.3 Surface Preparation of the Unwrapped Columns

Every column was coated with a whitewash made from a mixture of limestone powder, adhesive, and water. This treatment yielded a well-exposed surface, which was subsequently divided into small 50 mm square grids. This grid pattern facilitated tracking the initial formation and subsequent propagation of cracks on the column surface. After the concrete had fully hardened and reached its optimal strength, the tops of the columns were leveled to ensure that the load applied during testing was uniformly distributed across the column. Surface preparation of unwrapped columns specimens can be seen in Fig. 3.14.

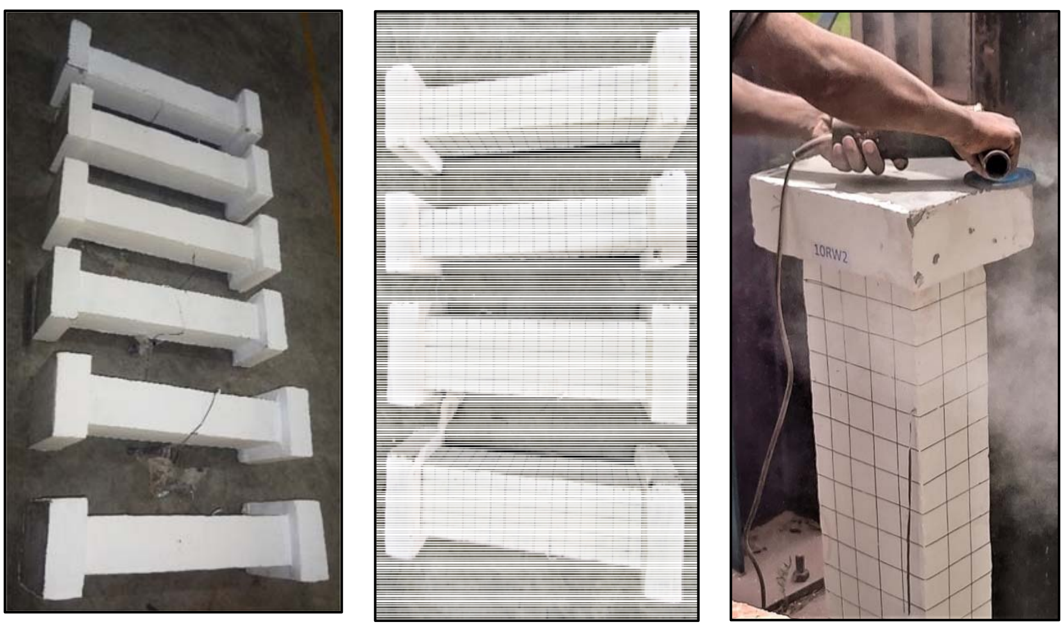

(a) Whitewashed column (b) Gridded columns (c) Head leveling

Fig. 3.14: Surface preparation of unwrapped columns specimens.

3.3.4 Specimens Preparation with CFRP Fabric

Three cylinders, each measuring 100 mm x 200 mm, were prepared for each specified strength, and they were wrapped with either one or two plies of CFRP. Similarly, for each specified strength, two cylinders measuring 150 mm x 300 mm were wrapped with either one or two plies of CFRP. Both size and strength groups included a column with discrete CFRP wrapping and another with a continuous CFRP layer. To prepare the CFRP-wrapped specimens, the fiber was cut to match the sizes of the specimens, as illustrated in the referenced Fig. Installing the CFRP wrapping was meticulously carried out per the ACI 440.2R-17 (2017) guidelines and the manufacturer's (Korea RE & T Co., Ltd.) instructions. The detailed procedure for sample preparation is discussed in the subsequent sections, and the CFRP fabric application methodology flow chart is presented in Fig. 3.15.

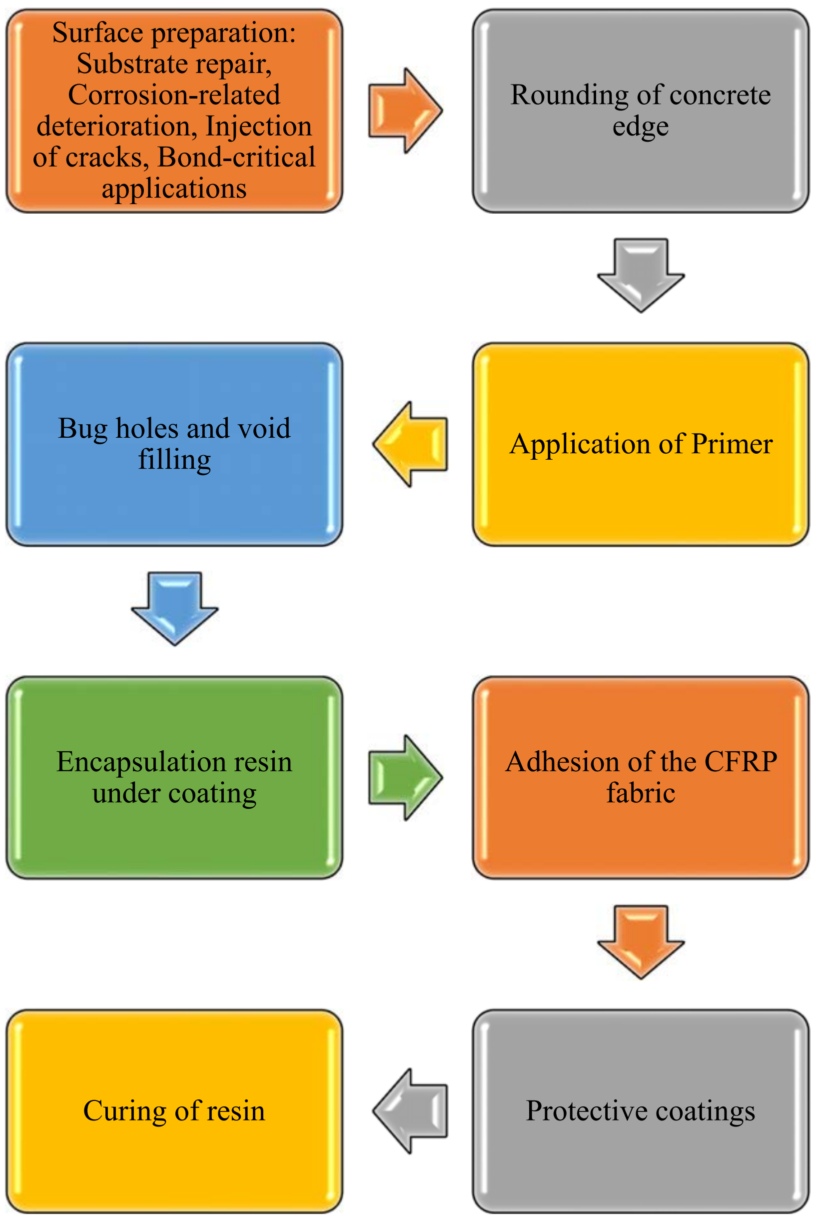

Fig. 3.15: Flow chart of CFRP fabric application methodology.

3.3.4.1 CFRP-Wrapped Columns

(a) Surface Preparation

For the bond-critical application, which necessitates an adhesive bond between the CFRP system and the concrete substrate. Bond-critical application is often used in engineering and construction contexts to emphasize the significance of the bond in maintaining the structural or functional integrity of the components or system. As such the surface of the column was first grinded (Fig. 3.16a). This step was undertaken to eliminate minor surface irregularities (less than 1 mm), remove laitance, dust, and dirt, and achieve a smooth, even finish. The resulting concrete surface profile conformed to CSP 3 (Fig. 3.17c), as defined by ICRI 310.2R (2013). In this experimental study all specimens were newly constructed, and the concrete substrates were not expected to contain actively corroding reinforcing steel. Given that no cracks were observed on the surface, there was no need for pressure-injection with epoxy resin (ACI 440.2R-17). According to ACI 224.1R-07 (2007), any cracks wider than 0.3 mm would have required repair. The column heads were leveled via grinding to ensure the load was distributed uniformly during testing. To remove dust particles and ensure the surface was dry, an air blower was utilized (Fig. 3.16c).

(a) Grinding work (b) Corner radius of column (c) Air blower

Fig. 3.16: Surface preparation of column prior to applying primer.

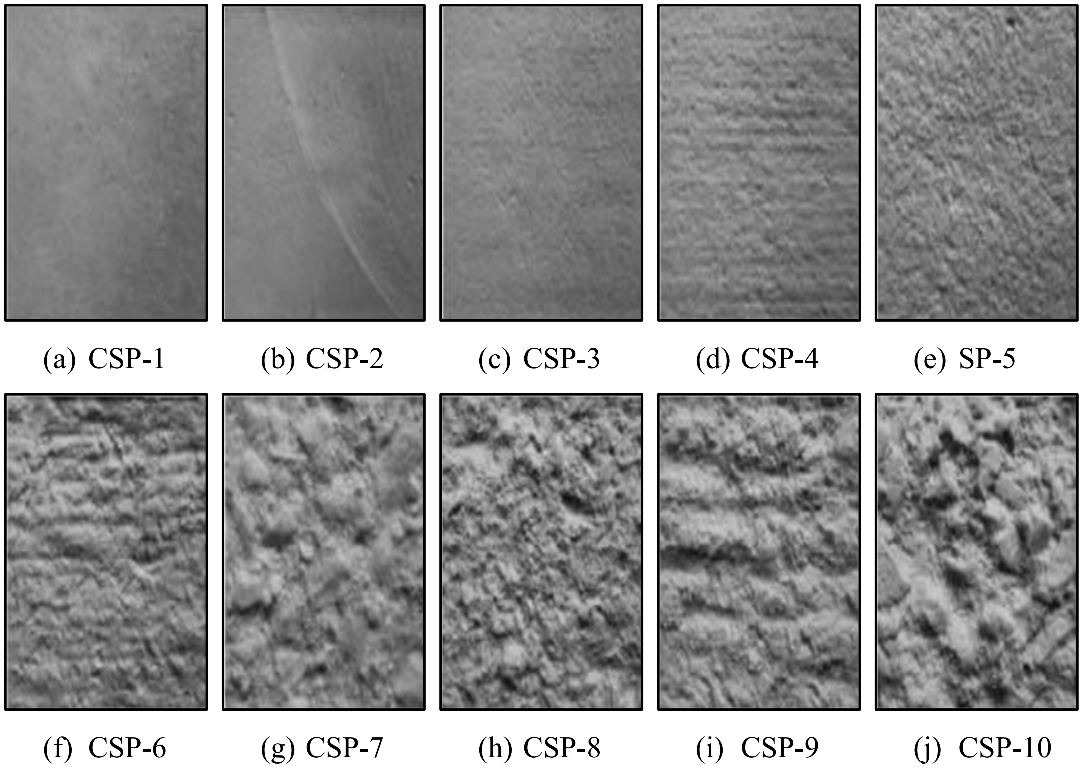

Note: CSP1 being the indicator for a nearly flat floor and CSP10 indicative of an extremely rough floor.

Fig. 3.17: Concrete surface profile inspection guide. *Source*: ICRI 310.2R (2013)

(b) Rounding of Concrete Edge

To minimize stress concentration within the CFRP system and prevent voids between the CFRP ply and the concrete, the corners of the columns were rounded (Fig. 3.16b) during the grinding process. This process ensured a corner radius of 15 mm was achieved, exceeding the minimum radius of 13 mm recommended by ACI 440.2R-17 (2017).

(c) Application of Primer

Before applying the primer, the surface was thoroughly checked to ensure it was free from dust, moisture, and other contaminants. An epoxy resin-based primer was prepared by mixing the base and hardener in a 2:1 weight ratio. This mixture was carefully stirred by hand. The primer was mixed in small quantities at a time to ensure all the mixed resin could be used within the pot life of 74 minutes, as suggested by the manufacturer. The primer was applied uniformly across the entire surface of the column at a rate of 0.25 to 0.3 kg/m^2 using a paintbrush. After application, a curing period of 12 hours was allowed (Fig. 3.18a).

(d) Bug Holes and Void Filling

In cases, where localized out-of-plane variations, bug holes, voids, or other depressions were found in the concrete surface, they were filled with an epoxy resin-based putty using a scraper. Once the putty was applied, an 8-hour curing period was allowed (Fig. 3.18b).

(e) Encapsulation Resin Under Coating

The encapsulation or saturating resin was prepared by mixing the base and hardener in a 2:1 weight ratio, and it was properly mixed by hand stirring. Small quantities of resin were prepared at a time to ensure that all the mixed resin could be used within the resin's pot life of 74 minutes, as recommended by the manufacturer. The encapsulation resin undercoat was applied uniformly to the prepared surface using a paintbrush at a rate of 0.50 to 0.67 kg/m^2 across the entire body surface (Fig. 3.18c). The wet film thickness of the saturant was maintained at an average of 0.25 mm.

(a) Column primed surface (b) Bug holes filling (c) Encapsulation resin undercoating

Fig. 3.18: Surface restoration prior to apply CFRP fabric.

(f) Adhesion of CFRP Fabric

The CFRP fiber was cut to the required size, and the wet layup method was used. After applying the encapsulation resin undercoat, the dry CFRP was wrapped around the column in the circumferential direction (Fig. 3.19a). This was done using a gloved hand and a surface roller to apply gentle pressure, ensuring the wrapping was firmly placed and any trapped air was expelled. A final coat of encapsulation resin was applied over the CFRP-wrapped surface within a 30-minute window, maintaining an average wet film thickness of 0.25 mm to guarantee full saturation of the fibers. An overlap of 150 mm of CFRP was used along the fiber length (circumferential direction of the column), and a 25 mm overlap was used in the vertical direction (transverse). An additional layer of resin was applied to the overlapping region.

(a) Adhesion of CFRP (b) Discrete wrapping (c) Continuous wrapping

Fig. 3.19: CFRP-wrapped columns.

(g) Protective Coatings

In this experimental study, no protective coat was applied. However, after the final encapsulation resin coat was applied, a coarse sand blast could be used as a rendering layer for a final coat of cement-sand plaster, depending on the intended use. Alternatively, painting could also be applied after the final encapsulation resin coat had cured to protect the CFRP surface from degrading because of ultraviolet rays.

(h) Curing of Resin

All column specimens were cured for 28 days at an ambient temperature between 25°C and 35°C prior to testing. It's important to note that the curing of resins is dependent on both time and temperature. Extreme or fluctuating temperatures can either slow down or speed up the resin curing process.

3.3.4.2 Geometry and Specifications of CFRP-Confined Columns

Two columns of each size (150 mm x 150 mm x 950 mm and 150 mm x 225 mm x 950 mm), representing two different strengths (17 MPa and 10 MPa), were wrapped with 210 gsm CFRP fabric. One column was configured with discrete wrapping, and the other with continuous wrapping, while the heads of the columns remained unwrapped (Fig. 3.20). The discrete wrapping method was adopted from the inspiration of Guo et al. (2018) experiments, where they found the strength increment is highly related to the FRP strip clear spacing rather than the FRP strip width under concentric loading. These CFRP-wrapped columns were prepared for testing under eccentric loading conditions. For the columns with discrete confinement, 150 mm wide CFRP straps were arranged vertically at 150 mm center-to-center spacing over a height of 750 mm. Conversely, continuous confinement was achieved using a single layer of CFRP that spanned the entire column height. The specifications for the CFRP were identical for both column sizes.

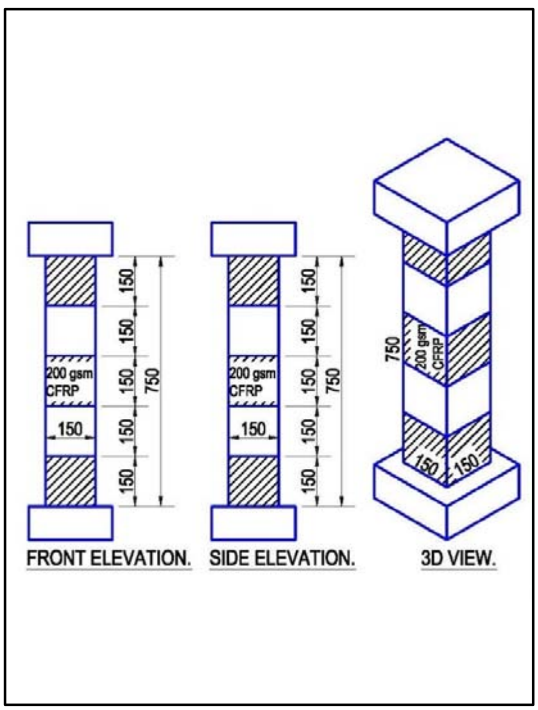

(a) Discrete CFRP wrapped 150 mm x 150 mm x 950 mm column

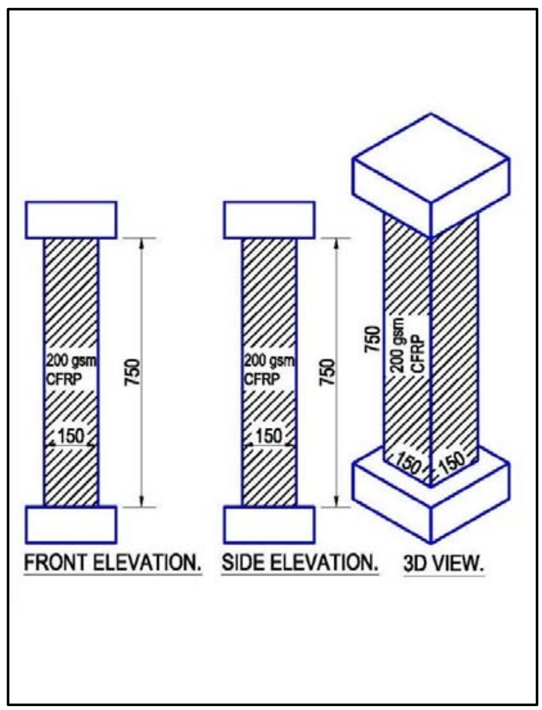

(b) Continuous CFRP wrapped 150 mm x 150 mm x 950 mm column

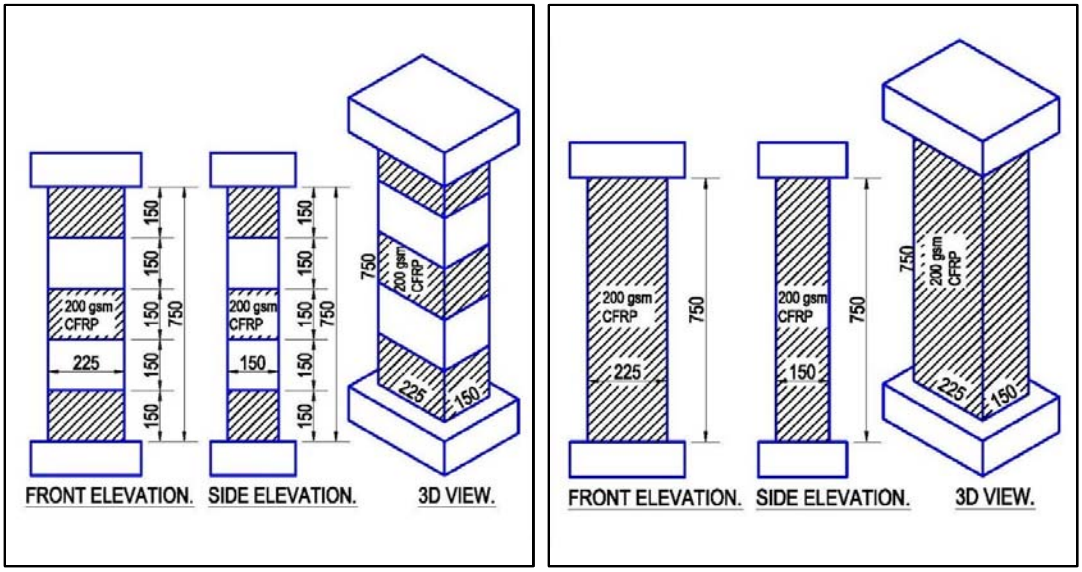

(c) Discrete CFRP wrapped 150 mm x 225 mm x 950 mm column

(d) Continuous CFRP wrapped 150 mm x 225 mm x 950 mm column

Fig. 3.20: Typical geometry of CFRP fabric wrapped column specimens.

3.3.4.3 CFRP-Wrapped Cylinders

In total, 12 cylinders measuring 100 mm x 200 mm and 8 cylinders measuring 150 mm x 300 mm were grinded (Fig. 3.21a) to eliminate minor surface irregularities, similar to the column specimen preparation. The grinding resulted in a smooth, even finish. As no cracks were observed on the surfaces, there was no need for crack injections. Before the primer was applied, the cylinder surface was thoroughly inspected to ensure it was free from dust, moisture, and other contaminants. The primer application (Fig. 3.21b) process mirrored that used for the columns. Once the primer had cured, a system-compatible putty (Fig. 3.21c), essentially a resin-based paste of thicker consistency, was applied to fill any existing voids and smooth out surface discontinuities, following a process similar to that employed with the columns. Following the FRP manufacturer's recommended procedure, the resin was mixed and applied (Fig. 3.21d) to the specimens after ensuring a smooth surface. This application took place 8 hours after filling any bug holes. The CFRP fiber was cut to the necessary size, and the wet layup method was employed. After the application of the encapsulation resin undercoat, dry CFRP was wrapped around the cylinder (Fig. 3.21e) in the peripheral direction. This was done using a gloved hand and a surface roller to apply gentle pressure, ensuring a firm placement of the wrapping and the expulsion of any trapped air. Another coat of encapsulation resin was then applied over the CFRP-wrapped surface within a 30-minute window, maintaining an average wet film thickness of 0.25 mm to guarantee complete saturation of the fibers. In cases involving double plies, an additional complete turn of CFRP fabric was used, with saturant applied between successive layers before the previous layer of resin fully cured. Generally, a 12-hour lapse time was required before applying a subsequent layer of CFRP. For both cylinder sizes, a 100 mm overlap of CFRP was used along the fiber length, with an additional layer of resin applied to the overlapping region. All prepared cylinder specimen for testing presented in Fig. 3.22.

(a) Grinded surface

(b) Primed surface

(c) Application of putty

(d) Application of resin

(e) Application of CFRP

Fig. 3.21: Steps of CFRP application on cylinder.

(a) Single ply-100 mm x 200 mm cylinder for 17 MPa concrete.

(b) Single ply-100 mm x 200 mm cylinder for 10 MPa concrete.

(c) Double plies-100 mm x 200 mm cylinder for 17 MPa concrete.

(d) Double plies-100 mm x 200 mm cylinder for 10 MPa concrete.

(e) Single and double plies of CFRP wrapped 150 mm x 300 mm cylinder for 17 Ma and 10 MPa concrete.

Fig. 3.22: CFRP wrapped cylinders.

3.3.5 Application of Concrete Strain Gauge

In order to measure axial and transverse strain in different column loading conditions, specific strain gauges were used. For concentrically loaded columns, two transverse concrete strain gauges were employed. One gauge was placed on the front face of the concrete surface, while the other was positioned on the adjacent side face. In the case of eccentrically loaded columns, two strain gauges were used. One gauge was placed on the compression face along the axial direction, and the other was affixed to the front face along the transverse direction.

However, when dealing with CFRP (carbon fiber reinforced polymer) confined columns, a slight variation was made in the positioning of the concrete strain gauges. In this case, the gauges were attached to the CFRP surfaces instead of the concrete surface. This adjustment allowed for accurate measurement of strain in CFRP confined columns.

3.3.6 Test Set-up

3.3.6.1 Concentric Loading of Column

A universal testing machine (UTM) with a capacity of 1000 kN was used to test column specimens under concentric loading until failure. The test involved applying load at a controlled displacement rate of 1 mm/min, gradually increasing until failure occurred. Fixed supports were employed at both the top and bottom of the column and a steel plate was used at both ends to ensure the distribution of the load was uniform. The column head was leveled prior to the test. In order to capture strain readings at regular intervals, two concrete strain gauges in the transverse direction, and one reinforcement strain gauge in the longitudinal direction was connected to the automatic data logger. Moreover, four linear variable differential transformers (LVDTs) were positioned at the column's mid-height to monitor the lateral displacement on its four faces.

The UTM was responsible for generating the load and axial deformation data. To document the failure pattern of the columns, a high-resolution camera was used. This allowed for a detailed examination of the recorded videos later, where crack initiation and propagation could be observed to identify the failure modes. The whole actual setup along with schematic drawings presented in Fig. 3.23.

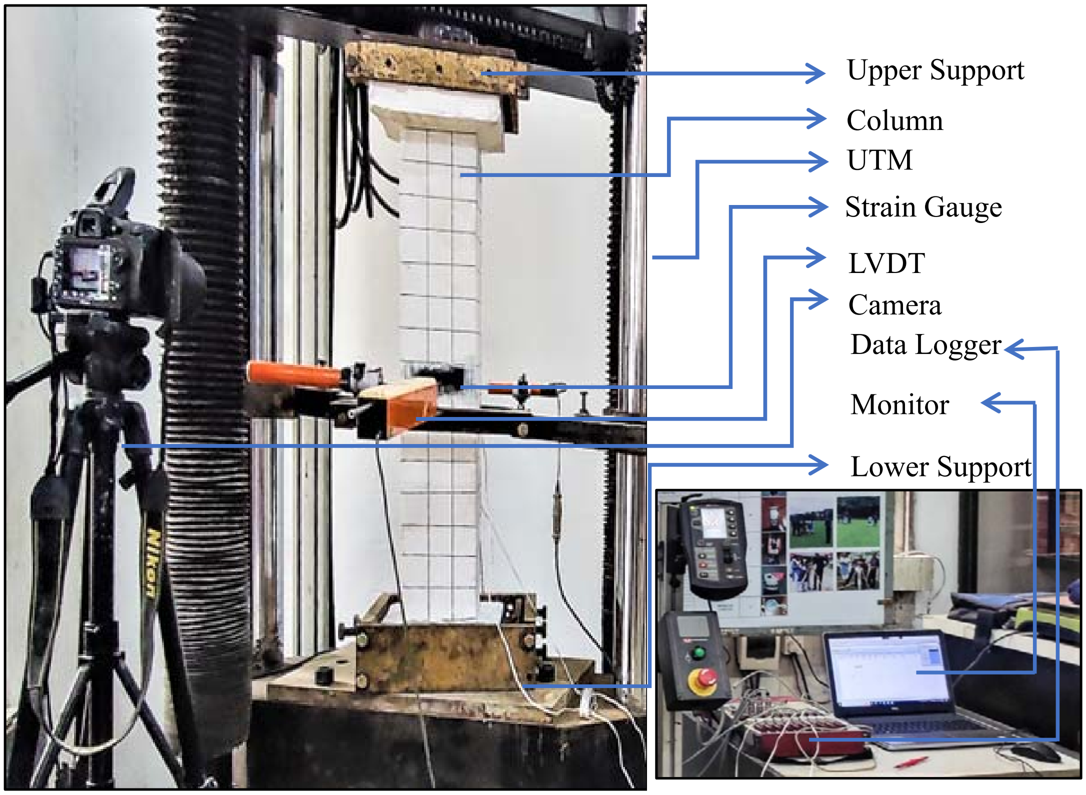

(a) Actual test set-up for concentric loading

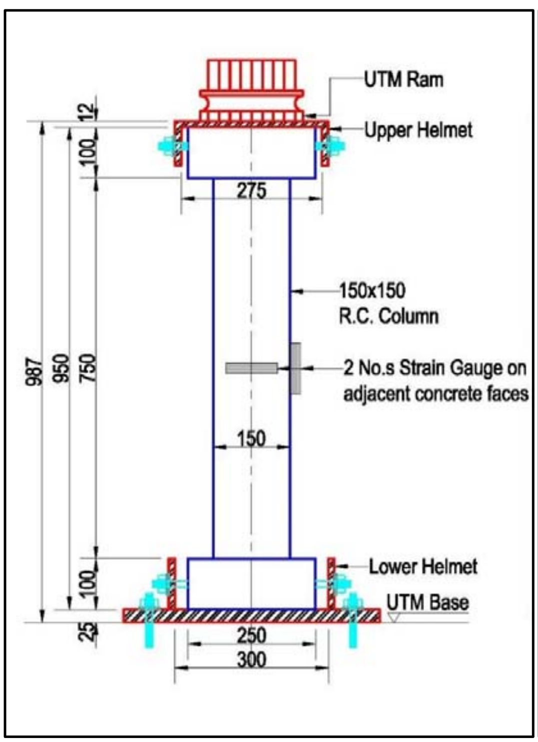

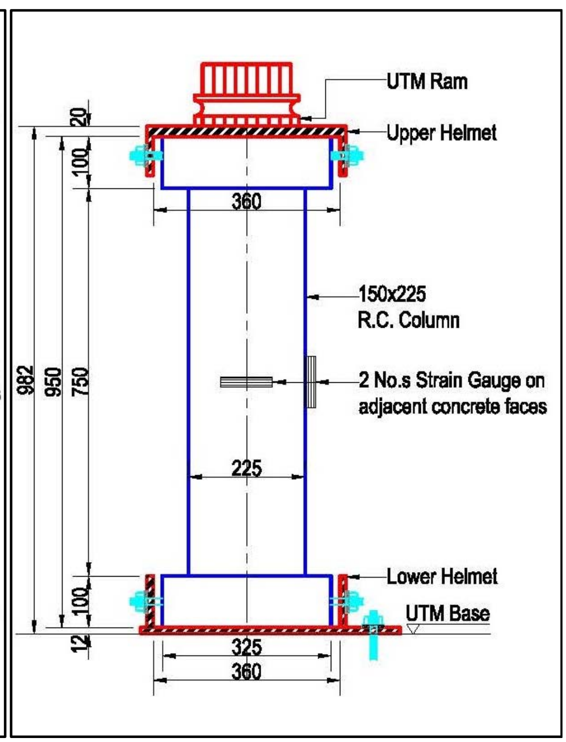

(b) Test set-up of 150 mm x 150 mm column for concentric loading

(c) Test set-up of 150 mm x 225 mm column for concentric loading

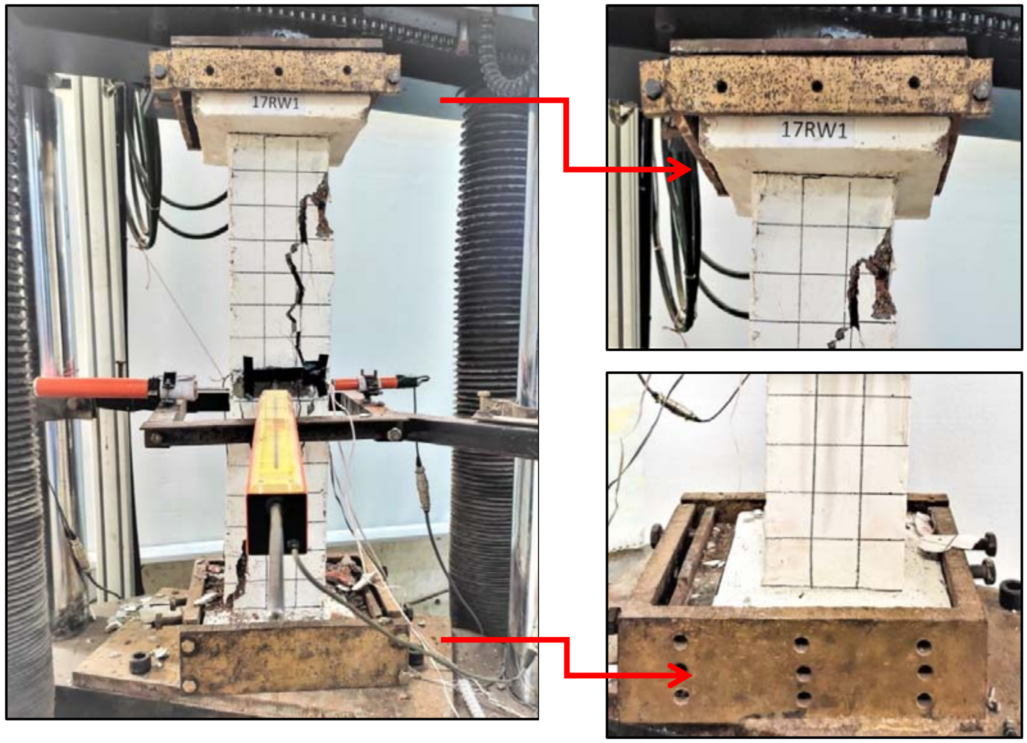

(d) Enlarged view of actual test set-up for concentric loading

Fig. 3.23: Test set-up for concentrically loaded columns.

3.3.6.2 Eccentric Loading of Column

A unique testing setup, illustrated in Fig. 3.24 and Fig. 3.25, was designed to apply eccentric loading on the columns. This setup involved the creation of a new high-strength steel plate, which was positioned on the top and bottom right sides of the column, the points at which the eccentric load was applied. To facilitate the eccentric load, two guide re-bars, each with a diameter of 10 mm, were welded onto the top and bottom steel plates. Additionally, the same setup was implemented on the top and bottom plates of the UTM setup, leading to the formation of a ball joint. The load produced by the UTM was transferred through these steel plates, which then further transferred the load to the columns, generating an eccentric load with a line of action that aligned with the steel rod's axis. This setup was adapted for two eccentricities, 45 mm (30% of h = 150 mm) and 90 mm (40% of h = 225 mm), by laterally adjusting the column specimen's position. Each column was equipped with one reinforcement strain gauge in the longitudinal direction, one concrete strain gauge in the axial direction, and one concrete strain gauge in the transverse direction. All these gauges were connected to the data logger. The linear variable differential transformers were oriented and the loading rate was maintained consistent with the concentric loading tests.

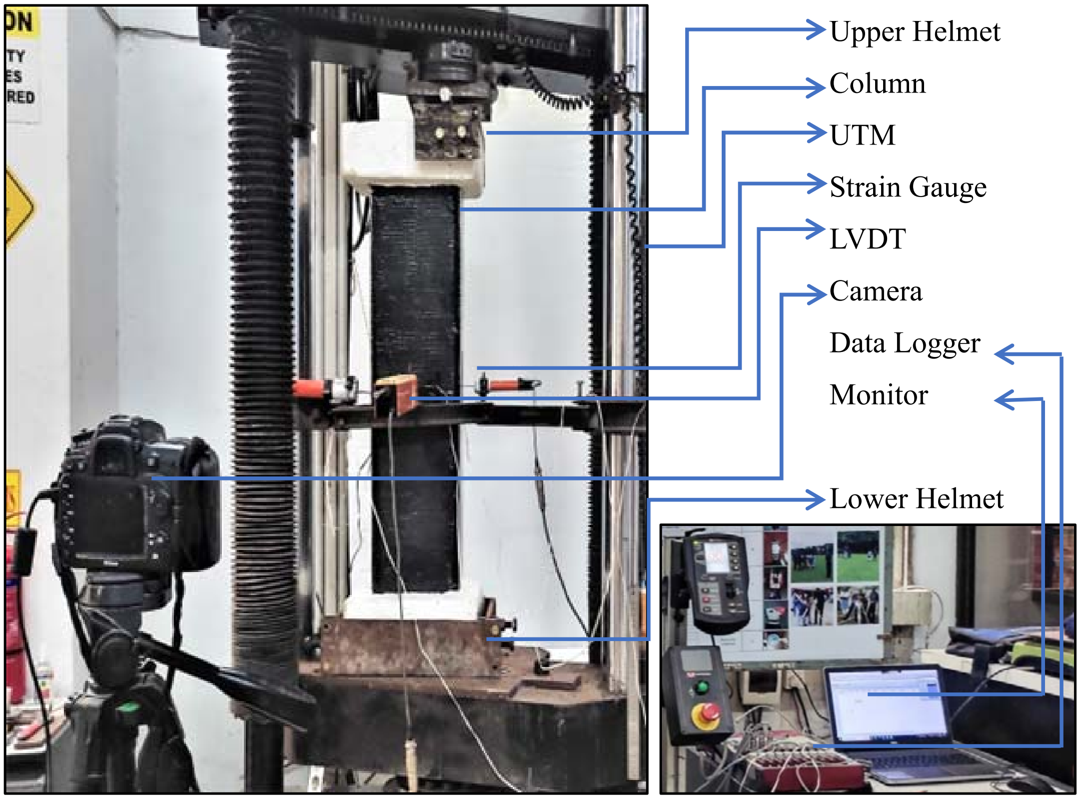

(a) Actual full test set-up in the lab for eccentric loading

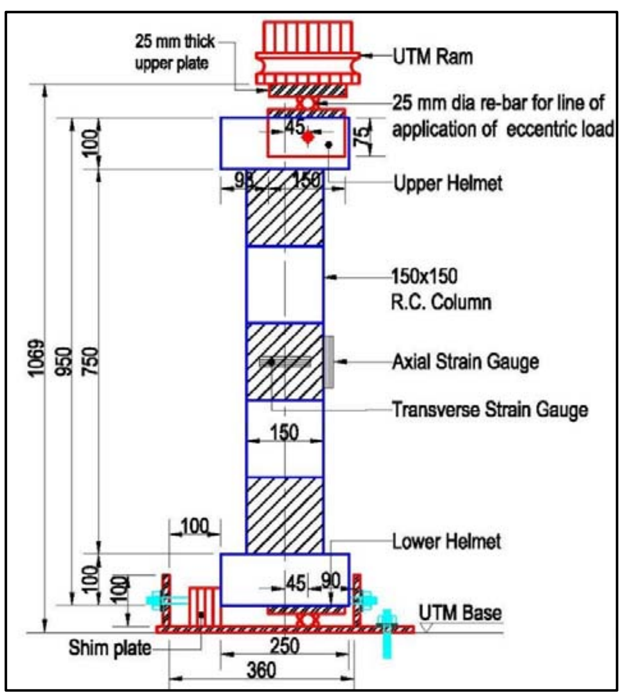

(b) Eccentric test set-up for 150 mm x 150 mm columns with 45 mm eccentricity

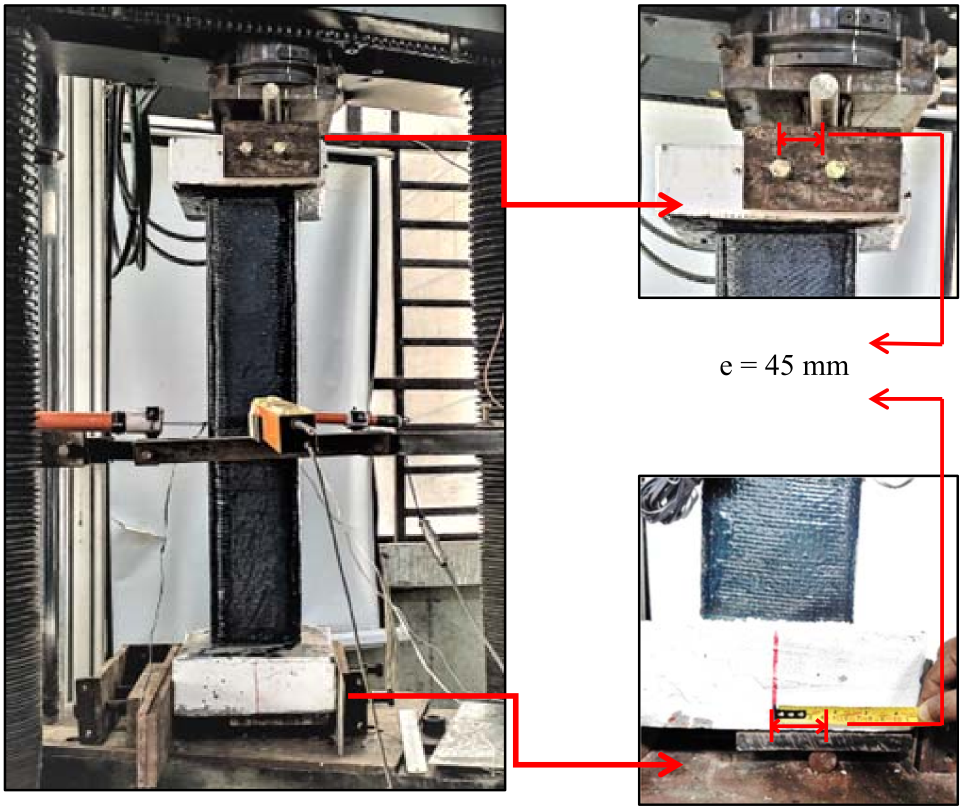

(c) Enlarged view of test set-up for 150 mm x 150 mm column for eccentric loading

Fig. 3.24: Actual eccentric test set-up for 150 mm x 150 mm columns.

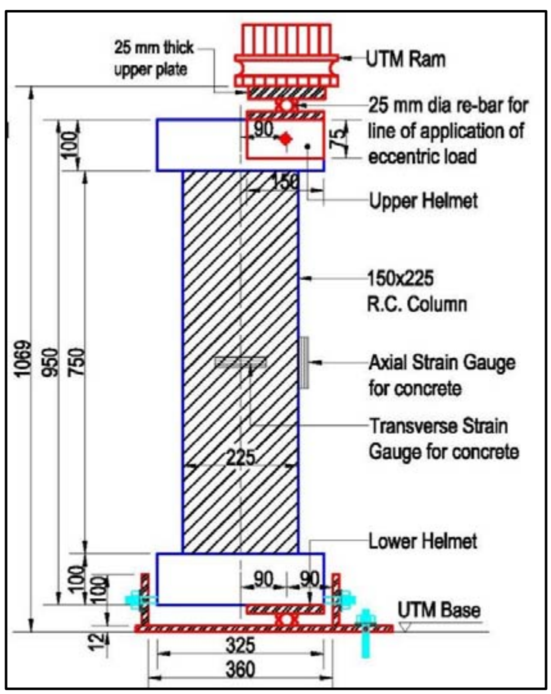

(a) Eccentric test set-up for 150 mm x 225 mm columns with 90 mm eccentricity

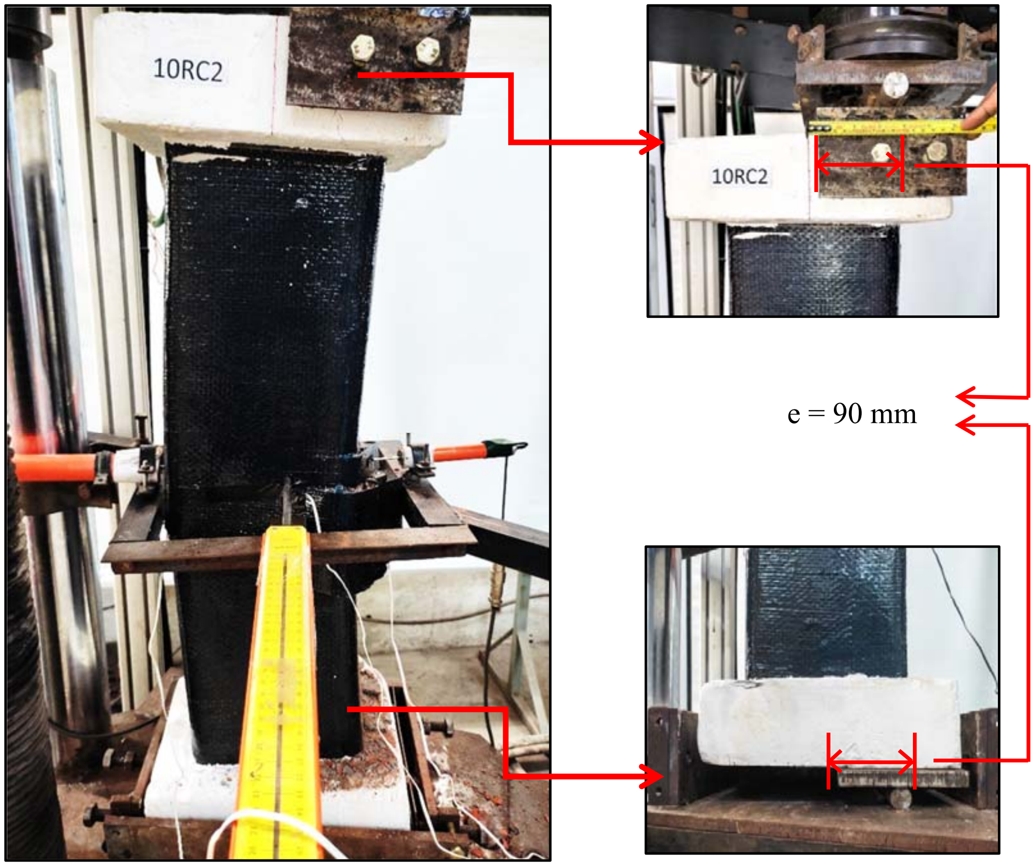

(b) Enlarged view of test set-up for 150 mm x 225 mm column for eccentric loading

Fig. 3.25: Actual eccentric test set-up for 150 mm x 225 mm columns.

3.3.6.3 Cylinder

The compressive strength of the concrete was determined at the age of 28 days and 56 days, in compliance with the standards of ASTM C39/C39M-21 (2021). A compressive strength machine with a minimum capacity of 2000 kN and a loading rate of 4.7 kN/sec was employed. The rubber pads were used at the top and bottom surfaces of the cylinders in the case of compression test only. The stress-strain curves for the cylinders were generated following the procedure outlined by ASTM C469/C469M-22 (2022). The cylinders underwent a compression test with two linear variable differential transformers (LVDTs) attached to track both axial and lateral deformation. These LVDTs were linked to a data logger, which recorded readings at regular intervals. Prior to the test, the top and bottom surfaces of the cylinders were grinded to create a level surface, ensuring that the load application did not induce any eccentricity. The detailed test setup of cylinder is presented in Fig. 3.26.

Fig. 3.26: Test setup of compressive strength of cylinder.

3.4 Summary

This study involved the preparation of eighty-four cylinders of size 100 mm x 200 mm, twenty-one 150 mm x 300 mm cylinders, and seventeen columns of varying sizes and strengths. The purpose of these cylinders was to evaluate the mechanical attributes of the concrete. Meanwhile, the columns were constructed to examine the impact of internal confinement, the use of Carbon Fiber Reinforced Polymer (CFRP) confinement, and the types of loading applied. During the execution of these tests, all standard specifications were strictly adhered to, ensuring the credibility of the results obtained.

CHAPTER 4
RESULTS AND DISCUSSION

4.1 General

The behavior of seventeen distinct combinations of columns under concentric and eccentric loading was examined through several tests, the findings of which are presented in this chapter. The cylinders' fresh properties, compressive strength, failure modes, and the effect of the number of CFRP plies on compressive strength will first be covered. The test results for the columns will then be discussed, beginning with their axial compressive load capacity, bending capacity, load-deformation responses, failure modes, dilation effect, strain in steel and concrete, toughness, ductility, tie bar effect, and comparison with codes.

4.2 Fresh Properties of Concrete During Casting

4.2.1 Slump Value

During casting, a slump test was conducted on the concrete mix in accordance with ASTM C143/C143M-20 (2020). The slump value serves as an indicator of the concrete mix's workability. For this specific mix design, the slump values were recorded as 110 mm and 115 mm. These measurements fall within the 60/80 – 120/150 range, indicating that the concrete mix possesses medium to high workability (Bartos et al., 2002). On the other hand, the slump values represent medium workability according to EN 206:1990. The correlation between the workability and slump value and the slump class as per EN 206:1990 is presented in Table 4.1.

Table 4.1: Degree of workability and class of slump

(Bartos et al., 2002)		EN 206:1990	
Slump (mm)	Degree of workability	Slump (mm)	Class
0	No Slump, Zero Slump	-	-
0-10	Very Low	10-40	S1
10-30	Low	50-90	S2
30-60/80	Medium	100-150	S3
60/80-120/150	High	160	S4
120/150-collapsed	Very High	-	-

4.2.2 Fresh Density

As per the ASTM C138/C138M-17a (2017) guidelines, the density of the freshly mixed concrete was determined to be 2105 kg/m^3 for a water-cement ratio of 0.50 and 2085 kg/m^3 for a water-cement ratio of 0.65. The fresh density provides an insight into the composition of the concrete for a specific mix design, as well as the quantity of air, water, cement, and aggregates it contains.

4.3 Compressive Strength of Cylinder

4.3.1 Without CFRP Confinement

Concrete cylinders of 100 mm x 200 mm sizes were tested at 28 and 56 days to investigate the compressive strength. The findings are shown in Table 4.2 and Fig. 4.1 below. Two different w/c ratios (0.50 and 0.65) were selected with a target of 17 MPa and 10 MPa strength concrete. At 28 days, the average compressive strength of the 17WC50 mix is 17.89 MPa with a standard deviation of 2.69 MPa. In contrast, the 10WC65 mix has an average strength of 13.67 MPa at 28 days with a smaller standard deviation of 1.14 MPa, and which are 5% and 37% higher than the target strengths, respectively. When the testing period is extended to 56 days, both mixes exhibit an increase in strength, as expected with the continued curing of concrete. The 17WC50 mix reaches an average strength of 22.9 MPa at 56 days, with a reduced standard deviation of 1.2 MPa. On the other hand, the 10WC65 mix also shows improved performance with an average strength of 15.29 MPa at 56 days and a standard deviation of 0.97 MPa. The concrete strength is seen to rise by 28% and 12% from 28 to 56 days, respectively. Here, the lower standard deviations indicating more consistent results of the concrete's performance.

Table 4.2: Compressive strength of 100 mm x 200 mm cylinders without CFRP

Designation	28 Day's		56 Day's	
	Average f'_c (MPa)	Standard Deviation	Average f'_c (MPa)	Standard Deviation
17WC50	17.89	2.69	22.90	1.20
10WC65	13.67	1.14	15.29	0.97

Notes: 17WC50 = Specified compressive strength 17 MPa using water cement ratio 0.50, 10WC65 = Specified compressive strength 10 MPa using water cement ratio 0.65.

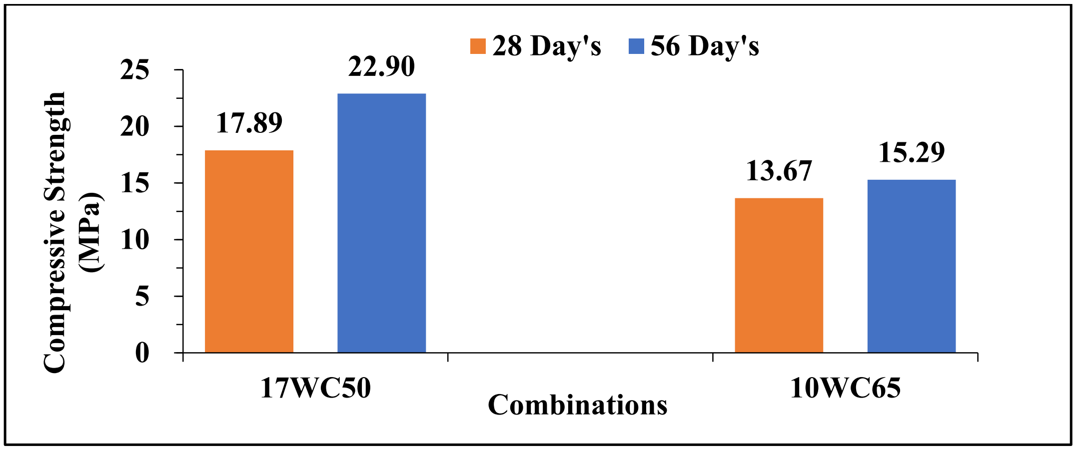

Fig. 4.1: Average compressive strength of 100 mm x 200 mm cylinders.

4.3.2 With CFRP Confinement

The impact of carbon fiber reinforced polymer (CFRP) confinement on the compressive strength of concrete cylinders, with diameters of 100 mm and 150 mm, was investigated. This examination used one-layer (17RFL1 and 10RFL1) and two-layer (17RFL2 and 10RFL2) CFRP jackets. These jackets were continuously wrapped around the concrete cylinders. The results highlighted that the CFRP jackets positively influenced the cylinders' compressive strength enhancement. This enhancement was significant compared to the unconfined cylinders, which did not have the CFRP jackets (17RFL0 and 10RFL0). This data is illustrated in Table 4.3.

Table 4.3: Compressive strength of cylinders with CFRP confinement

Designation	100 mm x 200 mm Cylinder		150 mm x 300 mm Cylinder	
	Average *f'cc* (MPa)	Standard Deviation	Average *f'cc* (MPa)	Standard Deviation
17RFL0	22.90	1.20	24.87	0.63
17RFL1	40.14	0.71	35.11	2.11
17RFL2	60.06	4.62	47.38	0.10
10RFL0	15.29	0.97	10.85	0.30
10RFL1	32.99	2.22	29.54	2.27
10RFL2	49.55	2.53	39.20	4.48

Notes: 17RFL0/17RFL1/17RFL2 = Specified compressive strength 17 MPa using recycled brick aggregate with 0, 1 and 2 layers of CFRP confinement, respectively. 10RFL0/10RFL1/10RFL2 = Specified compressive strength 10 MPa using recycled brick aggregate with 0, 1 and 2 layers of CFRP confinement, respectively.

Fig. 4.2 shows the effect of CFRP confinement for 17 MPa concrete. In Fig. 4.2(a), a marked enhancement in compressive strength for the 100 mm cylinders was observed when a single layer of CFRP was applied, with an upsurge of approximately 75%. When a second layer was added, this increase in strength almost doubled, reaching 162%. An increment of strength around 50% was observed from single to double layer CFRP confinement. For the 150 mm cylinders, the application of one and two layers of CFRP resulted in a strength enhancement of 41% and 91%, respectively, as illustrated in Fig. 4.2(b). In this case, a lower increment around 35% was exhibited from 1 to 2 layer of CFRP confinement. It suggests that the smaller size specimen shows a higher confinement effect. The result for the 150 mm cylinder is similar to that obtained by (Jiang et al., 2020), where the increase in axial load carrying capacity of the 150 mm recycled brick aggregate cylinder was 41% and 90%, respectively, for the application of one and two layers of CFRP confinement. Choudhury et al. (2016) also obtained a 37% increase for 1-ply conferment on a 150 mm recycled brick aggregate cylinder.

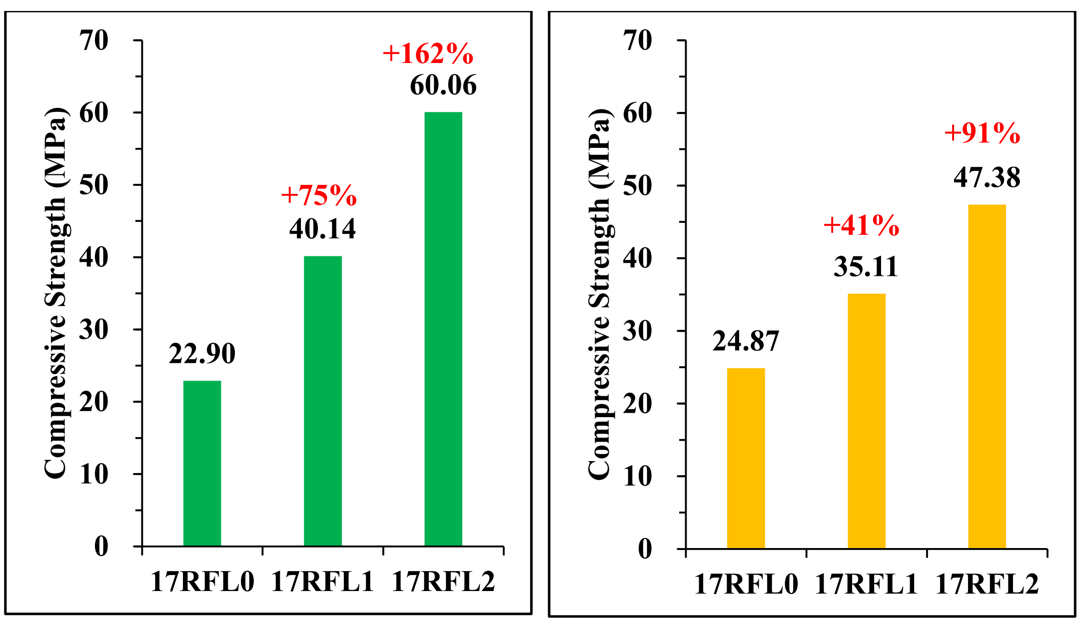

(a) 100 mm x 200 mm cylinders (b) 150 mm x 300 mm cylinders

Fig. 4.2: Compressive strength for two different sizes cylinder and varying numbers of CFRP layers effect on 17 MPa concrete.

Fig. 4.3 shows the effect of confinement for a lower strength concrete, 10 MPa concrete. According to Fig. 4.3(a), the 100 mm cylinders exhibited a strength increment of 116% with a single layer of CFRP confinement and an impressive 224% with two layers. An incremental strength difference around 50% between one, and two layer of CFRP was seen.

In the case of the 150 mm cylinders, a substantial strength increases of 172% and 261% was observed upon applying one and two CFRP layers, respectively, as demonstrated in Fig. 4.3(b). Here, 33% strength increment also observed between the CFRP layers. The increase in compressive strength from one to two layers of CFRP was consistent with the observation made by Seffo and Hamcho (2012), where this increase was 39% for stone aggregate concrete. Hence, between the two concrete cylinder sizes, the application of CFRP jackets contributes more substantially to the strength improvement of the lower-strength concrete. The addition of CFRP layers significantly enhances the strength of these cylinders.

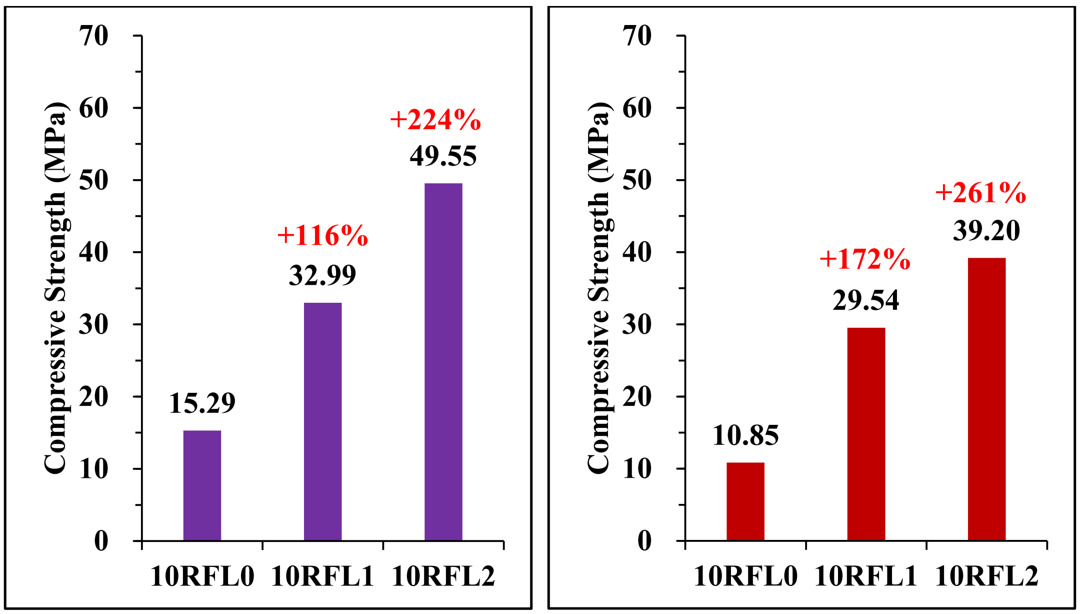

(a) 100 mm x 200 mm cylinders (b) 150 mm x 300 mm cylinders

Fig. 4.3: Compressive strength for two different sizes cylinder and varying numbers of CFRP layers effect on 10 MPa concrete.

4.4 Failure Patterns of Cylinder

Fig. 4.4 presents the observed failure patterns in compressive strength tests of cylinders measuring 100 mm x 200 mm. The unconfined specimens, namely 17RFL0 and 10RFL0, demonstrated shear failure. In contrast, the cylinder, confined with a single CFRP layer, experienced a sudden rupture along with an explosive sound indicative of brittle behavior. Specimens 17RFL2 and 10RFL2, as shown in Fig. 4.4(c) and Fig. 4.4(f), respectively, also displayed a brittle failure pattern. Here, the CFRP layer tore more slowly and progressively. A comparison between 17RFL1, 10RFL1 (Fig. 4.4b) and (Fig. 4.4e) and 17RFL2, 10RFL2

(Fig. 4.4c) and (Fig. 4.4f) reveals that cylinders reinforced with two layers of CFRP remained more intact post-failure than their single-layer counterparts.

(a) 17RFL0

(b) 17RFL1

(c) 17RFL2

(d) 10RFL0

(e) 10RFL1

(f) 10RFL2

Fig. 4.4: Failure pattern of the 100 mm x 200 mm cylinders.

Fig. 4.5 draws attention to the larger concrete cylinders, with 150 mm x 300 mm dimensions. The unconfined samples, referred to as 17RFL0 and 10RFL0 (Fig. 4.5a) and (Fig. 4.5d), revealed a prominent vertical crack extending throughout the entire height of the cylinder. When observing the cylinders reinforced with a single layer of CFRP, labeled as 17RFL1 and 10RFL1 (Fig. 4.5b) and (Fig. 4.5e), considerable tearing in the CFRP layer was evident. This damage was associated with a combination of cone and split failure modes within the concrete's core. In contrast, cylinders reinforced with two layers of CFRP, specifically 17RFL2 and 10RFL2 (Fig. 4.5c) and (Fig. 4.5f), showed a more restrained cone and shear failure mode. In these cases, the CFRP layer tore along the full height of the cylinder. (Jiang et al., 2020) and (Nadim et al., 2019) also observed similar failure modes. When inspecting all the specimens confined with CFRP across both size categories, a robust bond was observed between the surfaces of the cylinders and the CFRP layers. Significant note is that the failure did not start at the areas where the CFRP layers overlapped.

(a) 17RFL0

(b) 17RFL1

(c) 17RFL2

(d) 10RFL0

(e) 10RFL1

(f) 10RFL2

Fig. 4.5: Failure pattern of the 150 mm x 300 mm cylinders.

4.5 Tensile Strength of Cylinder

The cylinders underwent a split tensile test at 56 days, adhering to ASTM C496/C496M-17 (2017) standards. The same machine used for the compressive strength test was used to apply a diametrical compressive load to the cylinder. As depicted in Fig. 4.6, the cylinder was positioned laterally within the machine. The measured split tensile strength of the concrete at 56 days was 2.94 MPa and 1.90 MPa, corresponding to specified compressive strengths of 17 MPa and 10 MPa, respectively.

(a) Test set-up (b) Tested specimen (c) Inside of the failed specimen

Fig. 4.6: Split tensile test of cylinder.

4.6 Columns Subjected to Concentric and Eccentric Axial Force

4.6.1 Axial Load Capacity of the Concentrically Loaded Columns

Fig. 4.7 compares the axial load-carrying capacity of the different combinations of all seventeen columns and shows how column sections lose their axial capacities if eccentricity is introduced. The axial capacity of columns increased with the increase in cross-section, specified compressive strength, and tie application. From Fig. 4.7, under concentric loading, the 150 mm x 225 mm unwrapped rectangular column specimen with 17 MPa strength namely 17RW2-00's axial capacity increased by 34% over the 150 mm x 150 mm unwrapped square column specimen with 17 MPa strength that is to say 17RW1-00's, and the 150 mm x 225 mm unwrapped rectangular column specimen with 10 MPa strength that is 10RW2-00's increased by 41% over the 150 mm x 150 mm unwrapped square column specimen with 10 MPa strength to be specific 10RW1-00's, although the column's cross-section area increased by 50%. The fact that 10RW1-00 is 20% more than 10RU1-00 demonstrates the impact of shear reinforcement on the column's ability to support loads. In a study conducted by Ilki et al. (2008), they found a 90% axial capacity increase under concentric loading on a 10.94 MPa concrete substrate with 1 ply continuous CFRP for 250 mm square and 500 mm high columns.

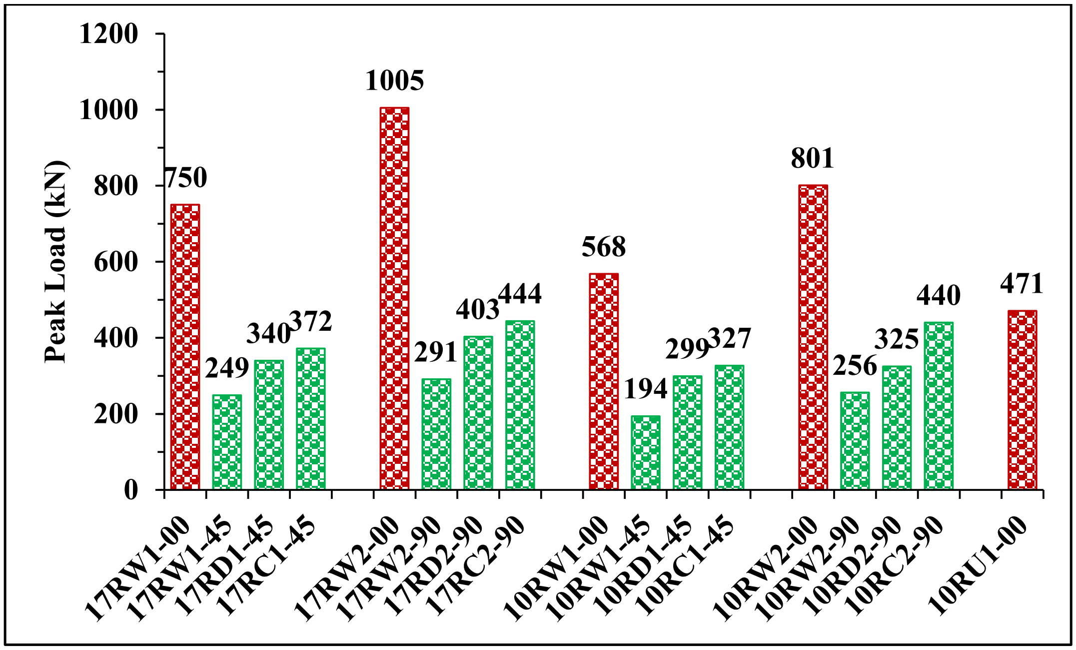

Fig. 4.7: Comparison of the peak loads of the all 17 columns.

4.6.2 Axial Load Capacity of the Eccentrically Loaded Columns

The axial load capacity of the eccentrically loaded columns is shown in Fig. 4.8. As a result of the bending caused by the eccentricity, a lower peak load is observed. Concerning the similar unwrapped controlled columns, the discrete CFRP layers increased axial capacity in the 45 mm eccentricity of 150 mm x 150 mm square columns by approximately 37% for 17RD1-45 and 54% for 10RD1-45 with 17 MPa and 10 MPa concrete strength respectively. On the other hand, 17RC1-45 and 10RC1-45, using continuous wrapping boosts capacity by 49% and 69%, respectively. This increase was observed to be 38% and 27% for discrete wrapping and 53% and 72% above the corresponding unwrapped controlled column for the 150 mm x 225 mm columns with 90 mm eccentricity for 17 MPa and 10 MPa concrete strength respectively. This research supports the findings of Parvin and Wang (2001), who discovered that adding one layer of continuous CFRP to small-scale square columns (b = 108 mm, h = 305 mm) with 21.4 MPa concrete strength increased their axial capacity by 48% under eccentric loading (e = 15.20 mm). Ilki et al. (2008) found a 40% increased axial capacity for a 150 mm x 300 mm rectangular column under concentric loading for a 10.94 MPa strength column made from natural gravel aggregate wrapped with 1-ply continuous CFRP. From discrete to continuous wrapping, the CFRP confinement area increased by 66%, but an increment of the axial capacity of 9% was observed for specimens 17RC1-45 and 10RC1-45. Moreover, a 10% increase was observed in 17RC2-90 and 35% in 10RC2-90. The 150 mm x 225 mm continuously wrapped rectangular column specimen with 10 MPa strength under 90 mm eccentricity that is 10RC2-90 exhibits abruptly higher axial load capacity say 35% increment over corresponding discrete specimen 10RD2-90 due to concrete dilated more effectively and displayed a greater stiffness gain from CFRP confinement.

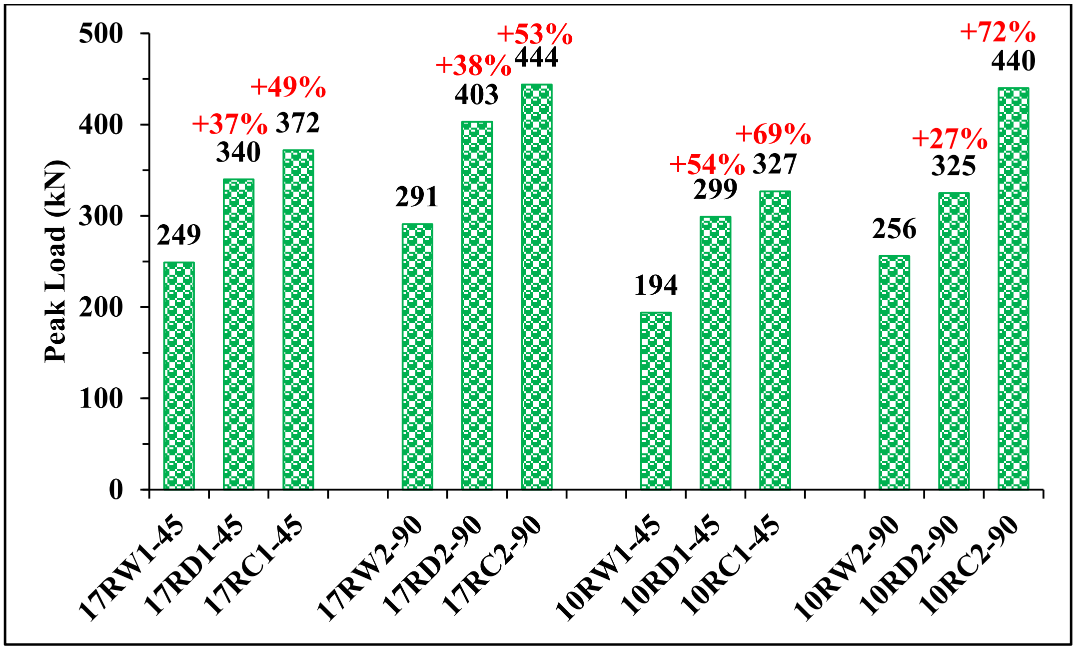

Fig. 4.8: Comparison of the peak loads of the eccentrically loaded columns.

4.6.3 Bending Moment Capacity

4.6.3.1 Bending Moment Capacity at Mid-Height of the Column

The effect of eccentricity in the loading reduces the load-carrying capacity of the columns, generating a bending moment. The bending moment capacity (M_{max}) of the eccentrically loaded columns at mid-height was calculated by multiplying the maximum load capacity (P_{peak}) and the sum of eccentricity (e) and lateral deflection (Δ, measured by the extension of LVDT-1 towards left) at the peak load as follows:

$$M_{max} = P_{peak}\,(e + \Delta) \tag{4.1}$$

The experimental bending moment capacity of the columns is displayed in Fig. 4.9. It can be seen that for the 150mm x 150mm columns, the addition of discrete CFRP wrapping increased the bending moment capacity by 36% for 17RD1-45 and 55% for 10RD1-45. In contrast, a more significant increment is reported when a continuous layer of CFRP is added, where the bending moment capacity improves by 56% for 17RC1-45 and 74% for 10RC1-45. In the 150 mm x 225 mm columns, adding a partial layer of CFRP increased the bending capacity by 37% for 17RD2-90 and 32% for 10RD2-90, respectively. Regarding continuous CFRP wrapping, 54% and 81% bending capacity increments were observed. After increasing the CFRP confinement area about 66% i.e from discrete to continuous wrapping, an increment of bending capacity 12% was observed for the specimen 17RC1-45 and 13% for 10RC1-45. Moreover, 11% increase exhibited in 17RC2-90 and 38% for 10RC2-90.

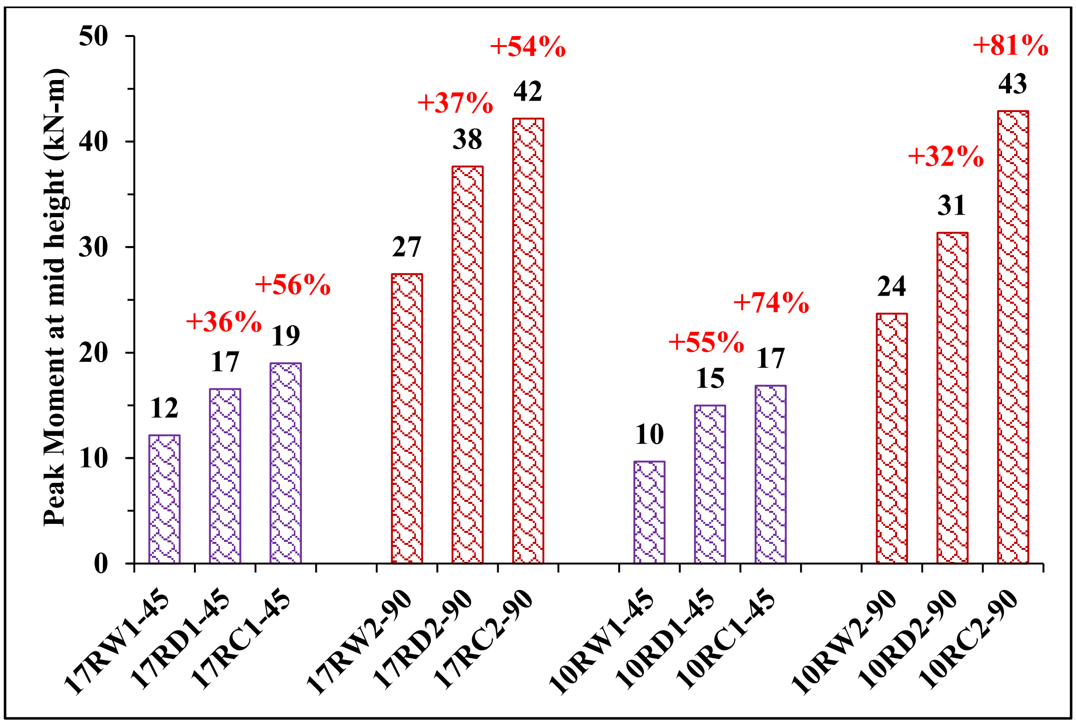

Fig. 4.9: Peak moment at the mid-height for the eccentrically loaded columns.

4.6.3.2 Bending Moment Capacity at Top/Bottom of the Column

The bending moment capacity (M_{max}) of the eccentrically loaded columns at the end was calculated by multiplying the maximum load capacity (P_{peak}) and the stipulated eccentricity (e) as follows:

$$M_{max} = P_{peak} \times e \tag{4.2}$$

The experimental bending moment capacity of the columns is displayed in Fig. 4.10, and it can be seen that the addition of either partial or continuous CFRP confinement increased the bending moment capacities significantly. In all cases, a higher percentage of increment was observed for lower specified concrete strength columns. Regardless the column size and strength, a minimum of 27% and maximum of 54% bending moment capacity increment was observed in discrete confined column over unwrapped specimen. On the other hand, an increment of bending moment capacity of 49% to 72% also seen in continuously CFRP confined columns compared to the unconfined columns.

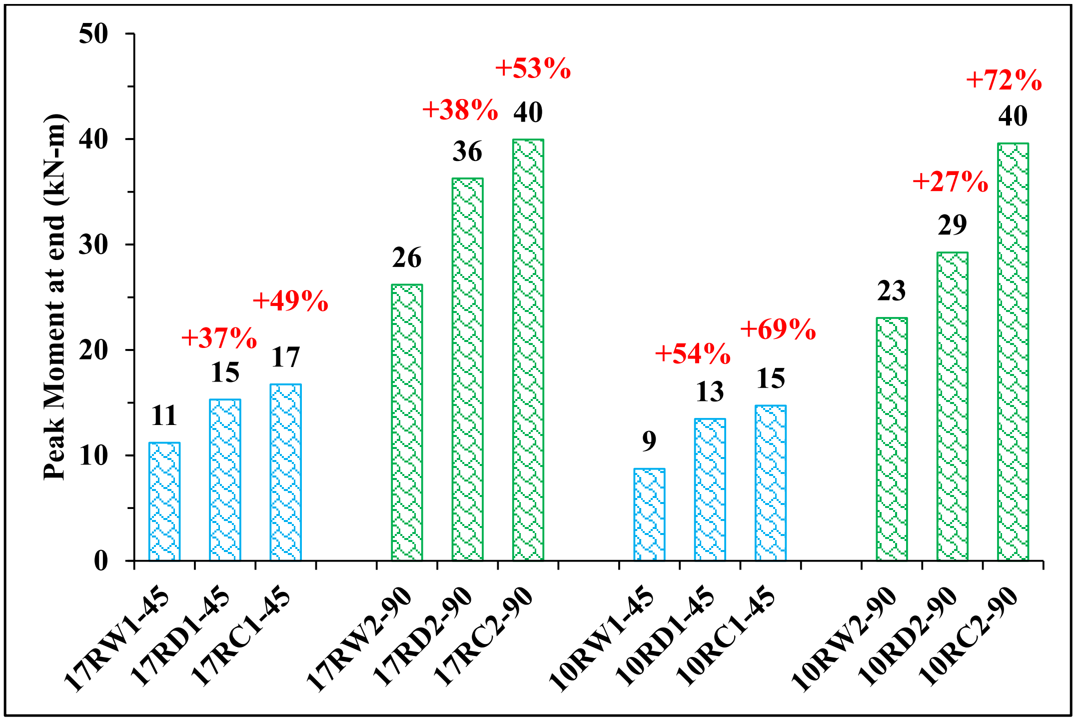

Fig. 4.10: Peak moment at the end for the eccentrically loaded columns.

4.6.4 **Load-Deformation Responses**

The load-deformation curves of the columns are presented in Fig. 4.11, Fig. 4.12, and Fig. 4.13. For the concentrically loaded columns, the load-deformation behavior can be outlined in one way, as illustrated in Fig. 4.11, and the curves for the eccentrically loaded columns show a different behavior, as shown in Fig. 4.12 and Fig. 4.13. For the concentrically loaded columns, the load is observed to increase rapidly up to the peak load, after which a sudden drop in the bearing capacity is experienced. In contrast, for the eccentrically loaded columns, the post-peak regions of the curves are more extended, showing large deformations in general.

4.6.4.1 Concentrically Loaded Columns

It can be shown from Fig. 4.11 for the concentrically loaded columns that 10RU1-00 showed the least deformation among the five columns, whereas 17RW2-00 reached the highest load. Due to the absence of internal reinforcement confinement, 10RU1-00 subjected to a 17% lower peak load than 10RW1-00 and demonstrated 21% less deformation. However, among them, 10RW2-00 exhibits the most distortion after yielding. Peak load increased by 34% as column size increased; however, peak load deformation decreased by 24%, from 17RW1-00 to 17RW2-00.

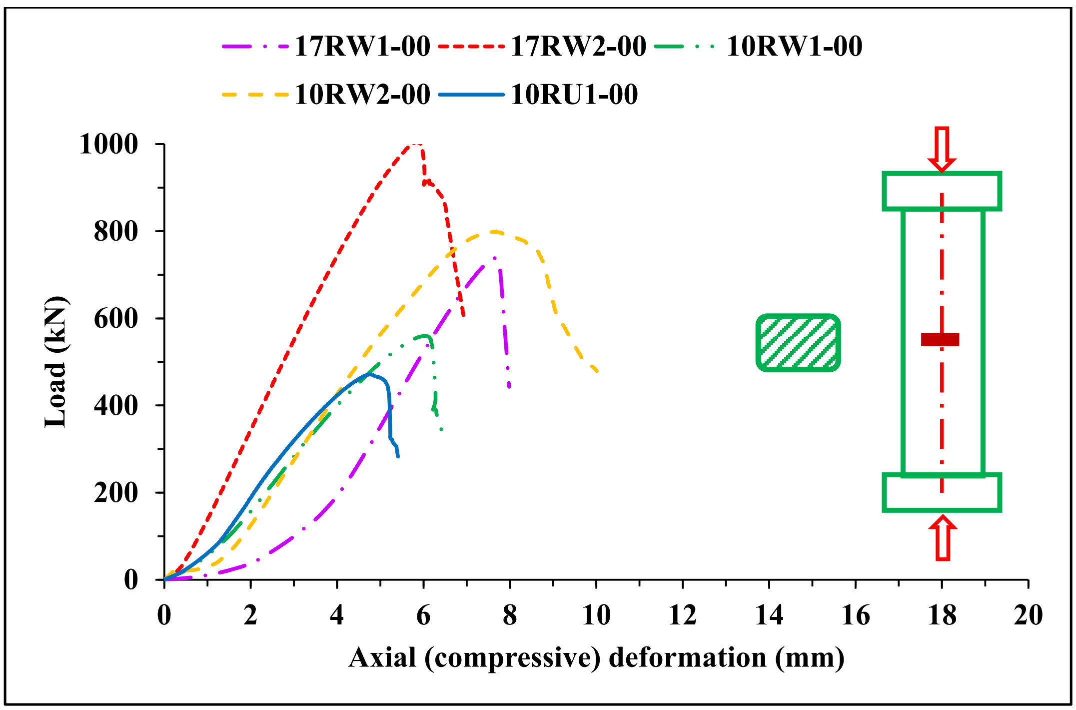

Fig. 4.11: Load-deformation interaction of the concentrically loaded columns.

4.6.4.2 Eccentrically Loaded 150 mm x 150 mm Columns

The behavior of the two varied strength 150 mm x 150 mm x 950 mm columns under 45 mm eccentricity and variable confinement effect is shown in Fig. 4.12. The peak load of 17RD1-45 increased by 37% when discrete CFRP wrapping was used, while a 49% increase was seen when 17RC1-45 over 17RW1-45 was wrapped continuously. On the other hand, 10RD1 and 10RC1 experienced peak load increases above 10RW1-45 of 54% and 69%, respectively. For 17RW1-45, 17RD1-45, and 17RC1-45, the corresponding deformation to the peak load was 8.20 mm, 5.98 mm, and 7.25 mm, respectively. The measurements that correspond for 10RW1-45, 10RD1-45, and 10RC1-45 are 6.69 mm, 8.04 mm, and 9.01 mm. Since the failure occurred in an unconfined zone, discrete wrapping exhibits substantially less deformation in this instance than their peak loads.

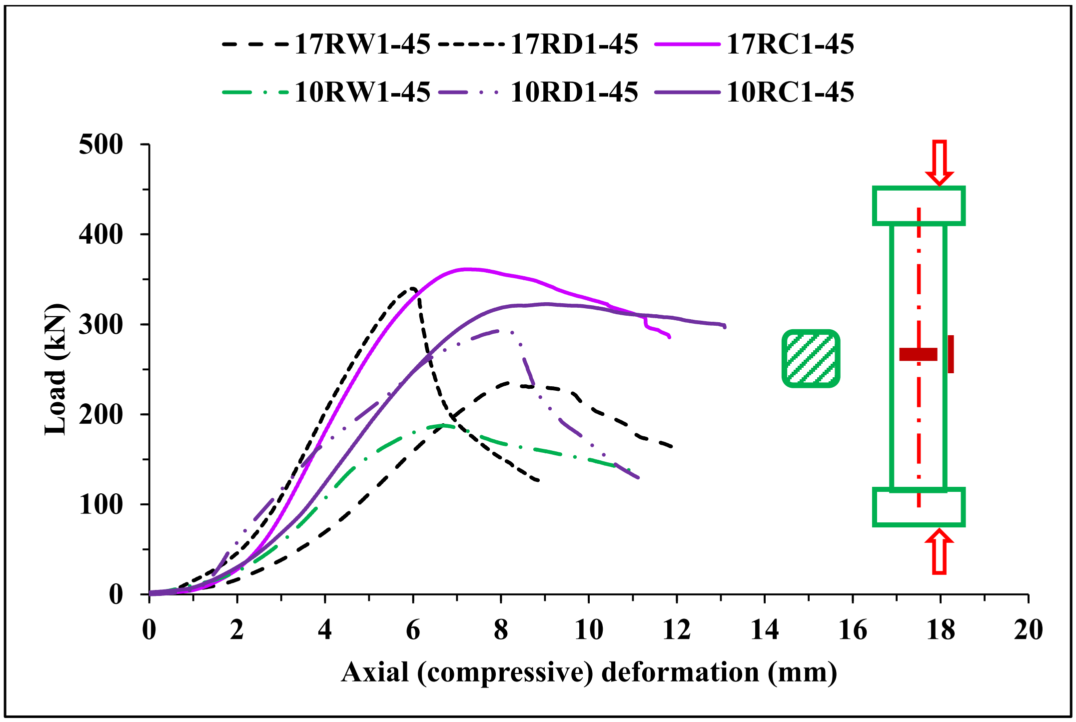

Fig. 4.12: Load-deformation interaction showing the effect of CFRP confinement in the 150 mm x 150 mm eccentrically loaded columns.

4.6.4.3 Eccentrically Loaded 150 mm x 225 mm Columns

From Fig. 4.13, for the 150 mm x 225 mm x 950 mm columns with a 90 mm eccentricity, 17RD2-90 had a peak load that was 38% greater than 17RW2-90's, while 17RC2-90 had a capacity that was 53% higher. In contrast, 10RD2-90 gained 27% more than 10RW2-90, whereas 10RC2-90 had a 72% improvement. Compared to 17RC2-90, 10RC2-90 displayed 38% higher deformation, indicating that lesser-strength concrete will exhibit more deformation. Deformation of the columns and their comparison between peak and post-peak regions (up to $\Delta_{0.85}$ after-peak) can be seen in Fig. 4.14, and Table 4.4 below.

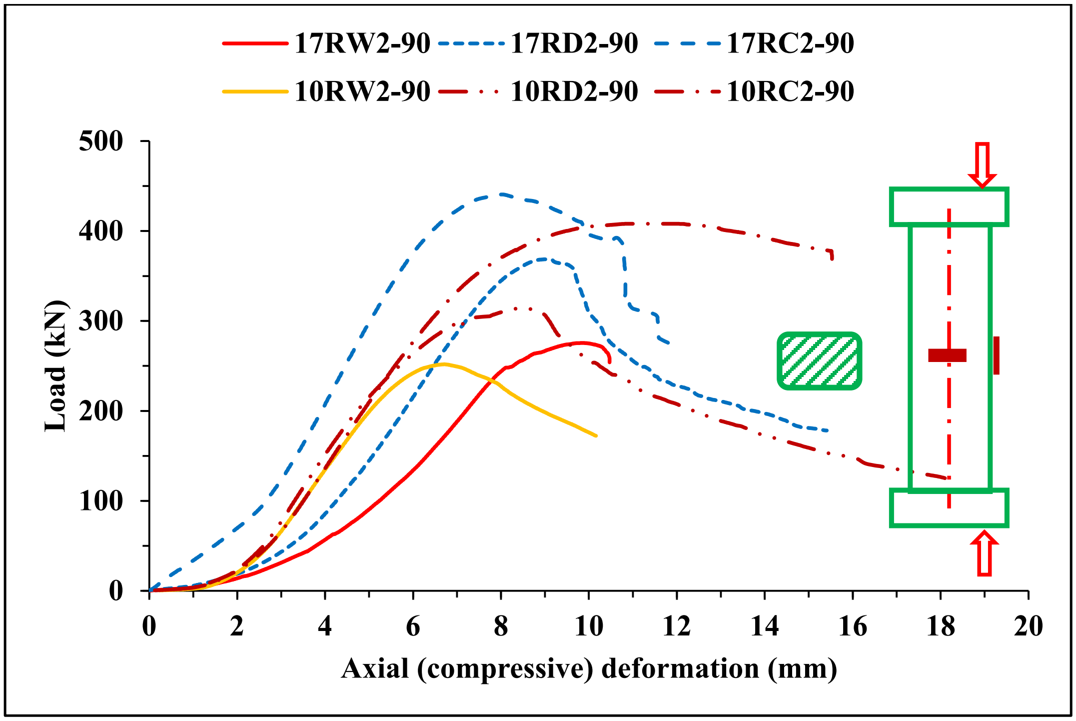

Fig. 4.13: Load-deformation interaction showing the effect of CFRP confinement in the 150 mm x 225 mm eccentrically loaded columns.

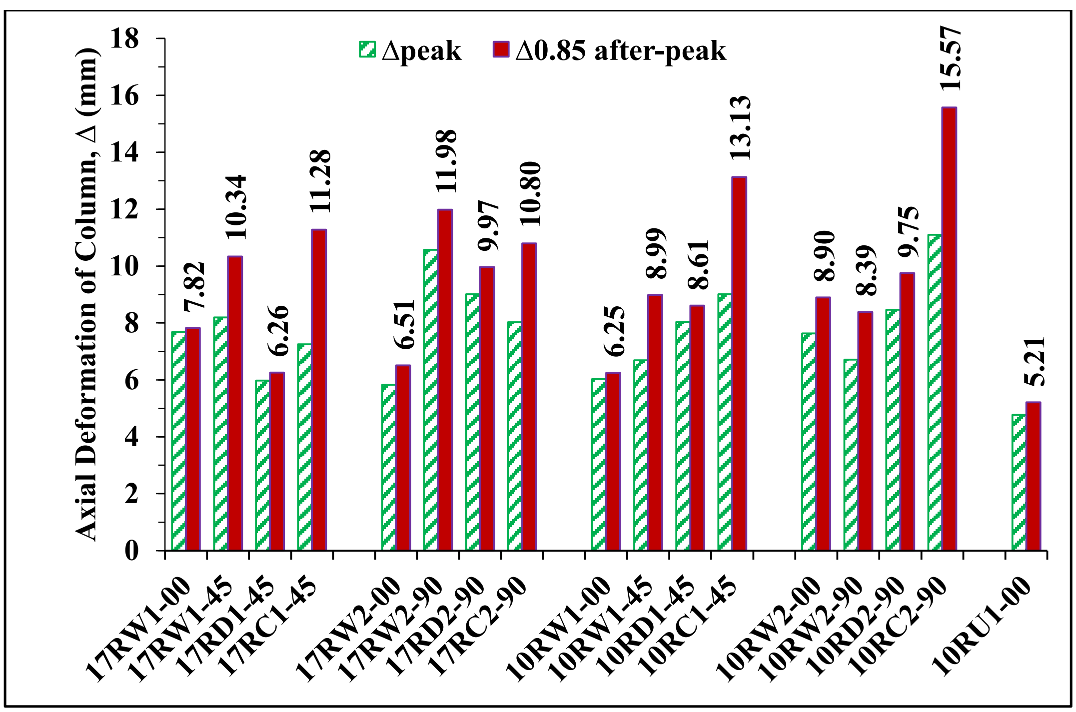

Fig. 4.14: Comparison of column deformation at peak and 85% of post- peak load.

Table 4.4: Summary of the column test results

S/N	Designation of Column	Ppeak (kN)	$P_{0.85}$ after-peak (kN)	Δpeak (mm)	$\Delta_{0.85}$ after-peak (mm)	Number of cracks	Failure Pattern	Ductility = $\Delta_{0.85}$ after-peak/Δpeak (%)
1	17RW1-00	750	638	7.68	7.82	12	Crushing	1.82
2	17RW1-45	249	212	8.20	10.34	10	Crushing & Spalling	26.10
3	17RD1-45	340	289	5.98	6.26	8	Crushing & Spalling	4.68
4	17RC1-45	372	316	7.25	11.28	6	CFRP Rupture	55.59
5	17RW2-00	1005	854	5.83	6.51	14	Crushing	11.66
6	17RW2-90	291	247	10.57	11.98	12	Crushing & Spalling	13.36
7	17RD2-90	403	343	9.01	9.97	8	Crushing & Spalling	10.65
8	17RC2-90	444	377	8.03	10.80	4	CFRP Rupture	34.50
9	10RW1-00	568	483	6.03	6.25	12	Crushing	3.65
10	10RW1-45	194	165	6.69	8.99	10	Crushing & Spalling	34.38
11	10RD1-45	299	254	8.04	8.61	8	Crushing & Spalling	7.06
12	10RC1-45	327	278	9.01	13.13	6	CFRP Rupture	45.73
13	10RW2-00	801	681	7.63	8.90	14	Crushing	16.64
14	10RW2-90	256	218	6.71	8.39	12	Crushing & Spalling	25.04
15	10RD2-90	325	276	8.47	9.75	6	Crushing & Spalling	15.11
16	10RC2-90	440	374	11.10	15.57	4	CFRP Rupture	40.27
17	10RU1-00	471	400	4.77	5.21	10	Crushing	9.22

Notes: Ppeak = Peak axial force, $P_{0.85}$ afer-peak = 85% of the peak load on the descending branch, Δpeak = Deformation corresponding to peak axial force, $\Delta_{0.85}$ after-peak = Deformation corresponding to 85% of the peak load on the descending branch.

4.6.5 Failure Modes

Studying and analyzing the failure modes of concrete columns can helps to refine their design approaches, selection of appropriate materials, identify the root cause of the failure and incorporate reinforcement strategies to enhance the structural performance. It allows them to ensure the columns can withstand the anticipated loads and provide a safe and durable structure. Additionally, failure modes aids in conducting structural assessments, evaluating existing structures, and implementing appropriate maintenance and repair strategies. The loading type, column size, and extent of CFRP confinement governed the failure modes. The failure patterns of the 17 columns are illustrated in Fig. 4.15 through Fig. 4.19. In these figures front and right faces of each column are shown, but back and left face can be seen in Appendix-C. Summary of the failure pattern are presented in Table 4.5.

4.6.5.1 Square Columns (150 mm x 150 mm) With 17 MPa Concrete

Under concentric loading of specimen 17RW1-00, vertical cracks were initiated at the column top and bottom, which were then observed to propagate vertically by increasing the crack width toward the mid-height (Fig. 4.15a). The column finally failed with the concrete crushing and spalling off the clear cover because of re-bar buckling (Fig. 4.15e).

Fig. 4.15b – Fig. 4.15d illustrates the post-failure characteristics of the eccentrically tested columns 17RW1-45, 17RD1-45, and 17RC1-45. These columns underwent testing at an eccentricity of 30%, or e = 45 mm. The first discernible horizontal cracks in 17RW1-45 formed at the tension face's upper third height before spreading along the same plane to both the front and back faces. Concrete at the compression face of the same plane showed crushing and spalling off the clear cover due to re-bar buckling, in that order (Fig. 4.15b).

As depicted in Fig. 4.15c and Fig. 4.15e; however, significant reinforcement buckling was seen for 17RD1-45, with significant cracks developing at the tension face of the upper 40% of the column's height at the unconfined region. The CFRP wraps were unaffected, and the entire height was shown to be vertically deformed.

For 17RC1-45, a CFRP tearing explosion was audible at a load near the peak load, but no physical symptoms of failure had been noticed. The column's mid-height section showed a minor bulging, and the CFRP ruptured on the compression face of the column (Fig. 4.15d). Furthermore, it was possible to identify a prominent horizontal fracture on the tension face of the concrete. The radius of the vertical curve was recognizable; however, the concrete core inside was not severely damaged.

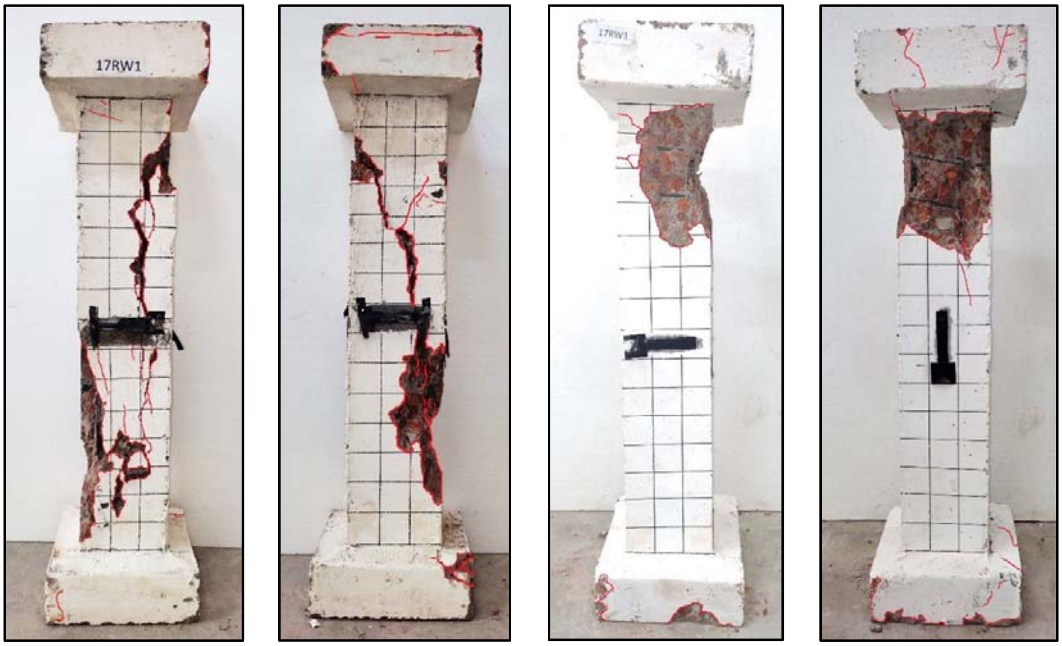

Front Right Front Right

(a) 17RW1-00 (b) 17RW1-45

Front Right Front Right

(c) 17RD1-45 (d) 17RC1-45

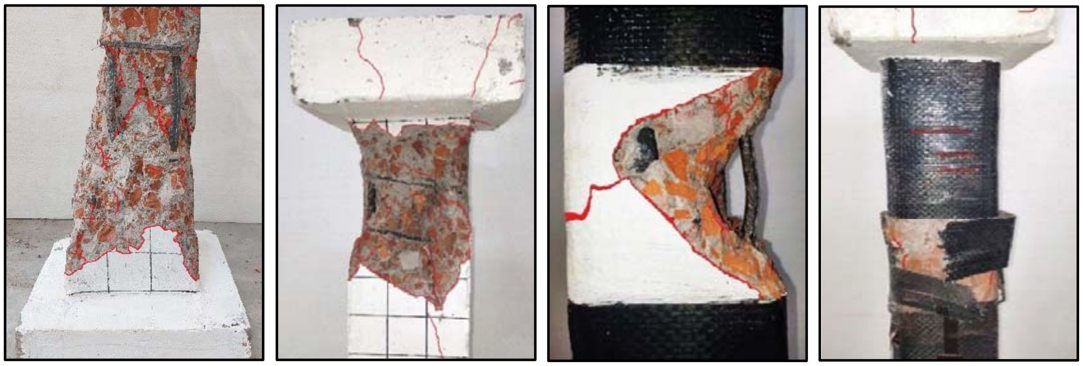

17RW1-00 17RW1-45 17RD1-45 17RC1-45

(e) Close observation of the failure modes

Fig. 4.15: Failure modes of the concentrically and eccentrically loaded of 150 mm x150 mm x 950 mm columns with 17 MPa strength.

4.6.5.2 Rectangular Columns (150 mm x 225 mm) With 17 MPa Concrete

Vertical cracks appeared to propagate vertically toward the mid-height of specimen 17RW2-00 under concentric loading after being started at the top of the body (Fig. 4.16a). The shearing caused the column to finally break by widening the crack at mid-height.

The post-failure characteristics of the eccentrically tested columns 17RW2-90, 17RD2-90, and 17RC2-90 are shown in Fig. 4.16b through Fig. 4.16d. These columns were tested at an eccentricity of 40% of the largest lateral dimension, i.e., e = 90 mm. The tension face's upper third height is where the first observable horizontal cracks in 17RW2-90 appeared before moving along the same plane to the back faces. Through crushing and spalling off the clear cover, concrete at the compression face displayed an angled fracture (Fig. 4.16b). However, the vertical curve radius was not as noticeable as in 17RW-45, but the reinforcing did seem to give once the column was manually crushed.

However, reinforcement buckling was seen for 17RD2-90, with sizeable fractures appearing at the tension face of the top 40% of the column's height in the unconfined area, as shown in Fig. 4.16c. When the maximal load was reached, the concrete bulged visibly and suddenly began to crush. The entire height was revealed to be vertically curved, and the CFRP wraps were completely undamaged.

For 17RC2-90, a CFRP tearing explosion could be heard at a load level close to the maximum load, but no outward signs of failure had yet been observed. The CFRP burst on the compression face at the peak load, and the mid-height section of the column developed a little bulge: recognizable vertical curve radius and minimal damage to the interior concrete core (Fig. 4.16d).

Front Right Front Right

(a) 17RW2-00 (b) 17RW2-90

Front Right Front Right

(c) 17RD2-90 (d) 17RC2-90

17RW2-00 17RW2-90 17RD2-90 17RC2-90

(e) Close observation of the failure modes

Fig. 4.16: Failure modes of the concentrically and eccentrically loaded of 150 mm x 225 mm x 950 mm columns with 17 MPa strength.

4.6.5.3 Square Columns (150 mm x 150 mm) With 10 MPa Concrete

In specimen 10RW1-00, vertical fractures were initiated at the body's top when subjected to concentric loading, extending vertically toward the mid-height (Fig. 4.17a). The column eventually broke due to concrete disintegration and the clear cover peeling off.

Fig. 4.17b through Fig. 4.17d display the post-failure attributes of the eccentrically tested columns 10RW1-45, 10RD1-45, and 10RC1-45. The columns were subjected to an eccentricity of 30%, or e = 45 mm. The first discernible horizontal cracks in 10RW1-45 began forming at the upper third height of the tension face before moving along the same plane to both the front and rear faces. As shown in Fig. 4.17b, the concrete at the compression face of the same plane underwent crushing and peeling off the clear cover due to re-bar buckling.

Substantial reinforcement buckling was noticeable in 10RD1-45 (Fig. 4.17c), with prominent cracks developing at the tension face in the upper 40% column height in the unconfined region. The CFRP wraps were unaffected, and a vertical curvature was observed across the entire height.

In the case of 10RC1-45, a loud sound of CFRP tearing was heard near the peak load. At the column's mid-height, the CFRP broke at the compression face at the peak load (Fig. 4.17d). A prominent horizontal fracture could be identified on the tension face of the concrete. The vertical curve radius was distinguishable, and the internal concrete core was minimally damaged.

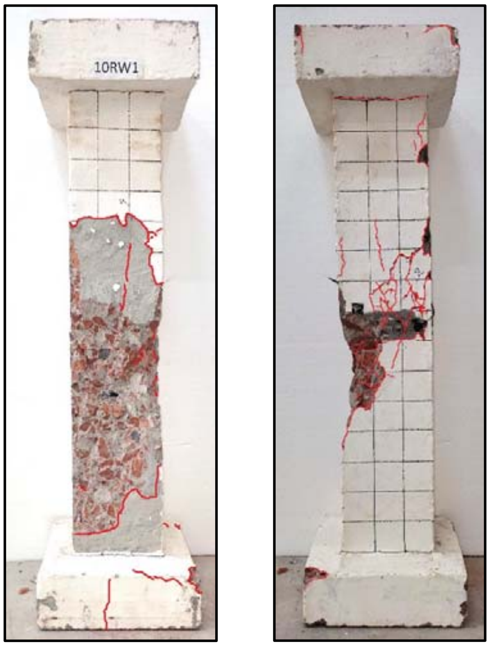

Front Right

(a) 10RW1-00

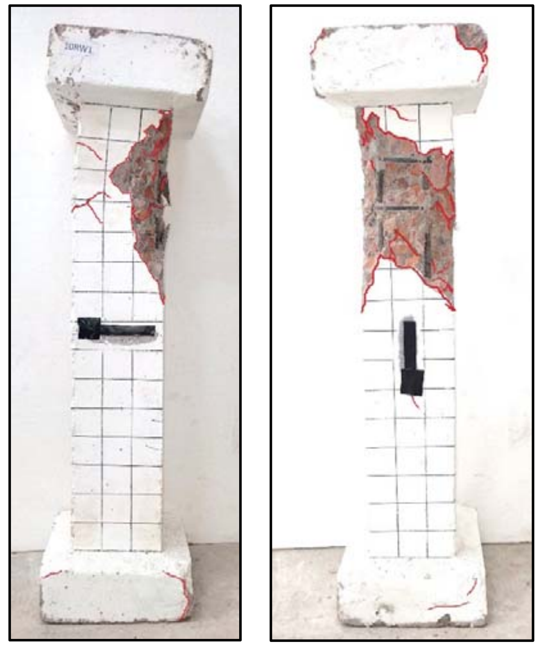

Front Right

(b) 10RW1-45

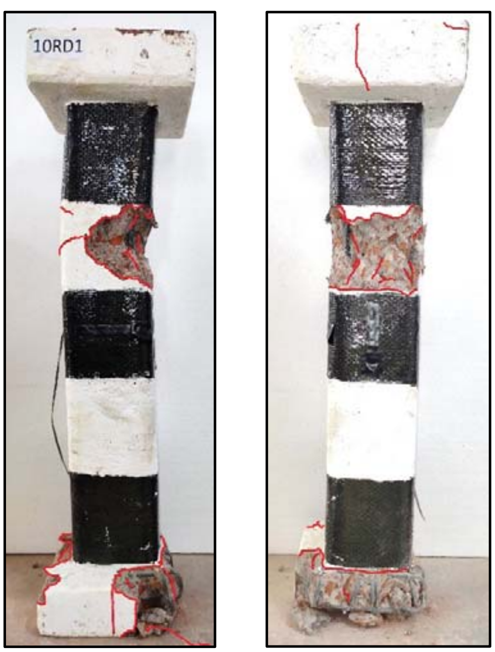

Front Right

(c) 10RD1-45

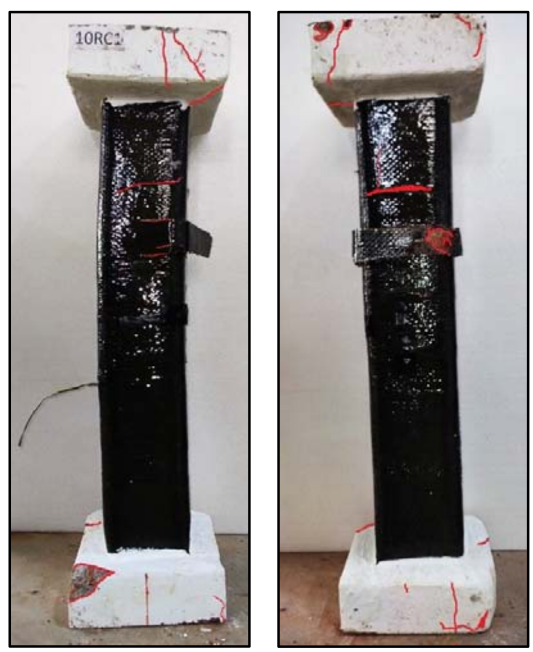

Front Right

(d) 10RC1-45

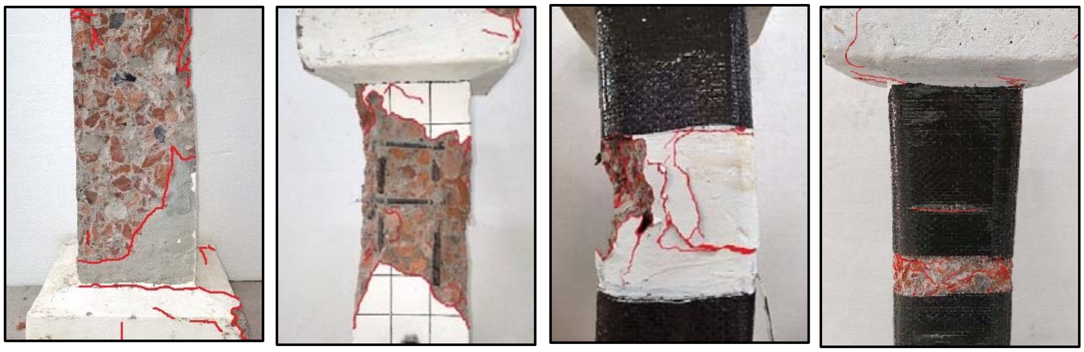

10RW1-00 10RW1-45 10RD1-45 10RC1-45

(e) Close observation of the failure modes

Fig. 4.17: Failure modes of the concentrically and eccentrically loaded of 150 mm x150 mm x 950 mm columns with 10 MPa strength.

4.6.5.4 Rectangular Columns (150 mm x 225 mm) With 10 MPa Concrete

Vertical cracks began at the top of the body and extended vertically towards the mid-height of specimen 17RW2-00 when under concentric loading. The column eventually broke at the upper third height due to shearing, and the re-bar also buckled (Fig. 4.18a).

The mid-height of the tension face is where the first visible horizontal cracks in 10RW2-90 appeared before moving along the same plane to the front and back faces. The concrete at the compression face of the same plane displayed crushing and peeling off of the clear cover, and the re-bars were buckled in that order (Fig. 4.18b).

Significant reinforcement buckling was observed in 10RD2-90, with notable cracks developing at the tension face of the upper 40% of the column's height in the unconfined region. The CFRP wraps remained unaffected, and the entire height displayed a vertical curve (Fig. 4.18c).

In the case of 10RC2-90, a loud sound of CFRP tearing was heard near the peak load. At the column's mid-height, the CFRP broke on the compression face at the peak load. A notable horizontal fracture could be identified on the tension face of the concrete (Fig. 4.18d). The vertical curve radius was distinguishable, and the internal concrete core was minimally damaged.

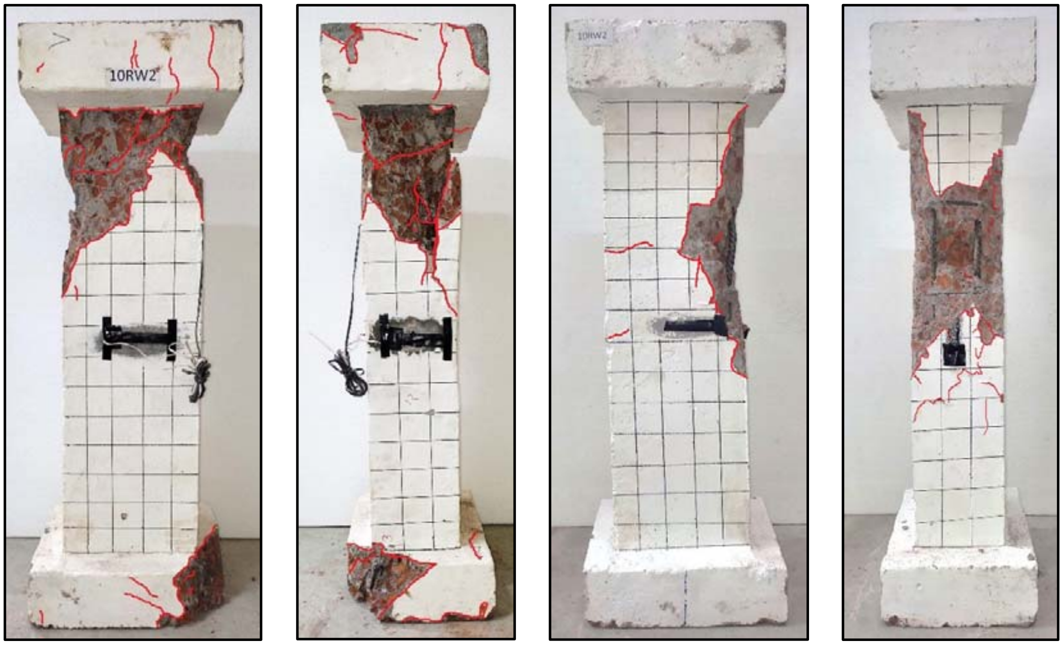

Front Right Front Right

(a) 10RW2-00 (b) 10RW2-90

Front Right Front Right

(c) 10RD2-90 (d) 10RC2-90

10RW2-00 10RW2-90 10RD2-90 10RC2-90

(e) Close observation of the failure modes

Fig. 4.18: Failure modes of the concentrically and eccentrically loaded of 150 mm x 225 mm x 950 mm columns with 10 MPa strength.

4.6.5.5 Column without tie bars

Column 10RU1-00, which lacked tie bars, was tested under concentric loading. The initial cracks appeared around the column's hunch, beneath the top head, and quickly extended towards the mid-height (Fig. 4.19). The spalling of the concrete cover around the top one-third region characterized the column failure. However, a major spall-off of the concrete cover was observed on one side of the column.

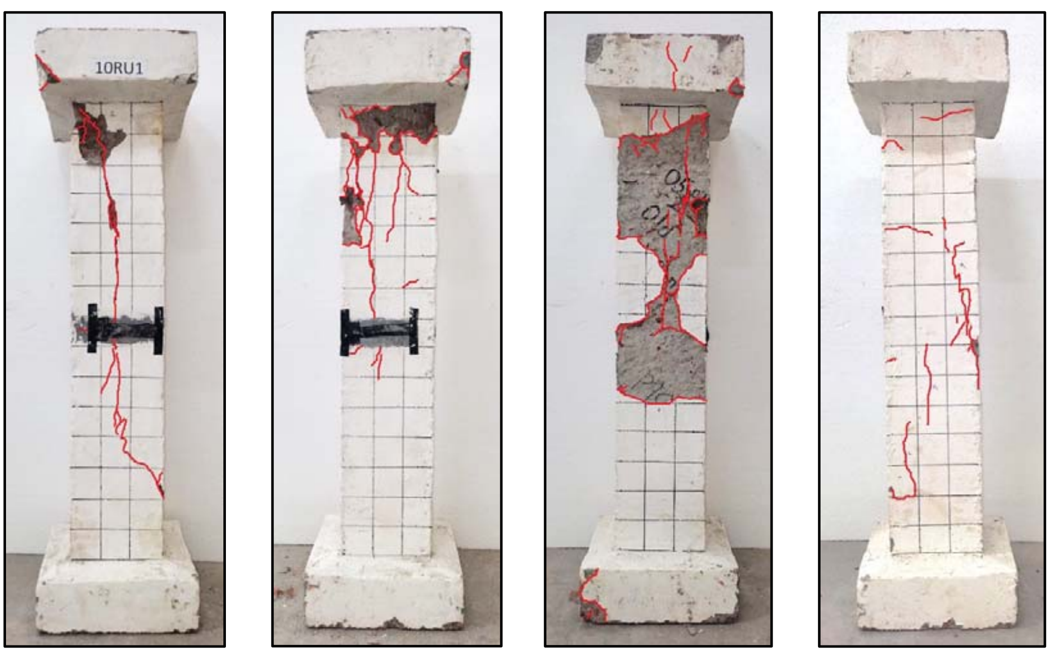

Front Right Back Left

Fig. 4.19: Failure modes of the concentrically loaded 10RU1-00 column.

Table 4.5: Summary of the column failure pattern

Cross section of column	Concrete Strength	Concentric column w/o CFRP	Eccentric Column			
			Eccentricity	W/O CFRP	Discrete CFRP	Continuous CFRP
150 x 150	17 MPa	• 12 Cracks developed • Re-bar buckled • Concrete crushing	45 mm	• 10 Cracks developed • Re-bar buckled • Crushing & Spalling	• 8 Cracks developed • Re-bar buckled • Crushing & Spalling • CFRP Unaffected	• 6 Cracks developed • CFRP Ruptured • Concrete core not severely damaged • Column buckled
150 x 225	17 MPa	• 14 Cracks developed • Concrete crushing	90 mm	• 12 Cracks developed • Re-bar buckled • Crushing & Spalling	• 8 Cracks developed • Re-bar buckled • Crushing & Spalling • CFRP Unaffected	• 4 Cracks developed • CFRP Ruptured • Concrete not critically damaged • Column buckled
150 x 150	10 MPa	• 12 Cracks developed • Concrete crushing	45 mm	• 10 Cracks developed • Re-bar buckled • Crushing & Spalling	• 8 Cracks developed • Re-bar buckled • Crushing & Spalling • CFRP Unaffected • Column buckled	• 6 Cracks developed • CFRP Ruptured • Concrete core not fatally damaged • Column buckled
150 x 225	10 MPa	• 14 Cracks developed • Re-bar buckled • Concrete crushing	90 mm	• 12 Cracks developed • Re-bar buckled • Crushing & Spalling	• 6 Cracks developed • Re-bar buckled • Crushing & Spalling • CFRP Unaffected • Column buckled	• 4 Cracks developed • CFRP Ruptured • Concrete core not seriously damaged • Column buckled
150 x 150 w/o ties	10 MPa	• 10 Cracks developed	-	-	-	-

4.6.6 Dilation Effect

4.6.6.1 Increase in Column Area

Fig. 4.20 and Appendix-D illustrates the locations of the linear variable differential transformer (LVDT) and the corresponding midpoint lateral deformation of the columns on the four faces at the peak load. In general, the failure of the concentrically loaded columns was governed by concrete crushing, the failure face being subjected to compression. Unlike the concentrically loaded columns, a significant increment of lateral deformation was noticed in the eccentrically loaded columns.

A lower modulus of elasticity leads to increased dilation properties of the concrete. This enhanced dilation activates the passive confinement effect of the Fiber-Reinforced Polymer (FRP), only achieving improved concrete strength after the concrete has expanded and dilated. From Fig. 4.20, columns with a strength of 17 MPa consistently demonstrate a tendency towards lower lateral deformation than their 10 MPa counterparts when subjected to identical conditions. Additionally, the loading type applied on the columns also plays a critical role, with eccentric loading generally inducing more lateral deformation than concentric loading.

The presence of Carbon Fiber Reinforced Polymer (CFRP) wrapping also influences deformation characteristics, potentially helping to minimize lateral deformation in certain instances due to greater stiffness gain from CFRP confinement and enhanced compressive strength of confined concrete, such as evidenced by comparing 17RD1-45 with 17RW1-45 or 10RD1-45 with 10RW1-45. While the influence of CFRP wrapping on deformation reduction is evident in certain instances, the experimental cross-sectional area increased values offer an opportunity for further investigation to fully unveil the underlying pattern correlating CFRP wrapping with reduced lateral deformation. An increased aspect ratio, from 1 to 1.5, within the same column type can reduce lateral deformation, demonstrated by comparing 17RW1-00 with 17RW2-00 or 10RW1-00 with 10RW2-00 on account of increased stiffness.

Fig. 4.21 compares the increased area for all the columns expressed as percentages. It reveals that most columns experienced minor area increments, except for 10RW1-00 and 10RC1-45, which underwent the most significant increase in the area among all the specimens.

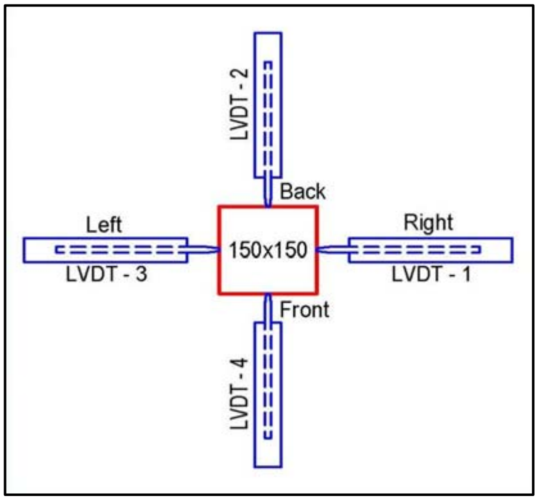

(a) Location of LVDT

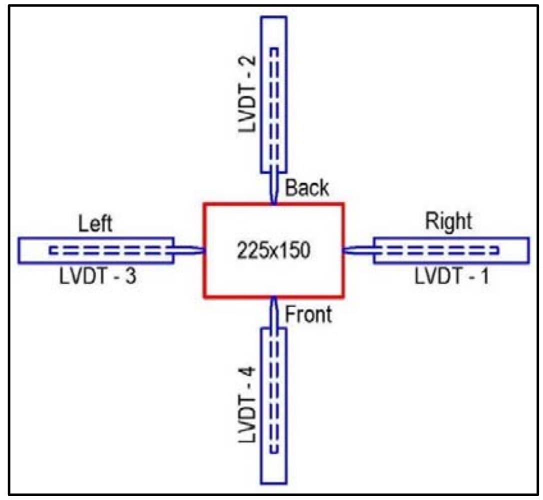

(b) Location of LVDT

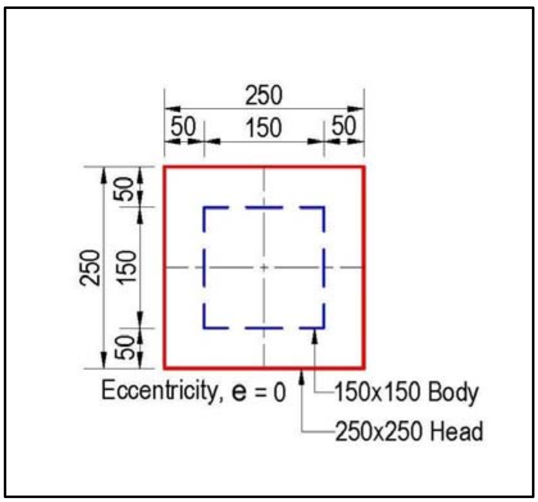

(c) Line of action of applied load

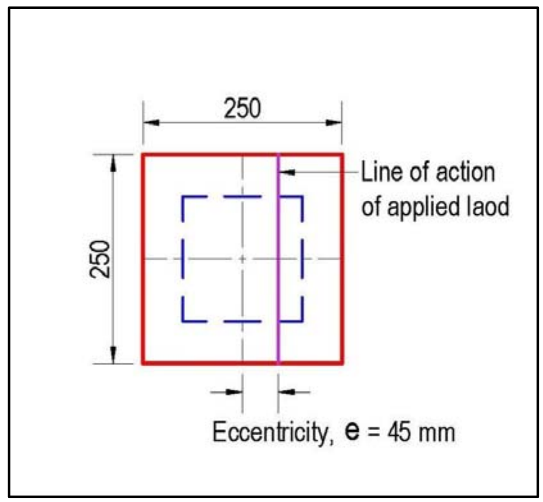

(d) Line of action of applied load

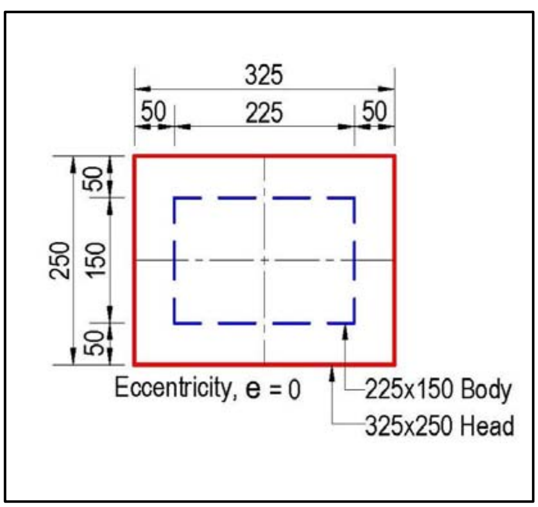

(e) Line of action of applied load

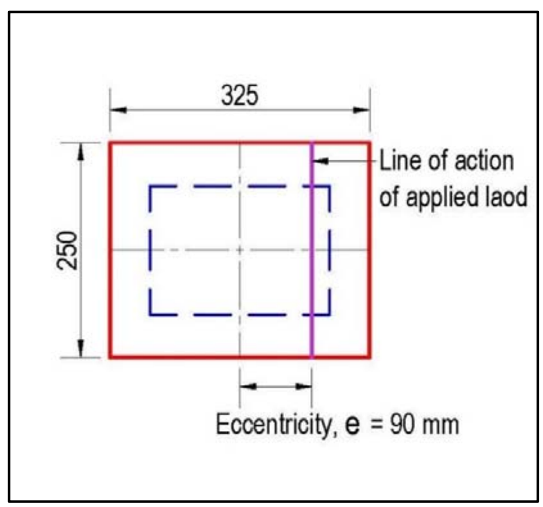

(f) Line of action of applied load

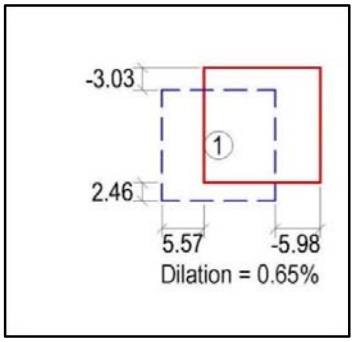

(g) 17RW1-00

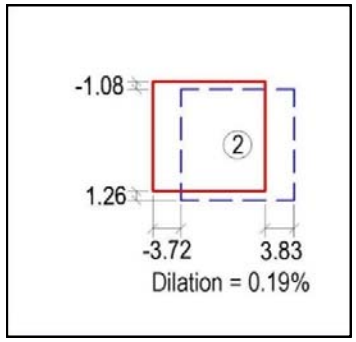

(h) 17RW1-45

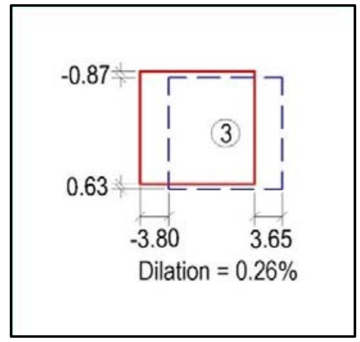

(i) 17RD1-45

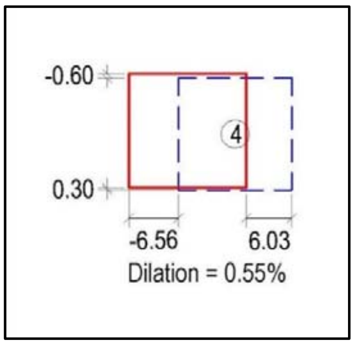

(j) 17RC1-45

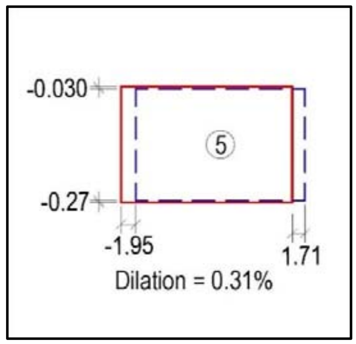

(k) 17RW2-00

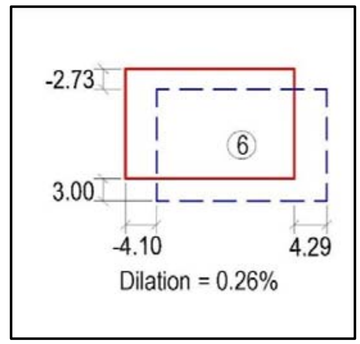

(l) 17RW2-90

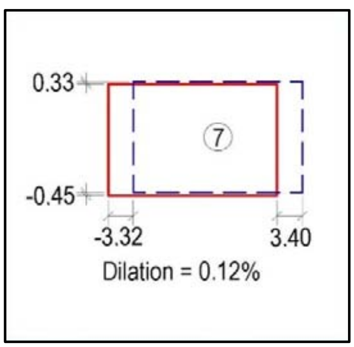

(m)17RD2-90

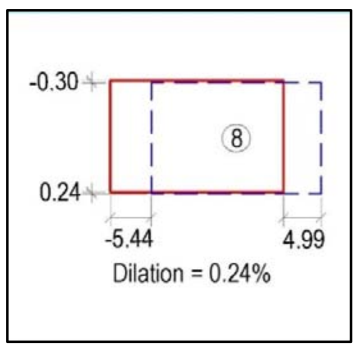

(n) 17RC2-90

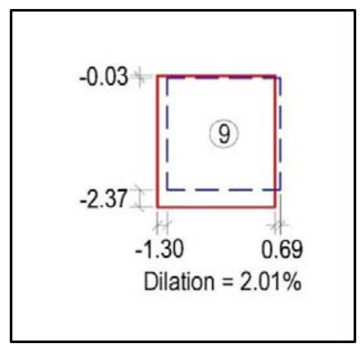

(o) 10RW1-00

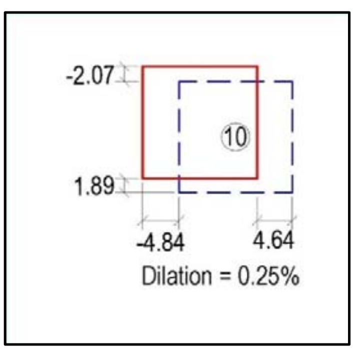

(p) 10RW1-45

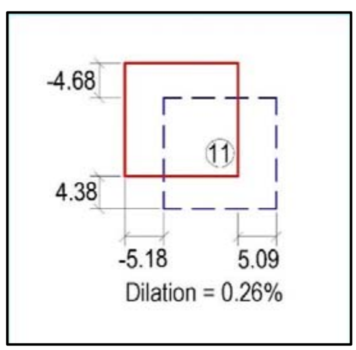

(q) 10RD1-45

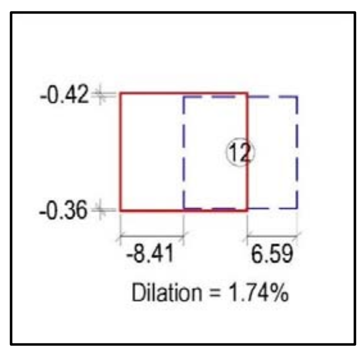

(r) 10RC1-45

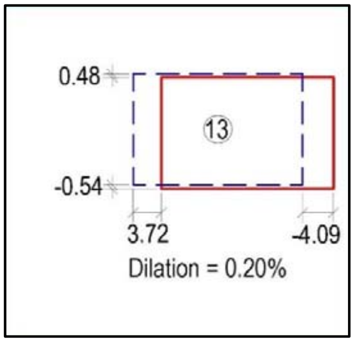

(s) 10RW2-00

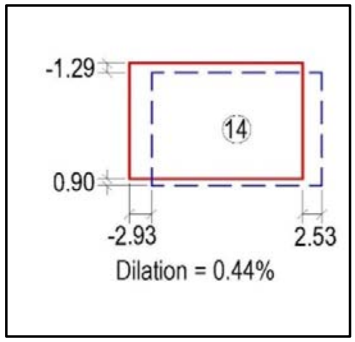

(t) 10RW2-90

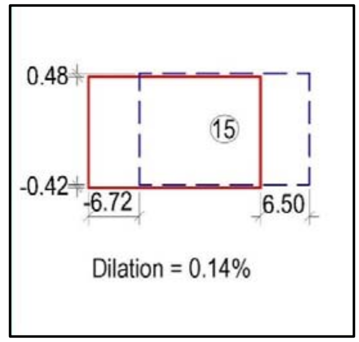

(u) 10RD2-90

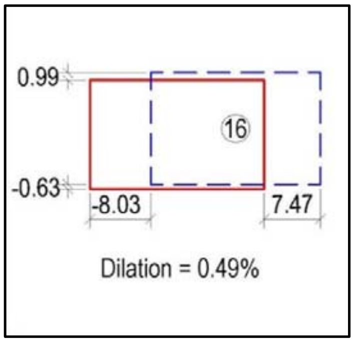

(v) 10RC2-90

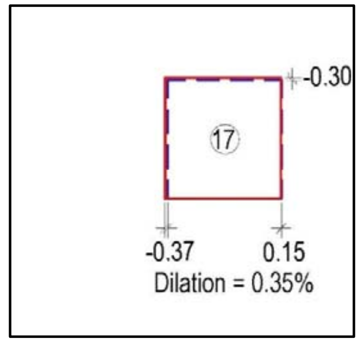

(w) 10RU1-00

Note: The blue box represents the initial position of the columns, and the red box represents the corresponding mid-point lateral deformation of the columns at the peak load.

Fig. 4.20: Comparison of the initial and deformed area of the column at peak load.

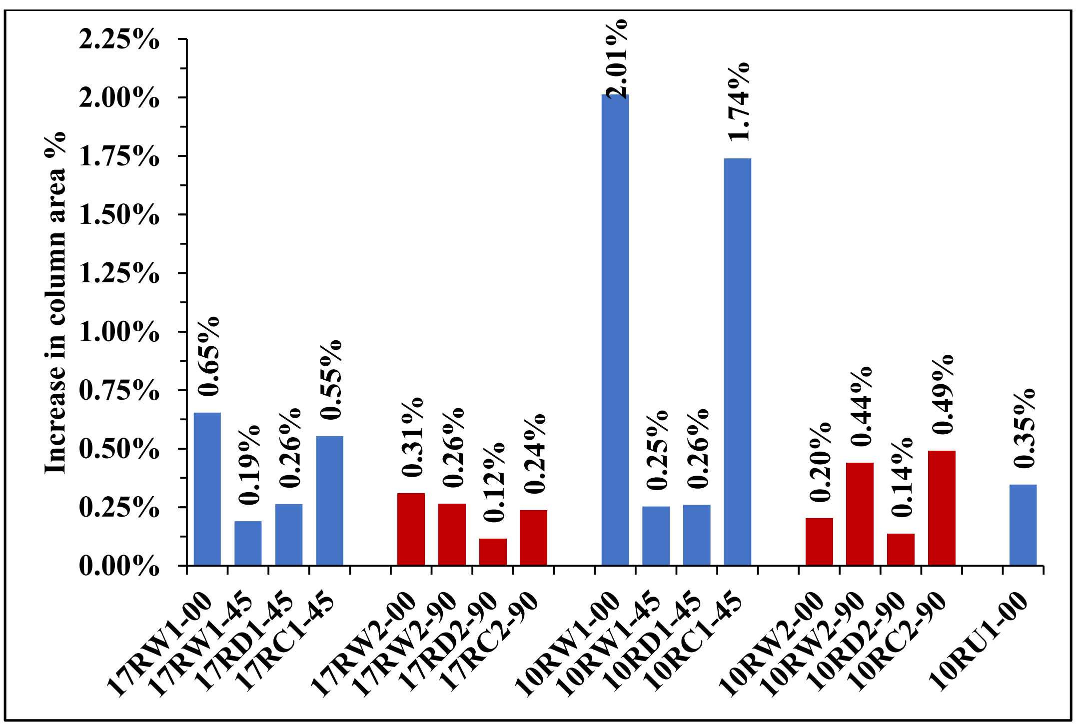

Fig. 4.21: Increment of column area at peak load.

4.6.6.2 Axial Strain in Reinforcement

The axial strain graphs of the reinforcing bars indicate that the longitudinal bars were under compression for the concentrically loaded columns across all instances, regardless of aspect ratio (Fig. 4.22). The reinforcement in eccentrically loaded columns was under tension (Fig. 4.23). The reinforcement in the eccentrically loaded columns was subjected to much larger strains than those in the concentrically loaded columns due to the bending of the columns under eccentric load. However, under concentric loading, steel strain exceeds the yield strain of steel, ε = 0.002 ($\varepsilon = \frac{\sigma}{E}$), suggesting that the yielding of the bars occurs. For instance, in the case of a column strength of 17 MPa with an aspect ratio of 1 (17RW1-00), the steel strain value is -0.0047, indicating contraction. This pattern repeats in all the other cases of concentric loading, such as 17RW2-00 (strain -0.0034), 10RW1-00 (strain -0.0057), and 10RW2-00 (strain -0.0059).

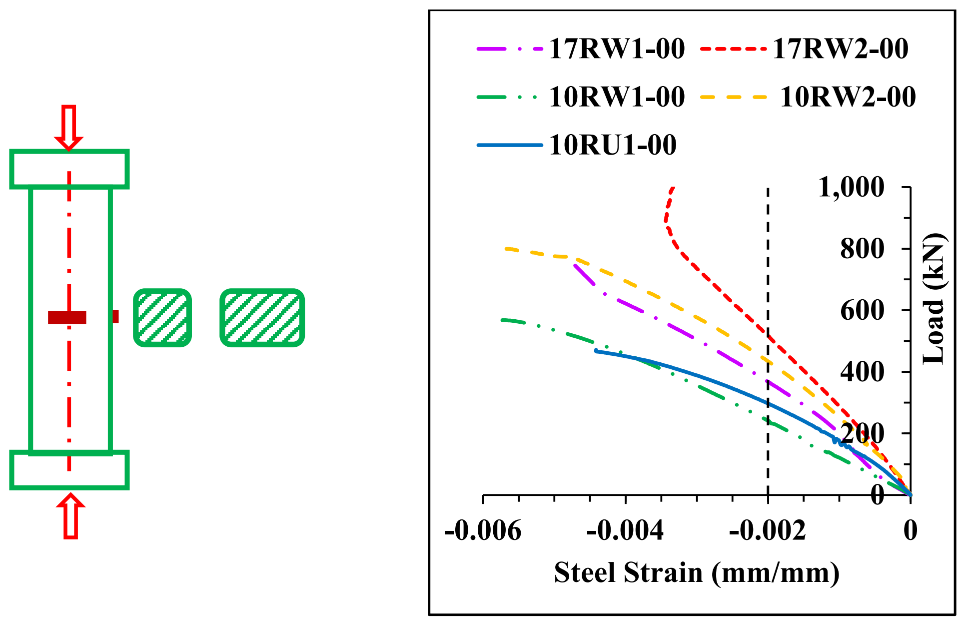

Fig. 4.22: Load-axial strain interaction of steel in the concentrically loaded columns.

For eccentric loading, the amount of strain varies depending on the application of CFRP wrapping and the column's aspect ratio. Continuous CFRP wrapping generally results in higher steel strain values, due to the larger deformation in the columns under eccentric loading. For column with a strength of 17 MPa and an aspect ratio of 1 (17RC1-45), the steel strain is as high as 0.0092. This strain value is noticeably higher when compared to the without-wrapped column under similar conditions (17RW1-45) with a strain of 0.0016. The trend of increased strain with continuous CFRP wrapping is also observed in columns with different strengths and aspect ratios. Among all specimens, particularly the 150 mm x 225 mm rectangular column, namely 17RD2-90, abruptly shows a very lower steel strain of 0.00015. This indicates concrete has been yielded in an unconfined region before yielding of tension reinforcement. Reinforcement strain is summarized in Table 4.6.

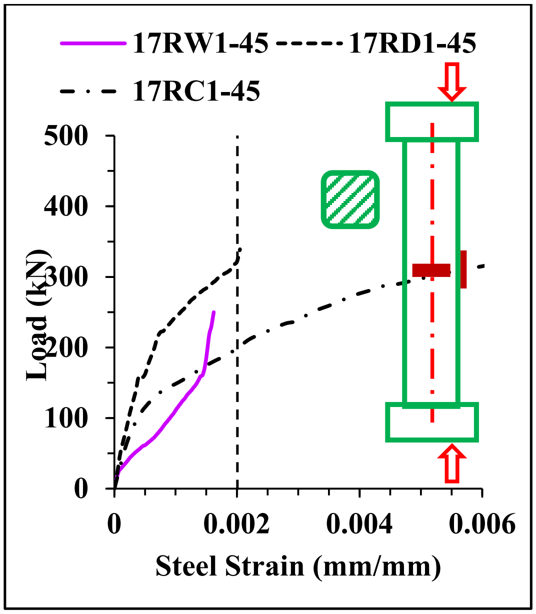

(a) 150 mm x 150 mm columns of 17 MPa strength

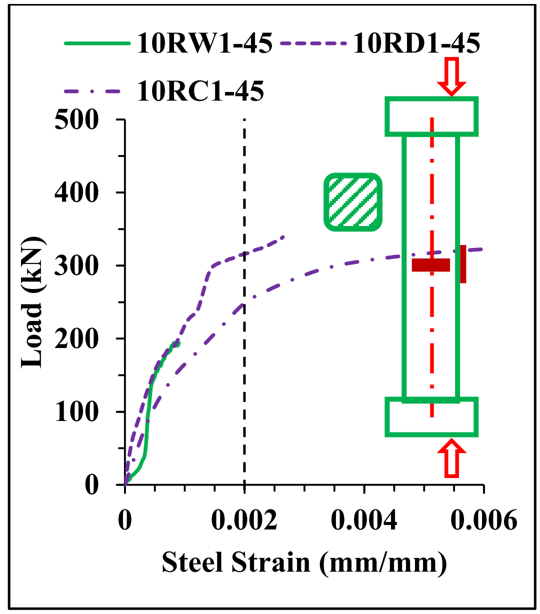

(b) 150 mm x 150 mm columns of 10 MPa strength

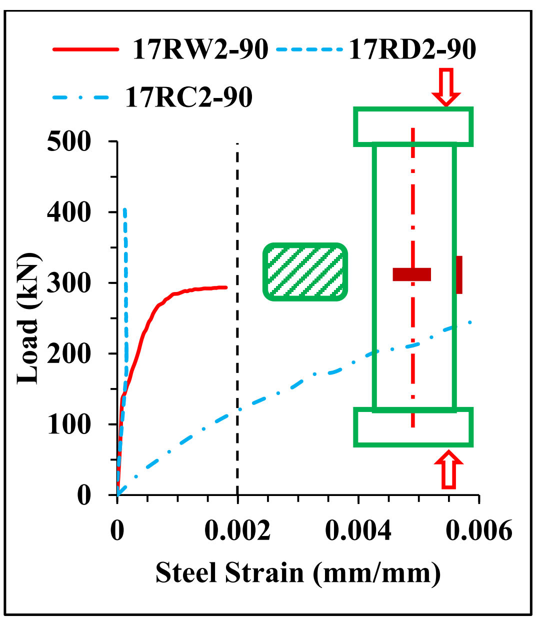

(c) 150 mm x 225 mm columns of 17 MPa strength

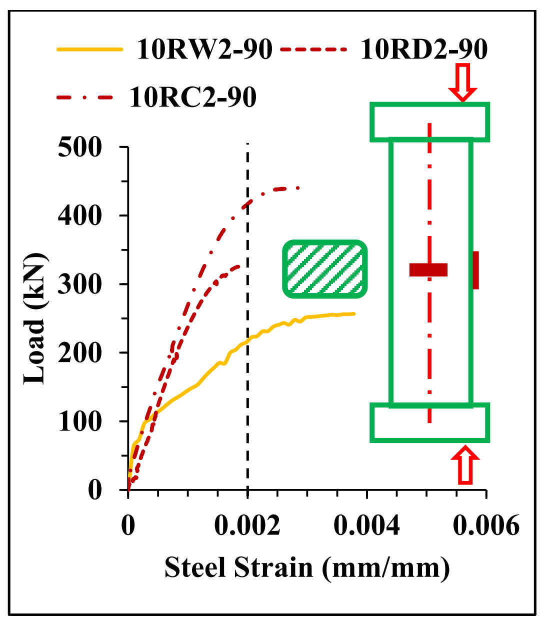

(d) 150 mm x 225 mm columns of 10 MPa strength

Fig. 4.23: Load-axial strain interaction of steel in the eccentrically loaded columns.

4.6.6.3 Axial Strain in Concrete

For most columns, the ultimate failure was caused by the crushing of concrete following the yielding of the longitudinal reinforcement. Looking at the strain values, the axial strain under concentric loading ranges between -0.0048 and -0.0078 (Fig. 4.24). A key observation is that the strain is usually more pronounced for columns with a lower strength (10 MPa) than those with a higher strength (17 MPa). Furthermore, the 10RW1-00 column shows 27% more strain than the 10RU1-00 column, where ties were not used.

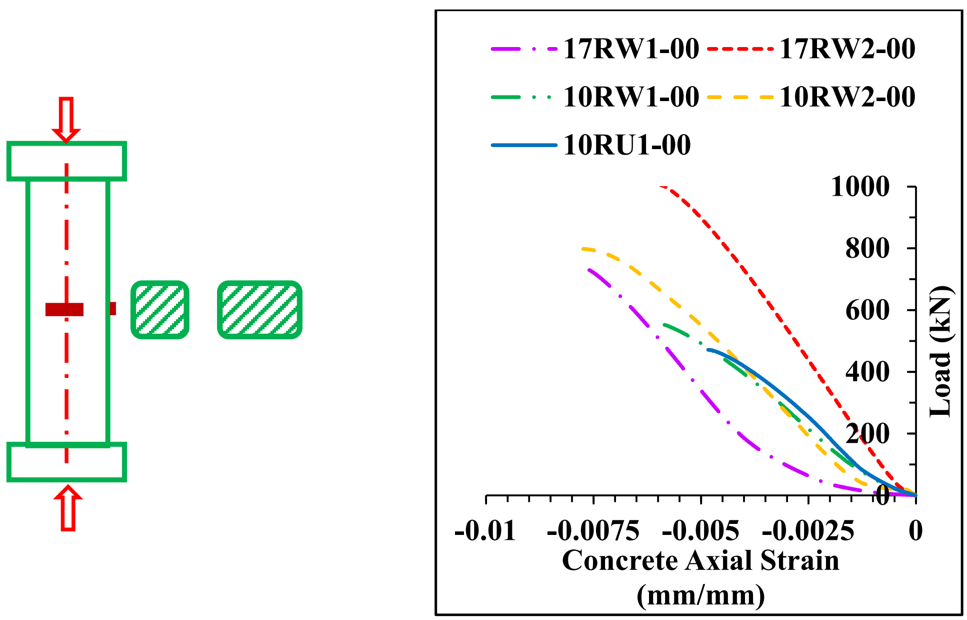

Fig. 4.24: Load-axial strain interaction of concrete in the concentric columns.

Eccentric loading, generally results in a combination of bending and axial stress, leading to higher strain values than concentric loading. In the eccentrically loaded columns, the eccentric load produced compression on the right face and tension on the left face. Accordingly, the concrete strain gauges in the longitudinal direction on the right face produced graphs on the negative side for compression. The strain values under eccentric loading range from -0.0039 to -0.0138 (Fig. 4.25). For columns with no CFRP wrapping and an aspect ratio of 1, the 17 MPa column (17RW1-45) shows less strain (-0.0039) than the 10 MPa columns (10RW1-45) with a strain of -0.0041. This pattern follows when CFRP wrapping is introduced. For instance, with discrete CFRP wrapping, the strain in the 17 MPa column (17RD1-45) is -0.0046, while it is -0.0064 in the 10 MPa columns (10RD1-45). These findings consist of the concept that lower-strength concrete is more ductile than higher-strength concrete. Moreover, the impact of CFRP wrapping becomes more pronounced with eccentric loading, which is a minimum of 2.93 times (-0.0088) of the ultimate unconfined strain of 0.003. Concrete axial strain can be seen in Table 4.6.

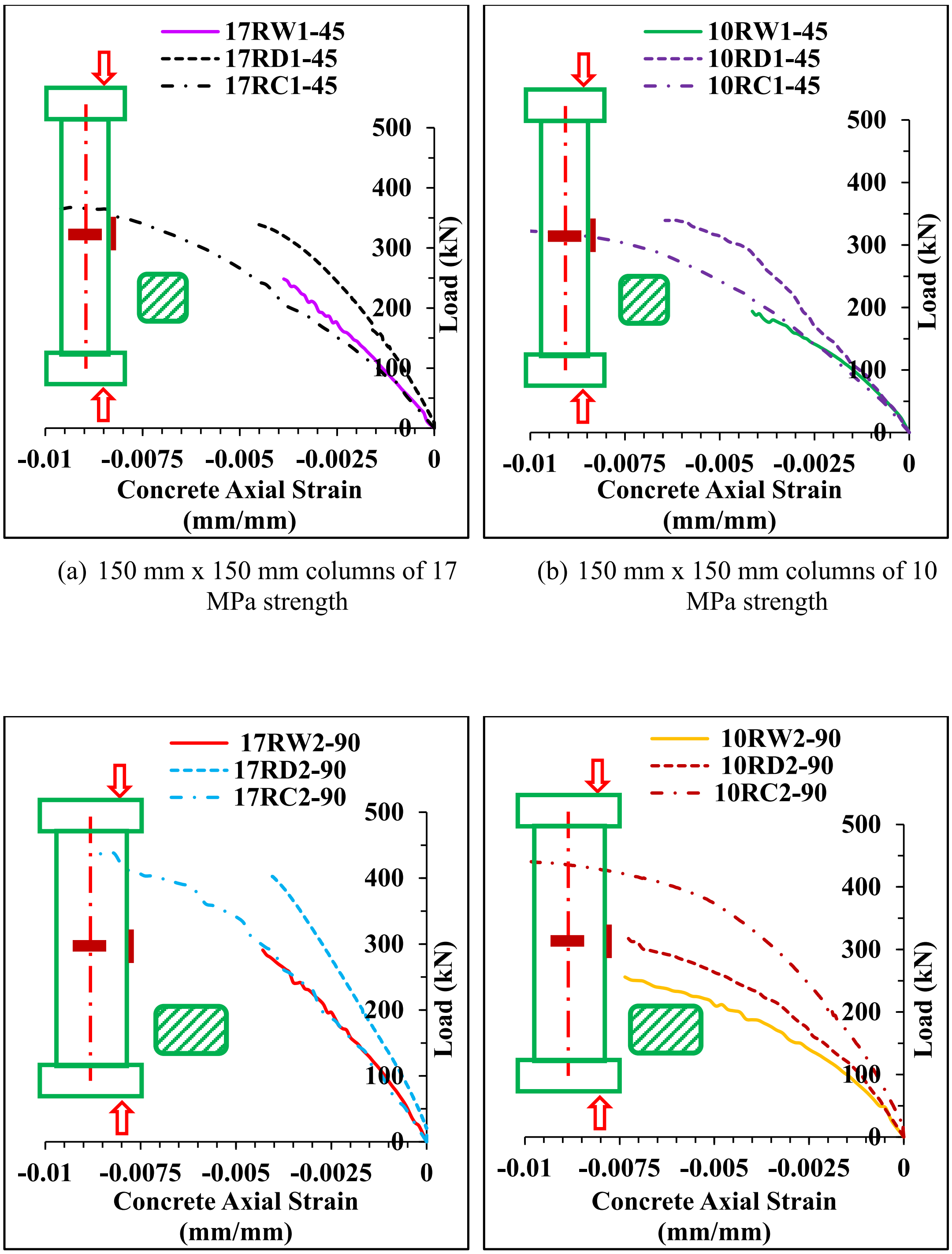

(a) 150 mm x 150 mm columns of 17 MPa strength

(b) 150 mm x 150 mm columns of 10 MPa strength

(c) 150 mm x 225 mm columns of 17 MPa strength

(d) 150 mm x 225 mm columns of 10 MPa strength

Fig. 4.25: Load-axial strain interaction of concrete in the eccentric columns.

4.6.6.4 Transverse Strain in Concrete

Columns subjected to concentric loading, where the line of action of the load aligns with the center of the column, exhibit a general consistency in transverse concrete strain on both the front and side faces. As a general trend, columns under concentric loading showed higher transverse strain than those under eccentric loading. However, an outlier is column 10RW1-45, which had higher strain under eccentric loading. The most significant transverse strain under concentric loading was observed in column 10RW1-00, registering at 0.0059. This was followed by column 10RU1-00 with a strain of 0.0024, while column 17RW2-00 showed a minor strain at 0.0011 (Fig. 4.26).

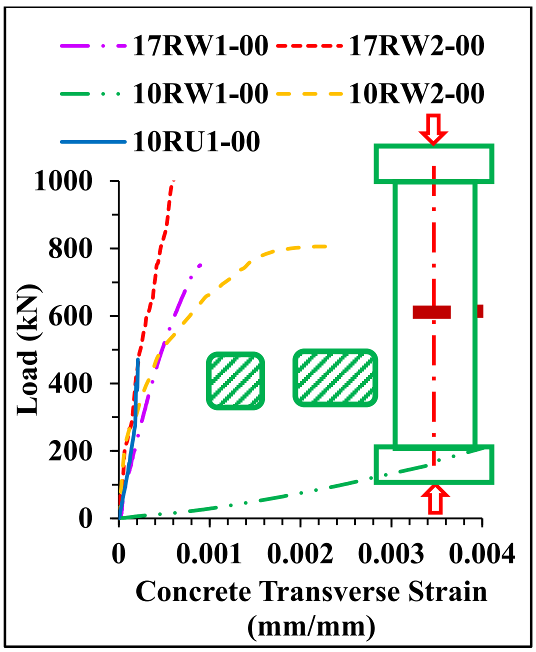

(a) Front

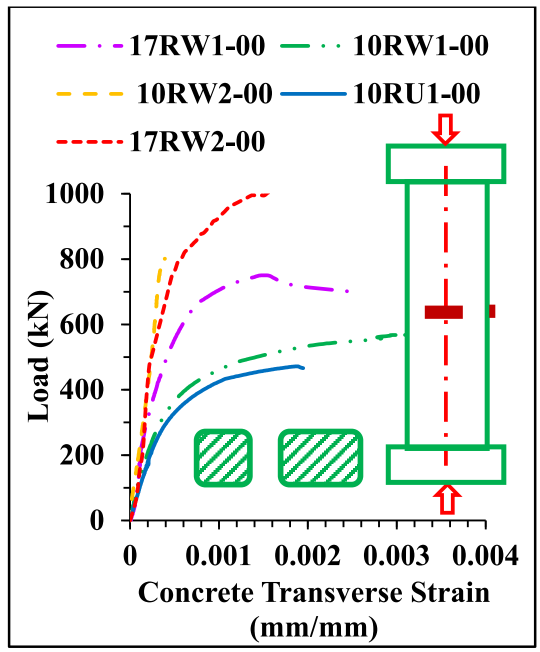

(b) Right/Left

Fig. 4.26: Load-transverse strain interaction of concrete in the concentric columns.

Regarding the columns under eccentric loading, column 10RW1-45 exhibited the highest transverse strain at 0.0076. In contrast, the lowest strain was recorded by columns 17RD2-90 and 10RC2-90, presenting a strain of 0.0001 (Fig. 4.27). A summary of the axial and transverse concrete strain and axial strain of longitudinal re-bar corresponding to peak load are presented in Table 4.6.

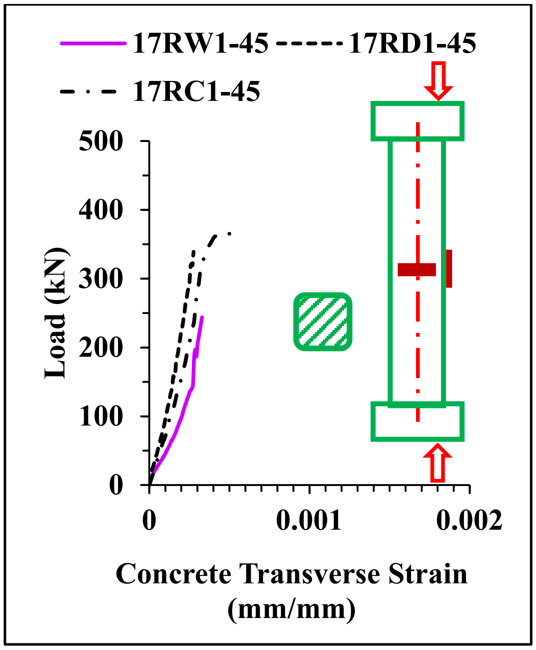

(a) 150 mm x 150 mm columns of 17 MPa strength

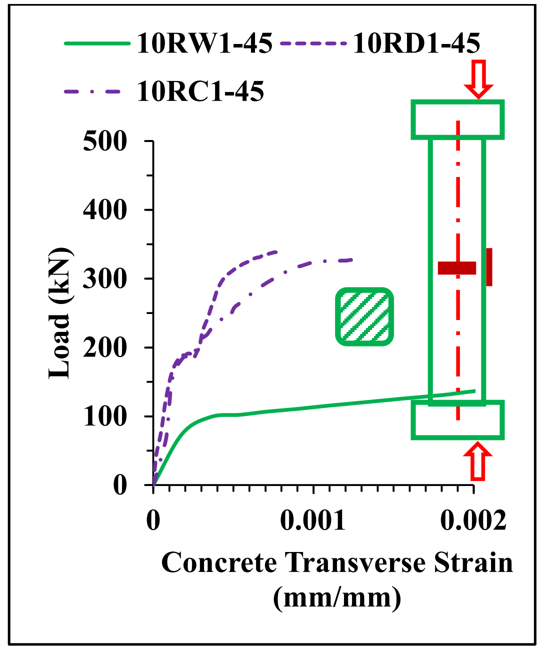

(b) 150 mm x 150 mm columns of 10 MPa strength

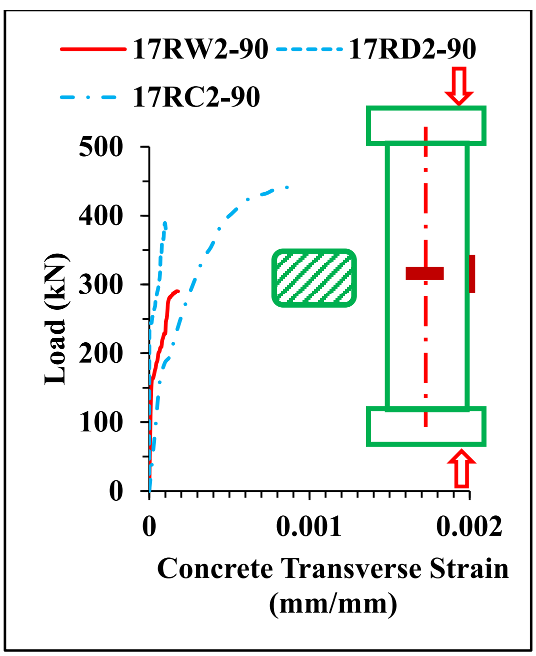

(c) 150 mm x 225 mm columns of 17 MPa strength

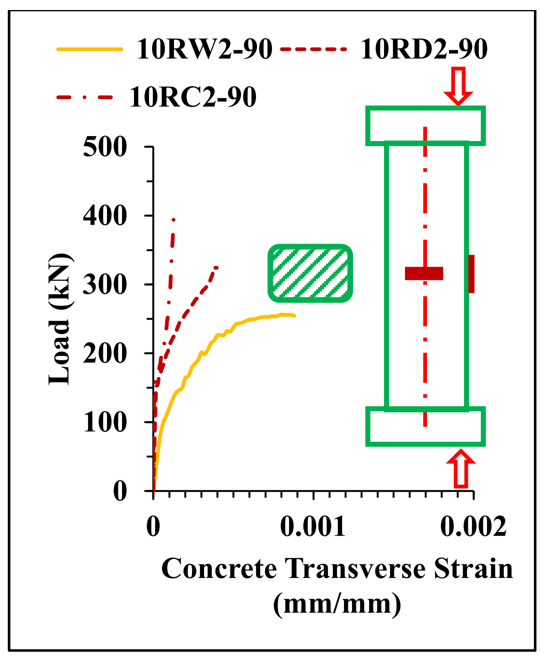

(d) 150 mm x 225 mm columns of 10 MPa strength

Fig. 4.27: Load-transverse strain interaction of concrete in the eccentric columns.

Table 4.6: Summary of the strain in reinforcement and concrete

S/N	Designation of Column	Peak axial force (kN)	Peak bending (kN-m)	Maximum axial strain of steel (mm/mm)	Maximum axial strain of concrete (mm/mm)	Maximum transverse strain of concrete (mm/mm)
1	17RW1-00	750	-	-0.0047	-0.0078	0.0017
2	17RW1-45	249	12.16	0.0016	-0.0039	0.0003
3	17RD1-45	340	16.54	0.0020	-0.0046	0.0003
4	17RC1-45	372	18.98	0.0092	-0.0098	0.0006
5	17RW2-00	1005	-	-0.0034	-0.0059	0.0011
6	17RW2-90	291	27.44	0.0018	-0.0043	0.0002
7	17RD2-90	403	37.64	0.0002	-0.0041	0.0001
8	17RC2-90	444	42.18	0.0169	-0.0088	0.0009
9	10RW1-00	568	-	-0.0057	-0.0061	0.0059
10	10RW1-45	194	9.67	0.0009	-0.0041	0.0076
11	10RD1-45	339	14.98	0.0026	-0.0064	0.0008
12	10RC1-45	327	16.87	0.0176	-0.0138	0.0013
13	10RW2-00	801	-	-0.0059	-0.0078	0.0014
14	10RW2-90	256	23.69	0.0038	-0.0074	0.0009
15	10RD2-90	325	31.36	0.0035	-0.0074	0.0004
16	10RC2-90	440	42.89	0.0063	-0.0100	0.0001
17	10RU1-00	471	-	-0.0044	-0.0048	0.0024

4.7 Toughness and Ductility of Column

4.7.1 Toughness

Toughness measures the column’s ability to deform and absorb energy to release in the plastic range before failure. Toughness enables the redistribution of forces within the column. When subjected to extreme loads, a tough column can absorb and distribute the energy throughout its length, reducing the concentration of stress in specific areas. This redistribution helps prevent localized damage. This property helps prevent sudden or catastrophic failures and allows the structure to recover from significant forces. The toughness of the columns is computed as the area under the stress versus axial strain curves up to 85% of the peak load on the descending branch (Fig. 4.28), (Husem and Pul, 2008).

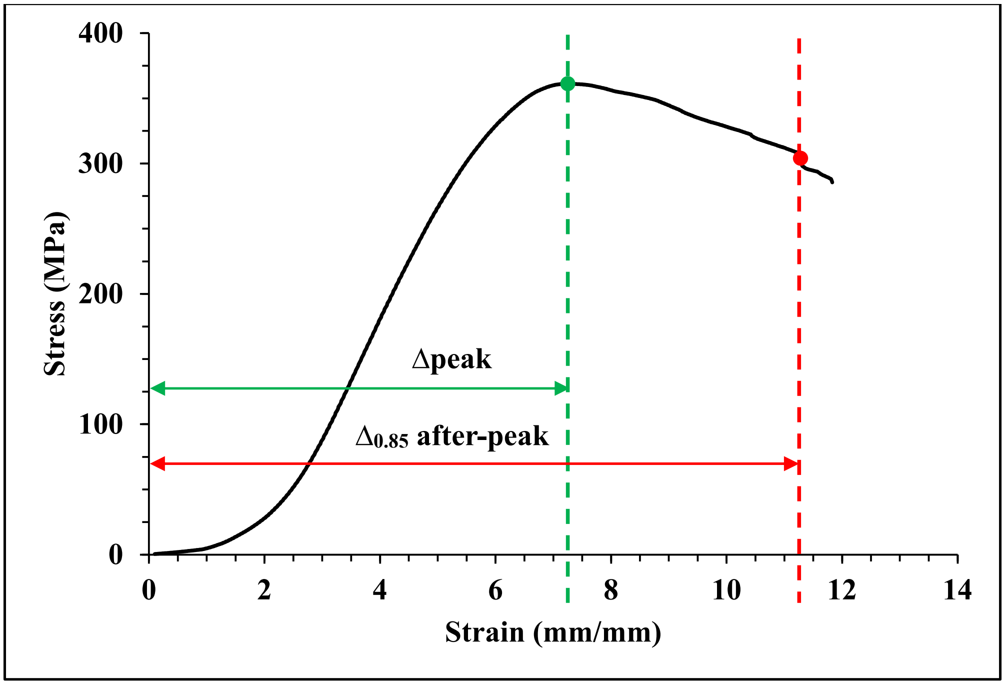

Fig. 4.28: Typical load–deformation curve for determining toughness and ductility.

Fig. 4.29 represents the comparison of the toughness of the columns under concentric and eccentric loading. In general, it can be observed that introducing eccentricity in the loading decreases the toughness of the columns. For 17RW1-45 and 17RW2-90, toughness reduces by 50% and 63%, respectively, compared to 17RW1-00 and 17RW2-00. Similarly, 10RW1-45 toughness was reduced by 50%, and 10RW2-90 was reduced by 75% compared to the 10RW1-00 and 10RW2-00. For the confinement effect of lateral ties, 10RW1-00 exhibited 33% greater toughness than 10RU1-00. Under concentric loading, it can be observed that the increase of column cross-sections increases toughness. Among the eccentrically loaded columns, the confinement effect of CFRP improves the toughness, with significantly higher toughness observed for continuous wrapping compared to the unwrapped and discrete wrapping of the columns.

Continuous confinement of the 150 mm x 150 mm columns caused the toughness of the column to become almost 2.20 and 2.75 times that of the unconfined column of 17 MPa and 10 MPa strength, respectively. However, this ratio for the 150 mm x 225 mm columns is 2 and 4 times, respectively. These ratios are a minimum of 1.83 times for the square column and 1.60 times for the rectangular column, more for continuous to discrete wrapping. From Fig. 4.29, it can be seen that, for discrete wrapping, toughness improvement was not as much as the crushing failure observed at the unconfined portion, but it delayed re-bar buckling. Unfortunately, 17RD1-45 did not show any improvement. Since this signifies higher deformability of the continuous wrapping columns under eccentric loading, the toughness values imply that the addition of CFRP wrapping also causes the ductility to be improved.

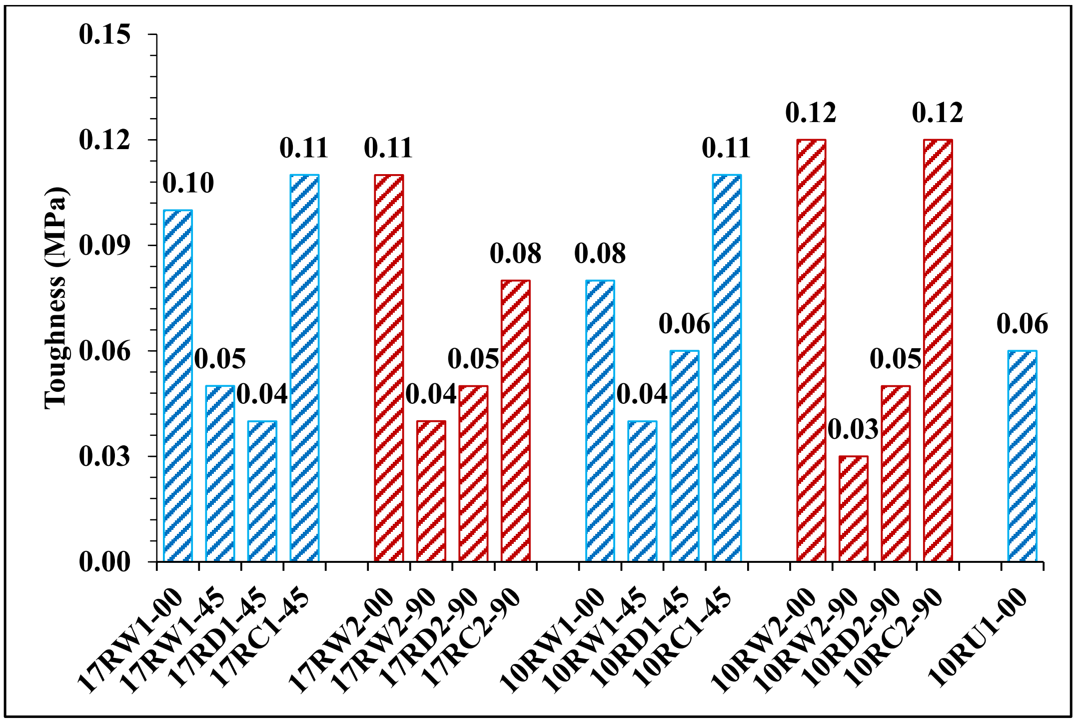

Fig. 4.29: Toughness of the concentric and eccentrically loaded columns.

4.7.2 Ductility

Ductility in a concrete column lies in its ability to provide warning signs, absorb energy, redistribute forces, prevent progressive failure, offer design flexibility, and enhance the seismic performance of structures. The ratio of the ultimate deformation assumed at 85% of the post-peak load ($\Delta_{0.85}$ after-peak) and the deformation at the peak load (Δpeak) is used to calculate the ductility value according to (Fig. 4.28), (Husem and Pul, 2008).

The ductility values of different columns are represented in Fig. 4.30. The general trend indicates that eccentrically loaded columns exhibit more excellent ductility than concentrically loaded ones. Moreover, adding a Carbon Fiber Reinforced Polymer (CFRP) confinement layer improves ductility. For a 150 mm x 150 mm column of 17 MPa strength, the maximum ductility, at 56%, was recorded for the continuously wrapped column (17RC1-45) subjected to eccentric loading. In contrast, the minimum, at 2%, was observed for the unwrapped specimen (17RW1-00) under concentric loading. The discretely wrapped column (17RD1-45) displayed a reduction in ductility by 80% compared to the unwrapped column 17RW1-45 under the same eccentricity of 45 mm, likely due to the non-uniform stiffness of the column. This trend was similarly noted in columns of the same size but of 10 MPa strength.

For a 150 mm x 225 mm column of 10 MPa strength, the continuous wrapped column (10RC2-90) subjected to eccentric loading displayed the highest ductility at 40%. The lowest ductility, at 15%, was exhibited by the discretely wrapped specimen (10RD2-90) under eccentric loading. However, the unwrapped specimen 10RW2-90 under concentric loading demonstrated 17% ductility. The unwrapped column (10RW2-90) showed 66% higher ductility than the discrete column 10RD2-90 under the same eccentricity of 90 mm, pointing towards the uniform stiffness of the column. The same pattern was observed in columns of the same size but of 17 MPa strength. Consequently, it can be concluded that continuous CFRP confinement boosts the ductility of columns by slowing down the development of cracks in the concrete and allowing the columns to sustain more significant deformation after reaching peak load, thus preventing premature failure.

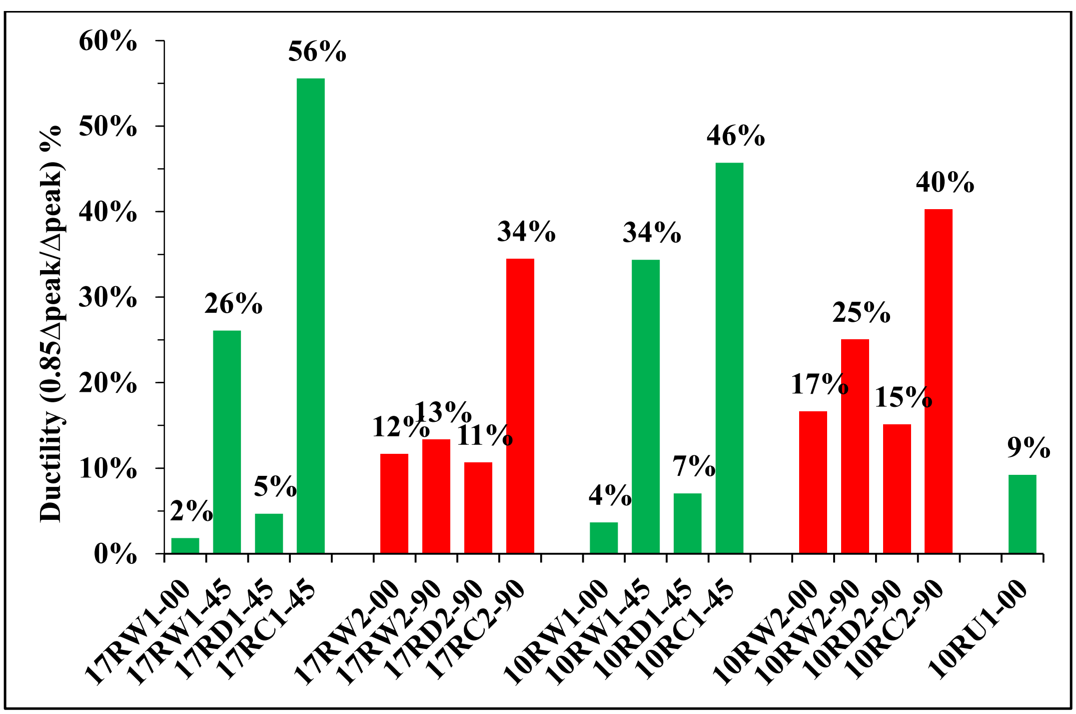

Fig. 4.30: Comparison of the ductility of the tested columns.

4.8 Effect of Tie Bar Confinement

Although the nominal axial load-carrying capacity equation for columns does not incorporate the effect of shear reinforcement, it plays a vital role in a column's capacity and behavior under loading. To investigate the effect of the tie bar confinement, 10RU1-00 and 10RW1-00 are used for comparison. In 10RU1-0, The initial cracks appeared around the column's hunch, beneath the top head, and quickly extended towards the mid-height. The spalling of the concrete cover around the top one-third region characterized the column failure. However, a significant spall-off of the concrete cover was observed on the back side of the column, failing. Upon manual crushing of the column, it was observed that the longitudinal bars did not undergo significant buckling.

On the other hand, in 10RW1-00, significant cracks developed around the mid-height, and the column eventually broke due to concrete disintegration and the clear cover peeling off at the left face mid-portion. Due to the closely spaced ties at the top and bottom, premature cracks at the ends of the columns were prevented. From the load-deformation curves, it can be ascertained that 10RU1-00 failed without showing much deformation. At the same time, the deformation at the peak load is more extended for 10RW1-00. Therefore, the concrete is crushed before reaching large axial deformations due to the absence of internal confinement. At the ultimate failure, 10RW1-00 showed almost 20% more deformation than 10RU1-00. The peak load deformation capacity and a peak load of 10RW1-00 are increased by 26% and 21% due to the addition of lateral ties.

Regarding lateral deformation, 10RW1-00 experienced a more significant increase in the area at peak load, which is 2.01%, whereas 10RU1-0 exhibited a 0.35% increase in area. The axial strain in concrete was also observed at 0.0048 for 10RU1-00 and 0.0061 for 10RW1-00, an increase of 27%. The transverse strain (0.0059) also significantly increased in the case of 10RW1-00 over 10RU1-00, 0.0024. Since there were no lateral ties in 10RU1-0, its longitudinal reinforcement underwent lower yielding and buckling, showing a strain of 0.0044. In contrast, in 10RW1-00, the reinforcement experienced a larger strain of 0.0057, owing to the presence of tie bars. Regarding toughness, 10RW1-00 was found to be more toughness, showing 37% higher than 10RU1-00.

4.9 Code Comparison of Axial Load and Moment Capacity

The analytical axial load-moment (P-M) interaction diagrams for the CFRP-confined (continuous wrapping) eccentric columns have been obtained using the equations provided in Section 2.3.7, as specified in ACI 440.2R-17 (2017). On the other hand, unwrapped columns were analyzed according to the ACI 318-14 (2014) code and by using software namely spColumn (2021). The interaction diagram of a concrete column is a graphical representation that depicts the interaction between axial force and bending moment in the column. It is significant as it allows for strength assessment, identifies failure modes, optimizes design, ensures safety and reliability, complies with design codes, and aids in retrofitting and rehabilitation efforts. Fig. 4.31 and Fig. 4.32 compares the nominal and factored axial force and bending moment capacities obtained from these analyses with experimental capacities. When considering CFRP-confined columns with discrete wrapping, I extrapolated their experimental capacities from the continuous-wrapped column interaction diagrams, as ACI 440.2R-17 (2017) provides no specific predictions, and it is also plotted on unwrapped column interaction diagrams.

Table 4.7 and Fig. 4.33 reveals that, except for the 17RW2-90 column, experimental capacities generally exceeded the code-predicted values under both concentric and eccentric loading. This implies that the codes typically underestimate column capacity. For example, the 10RC2-90 column saw the highest observed increase in axial force (75%) and bending moment capacity (74%) compared to code predictions. The 10RW2-90 column had minor increases at 4% in axial capacity and 6% in bending moment. Notably, the 17RW2-90 column's experimental capacities were 6% less in axial force and 5% less in bending moment than the code predictions. Examining columns 17RW1-45 and 10RW1-45, their experimental capacities exceed code predictions by 11% and 19% for axial capacity and 14% and 21% for bending moment, respectively.

Turning to continuous CFRP-confined wrapped columns, 17RC1-45 surpassed code predictions by 42% in axial capacity and 43% in bending moment. The 10RC1-45 column showed a remarkable 65% increase over code predictions in axial and bending moment capacities. Discrete CFRP-confined wrapped columns identified as 17RD1-45, 17RD2-90, 10RD1-45, and 10RD2-90, the experimental capacities are the peak load and moment values obtained from testing, and compared their values with the codes ACI 318-14 (2014) and ACI 440.2R-17 (2017) as their in no specific predictions.

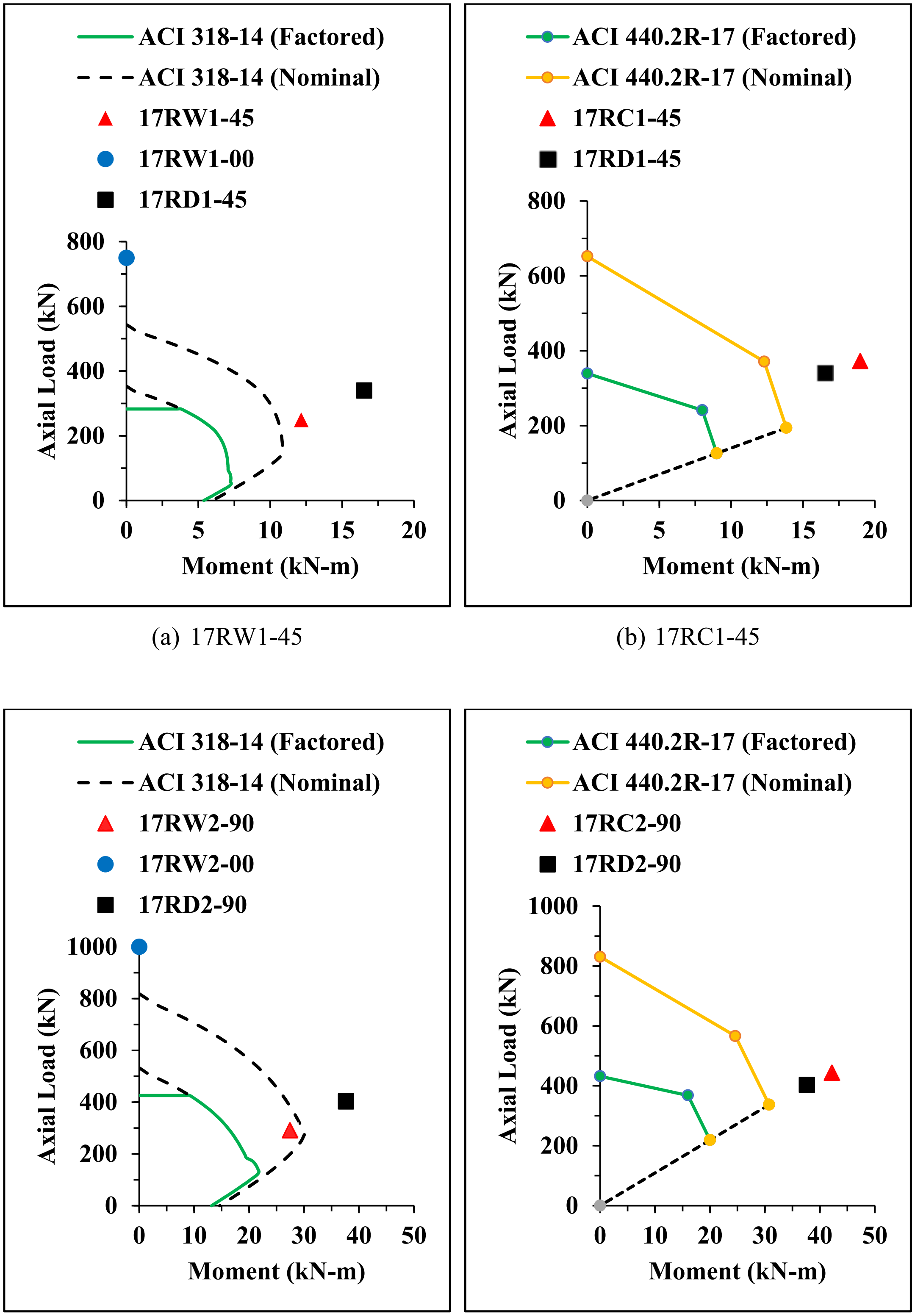

(a) 17RW1-45

(b) 17RC1-45

(c) 17RW2-90

(d) 17RC2-90

Fig. 4.31: Comparison of the experimental axial load and bending moment capacities with the code predictions for 17 MPa columns.

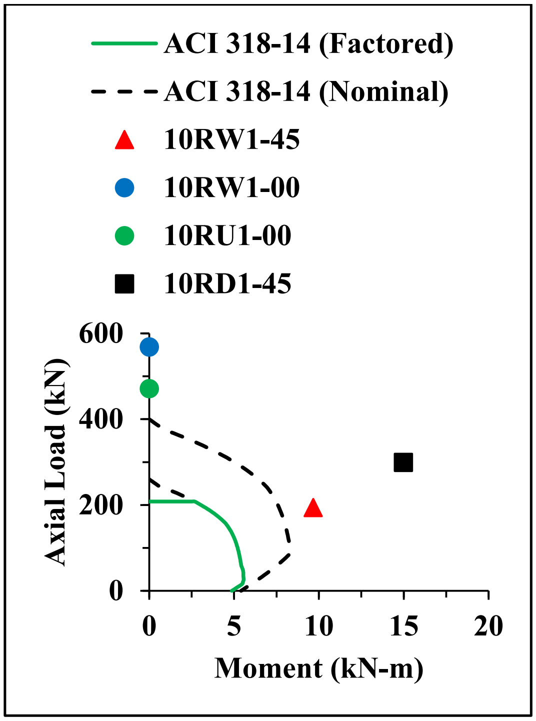

(a) 10RW1-45

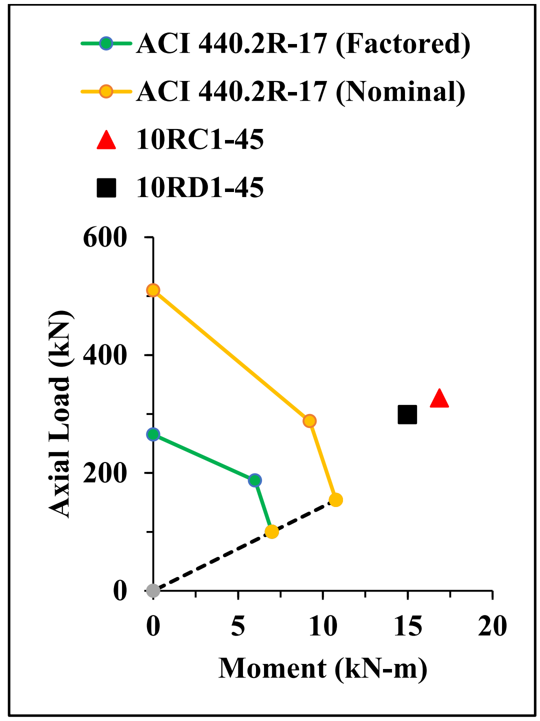

(b) 10RC1-45

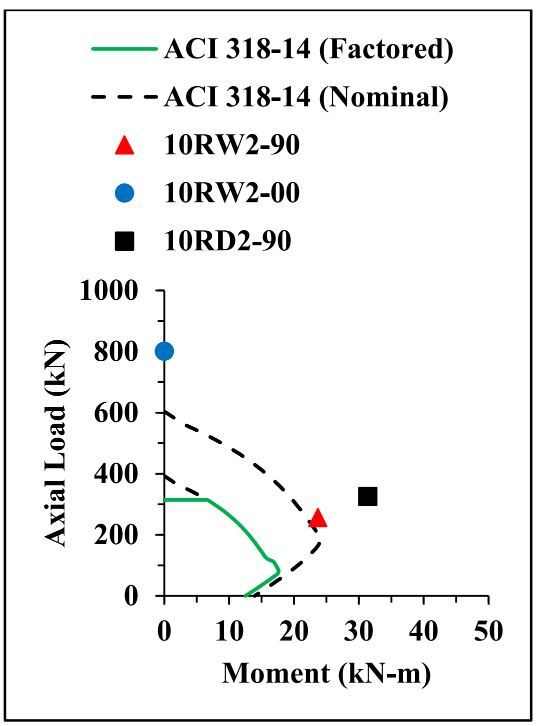

(c) 10RW2-90

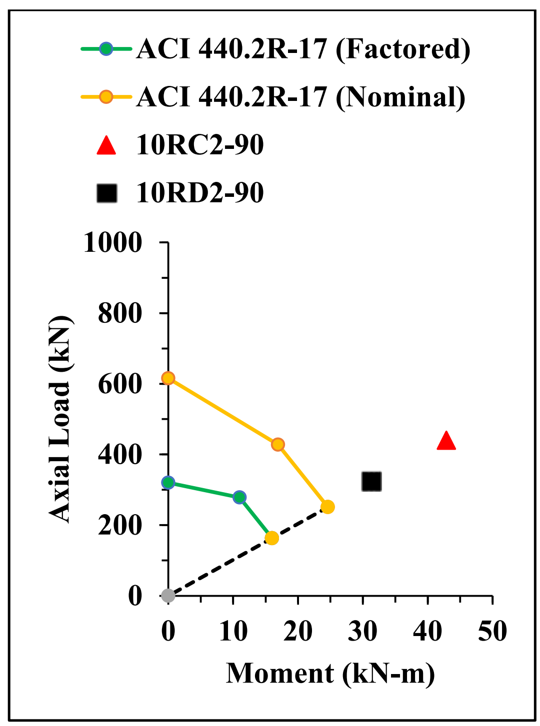

(d) 10RC2-90

Fig. 4.32: Comparison of the experimental axial load and bending moment capacities with the code predictions for 10 MPa columns.

Table 4.7: Experimental capacity verifying with the code prediction

S/N	Designation of column	Experimental capacity		Code predicted nominal capacity		Experimental capacity increased		Code followed
		Peak load (kN)	Peak moment (kN-m)	Axial load, Pn (kN)	Moment, Mn (kN-m)	Axial load (%)	Moment (%)	
1	17RW1-00	750	-	543	-	38%	-	ACI 318
2	17RW1-45	249	12.16	225	10.64	11%	14%	ACI 318
3	17RD1-45	340	16.54	225 (262)	10.64 (13.25)	51% (30%)	55% (25%)	ACI 318 (ACI 440.2R)
4	17RC1-45	372	18.98	262	13.25	42%	43%	ACI 440.2R
5	17RW2-00	1005	-	819	-	23%	-	ACI 318
6	17RW2-90	291	27.44	310	29.00	-6%	-5%	ACI 318
7	17RD2-90	403	37.64	310 (335)	29.00 (30.77)	30% (20%)	30% (22%)	ACI 318 (ACI 440.2R)
8	17RC2-90	444	42.18	335	30.77	33%	37%	ACI 440.2R
9	10RW1-00	568	-	400	-	42%	-	ACI 318
10	10RW1-45	194	9.67	163	8.00	19%	21%	ACI 318
11	10RD1-45	299	14.98	163 (198)	8.00 (10.25)	83% (51%)	87% (46%)	ACI 318 (ACI 440.2R)
12	10RC1-45	327	16.87	198	10.25	65%	65%	ACI 440.2R
13	10RW2-00	801	-	604	-	33%	-	ACI 318
14	10RW2-90	256	23.69	245	22.25	4%	6%	ACI 318
15	10RD2-90	325	31.36	245 (251)	22.25 (24.62)	33% (29%)	41% (27%)	ACI 318 (ACI 440.2R)
16	10RC2-90	440	42.89	251	24.62	75%	74%	ACI 440.2R
17	10RU1-00	471	-	400	-	18%	-	ACI 318

From the axial load-moment (P-M) interaction diagrams (Fig. 4.31 and Fig. 4.32), it is evident that rectangular columns exhibit balanced failure, where, square columns represent compression failure regardless of the concrete strength. Balanced failure of a concrete column reaches its ultimate load-carrying capacity while maintaining a balance between the material's compressive strength and yielding of reinforcement simultaneously. Unlike brittle failure, where the column abruptly collapses without any warning signs, a balanced failure allows for a degree of ductility and deformation, providing a warning through visible cracks and structural distress. It ensures the safety of occupants and allows for potential evacuation before catastrophic collapse. Achieving balanced failure is a testament to careful design and construction practices, emphasizing the reinforcement detailing, and load analysis in ensuring the structural integrity of concrete columns under extreme conditions.

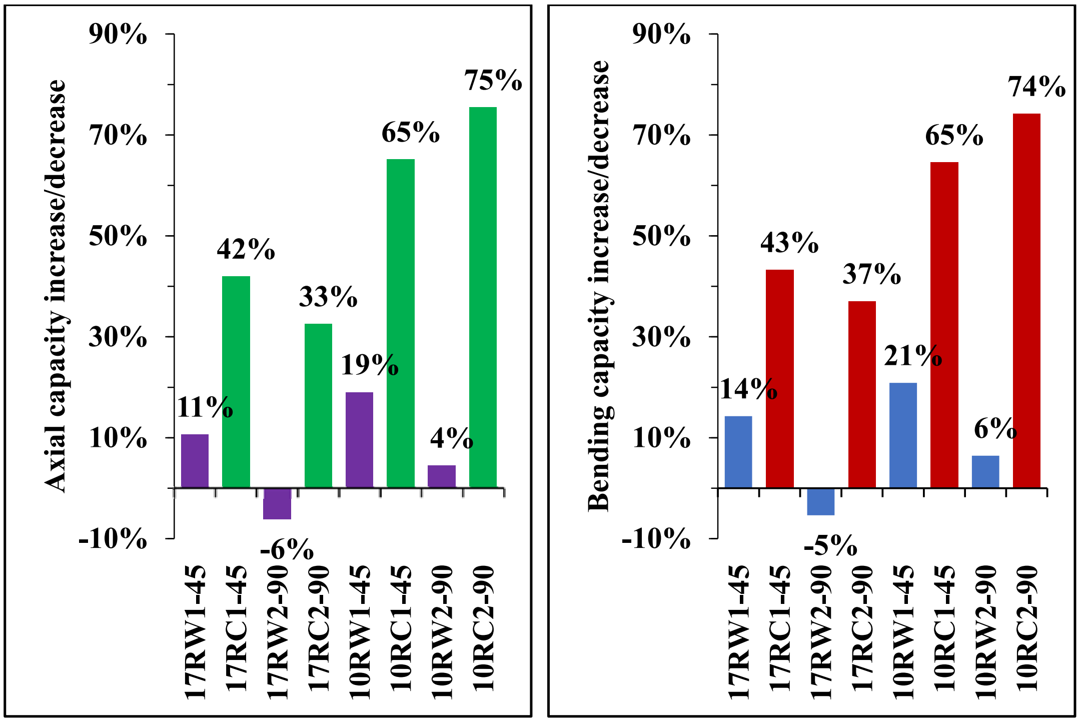

(a) Axial capacity increase/decrease (b) Bending capacity increase/decrease

Fig. 4.33: Experimental axial load and bending moment capacities increment/decrement over code prediction for eccentrically loaded columns.

Comparing the experimental and predicted capacities, it is evident that all the columns exhibited higher experimental capacities. The percentage increase in experimental capacity varied for each column. These results suggest that the tested concrete columns were able to withstand higher loads and moments than initially predicted, indicating their robustness and potentially allowing for more efficient and economical designs in future projects.

In conclusion, while the code predictions for unwrapped columns under eccentric loading are fairly accurate, they tend to be conservative when predicting capacities for continuously wrapped columns under the same conditions. This discrepancy suggests a potential area of improvement in the predictive model.

4.10 Summary

To summarize the findings of this study, it can be concluded that both the compressive strength of the cylinders and the axial capacity of the columns increase due to the addition of CFRP layers. This incremental effect is enhanced for the increased number of layers, although the increase is not linear. The confined compressive strength (*f'cc*) of the concrete increased by 41% and 91% minimum due to the addition of one and two layers of CFRP, respectively, disregarding the concrete substrate and the size effects in the cylinders. On the contrary, using discrete and continuous wrapping increased the axial capacity by at least 27% and 49%, respectively. Still, bending moment capacity increased by at least 32% for discrete and 54% for continuous CFRP confinement, respectively, disdaining the column concrete substrate and the side effects. The columns with CFRP confinement exhibited enhanced axial strain, lateral deformation capacity, toughness, and ductility. Considering both the column sizes, discrete to continuous confinement results in a minimum increase of 9% peak load and 11% bending moment capacity. As expected, the concentrically loaded columns reached higher axial capacities than the eccentric columns, and the column without lateral ties showed lower peak load and axial deformation. However, the unconfined eccentric columns were generally more ductile than the unconfined concentric columns, but discrete wrapped displayed reduced ductility compared to the unwrapped column under the same eccentricity.

CHAPTER 5
CONCLUSIONS AND RECOMMENDATIONS

5.1 General

In Bangladesh, the risk of earthquakes coupled with aging structures necessitates retrofitting these buildings to prevent human casualties and financial loss. The limitations of conventional jacketing techniques underline the importance of researching alternative retrofitting solutions, such as FRP (fiber reinforced polymer) jacketing. Therefore, it is crucial to align the study of FRP retrofitting with the requirements of developing nations to optimize its usage in these contexts.

This research aims to understand the impact of CFRP (carbon fiber reinforced polymer) confinement on various aspects of recycled brick aggregate columns under eccentric load. These aspects include the columns' axial capacity, concrete strain in axial and transverse directions, strain in axial reinforcement, bending moment capacity, toughness, and ductility. The study also explores the axial capacity changes in unconfined recycled brick aggregate columns under eccentric loading compared to concentric loading, the axial capacity of these columns under concentric loading, and the influence of lateral ties on axial capacity and failure modes.

5.2 Conclusions

The following conclusions can be drawn from the experimental findings:

(i) The confined compressive strength ($f'cc$) of the concrete cylinder increased by a minimum of 41% and 91%, respectively, due to the addition of one and two layers of CFRP, disregarding the concrete substrate and the size effects in the cylinders. For cylinders, the 1-ply and 2-ply specimens failed by rupturing the CFRP.

(ii) Due to eccentricity, the unconfined square and rectangular columns lose a maximum of 67% and 71% of their axial capacity, disregarding the concrete strength. The discrete and continuous wrapping increased axial capacity by at least 27% and 49%, respectively, and the corresponding bending moment capacity increased by at least 32% and 54%, disregarding the column concrete substrate and the aspect ratio.

(iii) For the continuously wrapped column, a maximum of 75% axial capacity and 74% bending moment capacity was found over ACI 440.2R-17 (2017) prediction in lower strength (10MPa) concrete. A minimum 33% axial capacity and 37% bending moment capacity was found over ACI 440.2R-17 (2017) prediction in 17 MPa strength concrete. ACI 440.2R-17 (2017) is not a recommended FRP system for concrete that has a compressive strength ($f'c$) of less than 17 MPa, but a higher percentage increase of compressive strength is found in lower strength (10 MPa) concrete. For unwrapped columns under eccentric loading, a maximum of 19% axial capacity and 21% bending moment capacity increment, and 6% axial capacity, 5% bending moment capacity decrement was found over ACI 318-14 (2014) prediction.

(iv) The toughness of the columns is reduced by the introduction of eccentricity. In the eccentric columns, the toughness of the columns increased with increasing CFRP confinement. The continuous CFRP-wrapped column shows a toughness minimum of 2.20 times for the square column and a minimum of 2 times for the rectangular column to the unwrapped column. These ratios are a minimum of 1.83 for the square column and 1.60 times for the rectangular column, more for continuous to discrete wrapping. Moreover, adding a CFRP confinement layer improves ductility. A minimum of 34% ductility was observed for continuous wrapping and 13% for unwrapped columns under eccentric loading, disregarding the concrete strength and sizes.

(v) The tension re-bar shows a minimum of 1.65 times more axial strains under eccentric loading in a continuously CFRP-wrapped column than the unwrapped column. The values of axial strain suggest that yielding of the longitudinal bars occurs at failure. Generally, a square column shows compression failure and a rectangular column shows balanced failure under eccentric loading. For the CFRP-wrapped eccentric columns, the continuously-wrapped columns showed a higher axial strain of concrete, and the general trend showed that the axial strain increased with increasing CFRP confinement. Poisson's ratio was 0.18 - 0.22 under concentric loading of unwrapped columns.

(vi) The failure in the concentric columns with no CFRP confinement consisted of a large concrete spall-off with cracks initiating at the top and propagating towards mid-height. In the eccentric columns, the unconfined columns failed by showing cracks on the tension face and the crushing of the concrete occurring on the compression face. In the columns with discrete wrapping, buckling in the re-bar was observed with concrete crushing at the unconfined portion. The continuously-wrapped columns showed CFRP rupturing at failure with a prominent horizontal fracture on the tension face and the radius of the vertical curve was recognizable, and the concrete core inside showed minor damage.

5.3 Recommendations for Future Study

To incorporate CFRP in structural systems as a means to improve the performance of structural elements, further research is needed to make its operation more practical. Some of the research areas that still need more exploration are as follows:

(i) Development of models to predict the capacity of brick aggregate columns confined with CFRP, particularly those with discrete wrapping, for various cross-sectional shapes.

(ii) Behavior of members strengthened with CFRP systems orienting the fibers combinedly along longitudinal and transverse axis with different aspect ratios R.C members and strength.

REFERENCES

ACI 211.1-91 (1991). Standard practice for selecting proportions for normal, heavyweight, and mass concrete, Farmington Hills, MI, USA, American Concrete Institute.

ACI 224.1R-07 (2007). Causes, evaluation, and repair of cracks in concrete structures, Farmington Hills, MI, USA, American Concrete Institute.

ACI 318-14 (2014). Building code requirements for structural concrete and commentary, Farmington Hills, MI, USA, American Concrete Institute.

ACI 318-19 (2019). Building code requirements for structural concrete and commentary, Farmington Hills, MI, USA, American Concrete Institute.

ACI 440.2R-08 (2008). Guide for the design and construction of externally bonded FRP systems for strengthening concrete structures, Farmington Hills, MI, USA, American Concrete Institute.

ACI 440.2R-17 (2017). Guide for the design and construction of externally bonded FRP systems for strengthening concrete structures, Farmington Hills, MI, USA, American Concrete Institute.

ACI 562-21 (2021). Assessment, repair, and rehabilitation of existing concrete structures - code and commentary, Farmington Hills, MI, USA, American Concrete Institute.

Ahmed, I., Gajendran, T., Brewer, G., Maund, K., Von Meding, J., Kabir, H., Faruk, M., Shrestha, H. D. & Sitoula, N. (2019). Opportunities and challenges of compliance to safe building codes: Bangladesh and Nepal. APN Science Bulletin, Vol. 9, pp. 73–80.

Amin, A. F. M. S. & Choudhury, J. R. (2015). Intrinsic properties of brick aggregate concrete. Advances in Civil Infrastructure and Construction Materials, MIST, Dhaka, Bangladesh (CICM 2015).

Apu, N. & Das, U. (2020). Tectonics and earthquake potential of Bangladesh: a review. International Journal of Disaster Resilience in the Built Environment, Vol. 12, pp. 295-307.

ASTM A615/A615M-22 (2022). Standard specification for deformed and plain carbon-steel bars for concrete reinforcement, West Conshohocken, PA, USA, ASTM International.

ASTM C29/C29M-17a (2017). Standard test method for bulk density (“unit weight”) and voids in aggregate, West Conshohocken, PA, USA, ASTM International.

ASTM C31/C31M-22 (2022). Standard practice for making and curing concrete test specimens in the field, West Conshohocken, PA, USA, ASTM International.

ASTM C39/C39M-21 (2021). Standard test method for compressive strength of cylindrical concrete specimens, West Conshohocken, PA, USA, ASTM International.

ASTM C67/C67M-21 (2021). Standard test methods for sampling and testing brick and structural clay tile, West Conshohocken, PA, USA, ASTM International.

ASTM C109/C109M-21 (2021). Standard test method for compressive strength of hydraulic cement mortars, West Conshohocken, PA, USA, ASTM International.

ASTM C128-22 (2022). Standard test method for relative density (specific gravity) and absorption of fine aggregate, West Conshohocken, PA, USA, ASTM International.

ASTM C136/C136M-19 (2019). Standard test method for sieve analysis of fine and coarse aggregates, West Conshohocken, PA, USA, ASTM International.

ASTM C138/C138M-17a (2017). Standard test method for density (unit weight), yield, and air content (gravimetric) of concrete, West Conshohocken, PA, USA, ASTM International.

ASTM C143/C143M-20 (2020). Standard test method for slump of hydraulic-cement concrete, West Conshohocken, PA, USA, ASTM International.

ASTM C187-16 (2016). standard test method for amount of water required for normal consistency of hydraulic cement paste, West Conshohocken, PA, USA, ASTM International.

ASTM C188-17 (2017). Standard test method for density of hydraulic cement, West Conshohocken, PA, USA, ASTM International.

ASTM C191-21 (2021). Standard test methods for time of setting of hydraulic cement by vicat needle, West Conshohocken, PA, USA, ASTM International.

ASTM C469/C469M-22 (2022). Standard test method for static modulus of elasticity and poisson's ratio of concrete in compression, West Conshohocken, PA, USA, ASTM International.

ASTM C496/C496M-17 (2017). Standard test method for splitting tensile strength of cylindrical concrete specimens, West Conshohocken, PA, USA, ASTM International.

ASTM C535-16 (2016). Standard test method for resistance to degradation of large-size coarse aggregate by abrasion and impact in the los angeles machine, West Conshohocken, PA, USA, ASTM International.

ASTM C595/C595M-21 (2021). Standard specification for blended hydraulic cements, West Conshohocken, PA, USA, ASTM International.

ASTM D3039/D3039M-17 (2017). Standard test method for tensile properties of polymer matrix composite materials, West Conshohocken, PA, USA, ASTM International.

Bartos, P. J. M., Sonebi, M. & Tamimi, A. K. (2002). Workability and rheology of fresh concrete: compendium of tests, ENS, CACHAN Cedex, FRANCE, The International Union of Testing and Research Laboratories for Materials and Structures.

BNBC (2020). Bangladesh National Building Code (BNBC). Ministry of Housing and Public Works.

Cachim, P. B. (2009). Mechanical properties of brick aggregate concrete. Construction and Building Materials, Vol. 23, pp. 1292-1297.

Cascardi, A., Lerna, M., Micelli, F. & Aiello, M. A. (2020). Discontinuous FRP-confinement of masonry columns. Frontiers in Built Environment, Vol. 5.

Chen, G. M., He, Y. H., Jiang, T. & Lin, C. J. (2016). Behavior of cfrp-confined recycled aggregate concrete under axial compression. Construction and Building Materials, Vol. 111, pp. 85-97.

Chen, G. M., Zhang, J. J., Jiang, T., Lin, C. J. & He, Y. H. (2018). Compressive behavior of cfrp-confined recycled aggregate concrete in different-sized circular sections. Journal of Composites for Construction, ASCE, Reston, VA, USA, Vol. 22.

Choudhury, M. S. I., Amin, A. F. M. S., Islam, M. M. & Hasnat, A. (2016). Effect of confining pressure distribution on the dilation behavior in FRP-confined plain concrete columns using stone, brick and recycled aggregates. Construction and Building Materials, Vol. 102, pp. 541-551.

CNR (2013). Guide for the design and construction of externally bonded frp systems for strengthening existing structures, Roma, Italy, National Research Council.

Debieb, F. & Kenai, S. (2008). The use of coarse and fine crushed bricks as aggregate in concrete. Construction and Building Materials, Vol. 22, pp. 886-893.

FIB (2001). Design and use of externally bonded fibre reinforced polymer reinforcement (FRP EBR) for reinforced concrete structures, Lausanne, Switzerland, International Federation for Structural Concrete.

Gao, C., Huang, L., Yan, L., Kasal, B. & Li, W. (2016). Behavior of glass and carbon FRP tube encased recycled aggregate concrete with recycled clay brick aggregate. Composite Structures, Vol. 155, pp. 245-254.

Guo, Y. C., Xiao, S. H., Luo, J. W., Ye, Y. Y. & Zeng, J. J. (2018). Confined concrete in fiber-reinforced polymer partially wrapped square columns: axial compressive behavior and strain distributions by a particle image velocimetry sensing technique. Sensors (Basel), Vol. 18.

Gutiérrez, J. P., Martínez, S., De Diego, A., Castro, V. J. & Echevarría, L. (2021). Experimental analysis and design strength models adopted by international guides for FRP-confined concrete columns subjected to axial compression. Materiales de Construcción, Vol. 71.

Hadi, M. N. S. (2005). The behaviour of FRP wrapped HSC columns under different eccentric loads. Composite Structures, Vol. 78, pp. 560-566.

Hadi, M. N. S. & Widiarsa, I. B. R. (2012). Axial and flexural performance of square rc columns wrapped with cfrp under eccentric loading. Journal of Composites for Construction, Vol. 16, pp. 640-649.

Hasnat, A., Islam, M. M. & Amin, A. F. M. S. (2016). Enhancing the debonding strain limit for CFRP-strengthened RC beams using U-clamps: identification of design parameters. Journal of Composites for Construction, ASCE, Reston, VA, USA, Vol. 20.

Husem, M. & Pul, S. (2008). Investigation of stress-strain models for confined high strength concrete. Sadhana, Vol. 32, pp. 243-252.

ICRI 310.2R (2013). Selecting and specifying concrete surface preparation for sealers, coatings, polymer overlays, and concrete repair, Rosemont, IL, USA, International Concrete Repair Institute.

Ilki, A., Peker, O., Karamuk, E., Demir, C. & Kumbasar, N. (2008). FRP retrofit of low and medium strength circular and rectangular reinforced concrete columns. Journal of Materials in Civil Engineering, ASCE, Reston, VA, USA, Vol. 20, pp. 169-188.

Islam, M. J., Alam, M. R., Islam, M. R. & Hasanuzzaman, M. (2020). Evaluation of commonly used aggregates for sustainable infrastructure development in Bangladesh. International Journal of GEOMATE, Vol. 18, pp. 98-104.

Islam, M. M., Choudhury, M. S. I. & Amin, A. F. M. S. (2016). Dilation effects in FRP-confined square concrete columns using stone, brick, and recycled coarse aggregates. Journal of Composites for Construction, ASCE, Reston, VA, USA, Vol. 20.

Jena, T. & Kaewunruen, S. (2021). Life cycle sustainability assessments of an innovative FRP composite footbridge. Sustainability, Vol. 13.

Jiang, T. & Teng, J. G. (2007). Analysis-oriented stress–strain models for FRP–confined concrete. Engineering Structures, Vol. 29, pp. 2968-2986.

Jiang, T., Wang, X. M., Zhang, W. P., Chen, G. M. & Lin, Z. H. (2020). Behavior of FRP-confined recycled brick aggregate concrete under monotonic compression. Journal of Composites for Construction, ASCE, Reston, VA, USA, Vol. 24.

Kelam, A. A., Karimzadeh, S., Yousefibavil, K., Akgün, H., Askan, A., Erberik, M. A., Koçkar, M. K., Pekcan, O. & Ciftci, H. (2022). An evaluation of seismic hazard and potential damage in Gaziantep, Turkey using site specific models for sources, velocity structure and building stock. Soil Dynamics and Earthquake Engineering, Vol. 154, pp. 107129.

Khalaf, F. M. (2006). Using crushed clay brick as coarse aggregate in concrete. Journal of Materials in Civil Engineering, ASCE, Reston, VA, USA, Vol. 18, pp.518-526.

Khalaf, F. M. & Devenny, A. S. (2004). Recycling of demolished masonry rubble as coarse aggregate in concrete: Review, Journal of Materials in Civil Engineering, ASCE, Reston, VA, USA, Vol. 16, pp. 331-340.

Kumutha, R., Vaidyanathan, R. & Palanichamy, M. S. (2007). Behaviour of reinforced concrete rectangular columns strengthened using GFRP. Cement and Concrete Composites, Vol. 29, pp. 609-615.

Lam, L. & Teng, J. G. (2002). Strength models for fiber-reinforced plastic-confined concrete. Journal of Structural Engineering, ASCE, Reston, VA, USA, Vol. 128, pp. 612-623.

Lam, L. & Teng, J. G. (2003). Design-oriented stress-strain model for frp-confined concrete in rectangular columns. Journal of Reinforced Plastics and Composites, The Hong Kong Polytechnic University, Hong Kong, China, Vol. 22, pp. 1149-1186.

Lim, J. C. & Ozbakkaloglu, T. (2015). Investigation of the influence of the application path of confining pressure: tests on actively confined and FRP-confined concretes, Journal of Structural Engineering, ASCE, Reston, VA, USA, Vol. 141.

Mia, M. S., Miah, M. K. & Hasan, M. (2015). Relationship between modulus of elasticity and strength of brick aggregate concrete. International Conference (IICSD-2015).

Miller, D. (2013). Last nightshift in savar: the story of the spectrum sweater factory collapse, Alnwick, Northumberland, England, McNidder & Grace, Vol. 68, pp. 341.

Mohammed, T. U., Hasnat, A., Awal, M. A. & Bosunia, S. Z. (2015). Recycling of brick aggregate concrete as coarse aggregate. Journal of Materials in Civil Engineering, ASCE, Reston, VA, USA, Vol. 27.

Momin, S. M. (2023). Devastation in Turkey: Lessons for Bangladesh [Online]. The Business Post. Available: https://businesspostbd.com/editorial.

Nadim, M. H., Islam, M. M., Mustafiz, S. & Mitra, D. K. (2019). Evaluating the efficiency of Carbon Fiber Reinforced Polymer (CFRP) in increasing the compressive strength of circular concrete column. Journal of Construction and Building Materials Engineering, Vol. 5.

Pantazopoulou, S. J., Bonacci, J. F., Sheikh, S., Thomas, M. D. A. & Hearn, N. (2001). Repair of corrosion-damaged columns with frp wraps. Journal of Composites for Construction, ASCE, Reston, VA, USA, Vol. 5, pp. 3-11.

Parvin, A. & Wang, W. (2001). Behavior of FRP jacketed concrete columns under eccentric loading. Journal of Composites for Construction, ASCE, Reston, VA, USA, Vol. 5, pp. 146-152.

Paul, S., Babafemi, A., Anggraini, V. & Rahman, M. (2018). Properties of normal and recycled brick aggregates for production of medium range (25–30 mpa) structural strength concrete. Buildings, Vol. 8.

Pendhari, S. S., Kant, T. & Desai, Y. M. (2008). Application of polymer composites in civil construction: A general review. Composite Structures, Vol. 84, pp. 114-124.

Ranjan, P. & Dhiman, P. (2016). Retrofitting of columns of an existing building by RC, FRP and SFRC jacketing techniques. IOSR Journal of Mechanical and Civil Engineering, Vol. 01, pp. 40-46.

Seffo, M. & Hamcho, M. (2012). Strength of concrete cylinder confined by composite materials (CFRP). Energy Procedia, Vol. 19, pp. 276-285.

Spcolumn (2021). Designing and investigating reinforced concrete sections subject to combined axial and flexural loads. Skokie, IL, USA: Structure Point.

Teng, J. G., Zhao, J. L., Yu, T., Li, L. J. & Guo, Y. C. (2015). Behavior of FRP-confined compound concrete containing recycled concrete lumps. Journal of Composites for Construction, ASCE, Reston, VA, USA, Vol. 20.

TR55 (2000). Design guidence for strengthening concrete structures using fire composite materials, Croethorne, Berkshire, UK, The Concrete Society.

Yardley, J. (2013). Report on deadly factory collapse in bangladesh finds widespread blame [Online]. The New York Times, Available: https://www.nytimes.com/world/asia.

APPENDIX A
CAPACITY CALCULATION OF THE COLUMNS

Calculation for Column 17RC1-45

(Calculation performed by using PTC Mathcad Prime 5.0.0.0 software.)

Table A. 1: Geometric and Mechanical Properties

$f'_c = 22.90$ MPa	$\varepsilon f_u = 0.021$
$f_y = 391$ MPa	$E_f = 240$ GPa
$\gamma_c = 15$ mm	$C_E = 0.95$
$b = 150$ mm	$k\varepsilon = 0.55$
$h = 150$ mm	$n = 1$
$A_{st} = 328$ mm^2	$\psi_f = 0.95$
$\rho_g = 0.0145$	$E_c = 17945$ MPa
$Ø = 0.65$	$d' = 40$ mm
$\varepsilon'_c = 0.002$	$E_y = 200$ GPa
$t_f = 0.111$ mm	$\varepsilon_{sy} = 0.00195$
$f_{fu} = 4900$ MPa	

$d = h - d' = 110$ mm

$D_e = \sqrt{b^2 + h^2} = 212.132$ mm

$A_g = b \text{ x } h = (2.25 \text{ x} 10^4)$ mm^2

$\varepsilon f_e = k\varepsilon \text{ x } \varepsilon f_u \text{ x } C_E = 0.011$

$$A_e = 1 - \frac{\left(\left(\frac{b}{h}\right) \text{x} (h - 2 \text{ x } r_c)^2 + \left(\frac{h}{b}\right) \text{x} (b - 2 \text{ x } r_c)^2\right)}{3A_g} - \rho_g = 0.559$$

$A_c = 1 - \rho_g = 0.986$

$\text{Ratio} = \frac{A_e}{A_c} = 0.567$

$k_a = \text{Ratio x} \left(\frac{b}{h}\right)^2 = 0.567$

$k_b = \text{Ratio x} \left(\frac{h}{b}\right)^{0.50} = 0.567$

Point A (Uniform/Max Compression)

$f_l = \frac{(2x\ E_f\ x\ n\ x\ t_f\ x\ \varepsilon f_e)}{D_e} = 2.756$ MPa

Confinement $= \frac{f_l}{f'_c} = 0.12$

$f'_{cc} = f'_c + \psi_f$ x 3.3 x ka x $f_l = 27.8$ MPa

$\varepsilon_{cuu} = \varepsilon'_c$ x $(1.50 + 12$ x k_b x $\frac{f_l}{f'_c}$ x $\left(\frac{\varepsilon f_e}{\varepsilon'_c}\right)^{0.45})$ = 0.0065 < 0.01 in

$ØP_n$ (a) = 0.8 Ø x (0.85f'_{cc} x (A_g - A_{st}) + f_y. x A_{st}) = 339 kN

Point B ($\varepsilon_t = 0$; $f_s = 0$)

$\varepsilon f_e = 0.004$ (Minimum)

$f_l = \frac{(2x\ E_f\ x\ n\ x\ t_f\ x\ \varepsilon f_e)}{D_e} = 1.005$ MPa

Confinement $= \frac{f_l}{f'_c} = 0.04$

$f'_{cc} = f'_c + \psi_f$ x 3.3 x ka x $f_l = 24.69$ MPa

$\varepsilon_{cuu} = \varepsilon'_c$ x $(1.50 + 12$ x k_b x $\frac{f_l}{f'_c}$ x $\left(\frac{\varepsilon f_e}{\varepsilon'_c}\right)^{0.45})$ = 0.0038 < 0.01 in

$E_2 = \frac{(f'_{cc} - f'_c)}{\varepsilon_{ccu}} = 468.077$ MPa

$\varepsilon'_t = \frac{2f'_c}{E_c - E_2} = 0.003$

c = d = 110 mm

$y_t = c\ x \frac{\varepsilon'_t}{\varepsilon_{ccu}} = 75.55$ mm

$A = \frac{-b\ x\ (E_c - E_2)^2}{12\ f'_c}$ x $(\frac{\varepsilon_{ccu}}{c})^2 = -2.006$ x $10^{-4}\ \frac{kN}{mm^3}$

$B = \frac{b\ x\ (E_c - E_2)}{2}$ x $(\frac{\varepsilon_{ccu}}{c}) = 45.467$ MPa

$C = -b \times f'_c = -3.435\ \frac{kN}{mm}$

$D = b \times c \times f'_c + \frac{b \times c \times E_2}{2} \times \varepsilon_{ccu} = 393$ kN

$E = \frac{-b \times (E_c - E_2)^2}{16 \times f'_c} \times (\frac{\varepsilon_{ccu}}{c})^2 = -1.505 \times 10^{-4}\ \frac{kN}{mm^3}$

$F = (b \times \left(c - \frac{h}{2}\right) \times \frac{(E_c - E_2)^2}{12\, f'_c} \times (\frac{\varepsilon_{ccu}}{c})^2 + \frac{b \times (E_c - E_2)}{3} \times (\frac{\varepsilon_{ccu}}{c})) = 37.333$ MPa

$G = -(\frac{b \times f'_c}{2} + b \times \left(c - \frac{h}{2}\right) \times \frac{(E_c - E_2)}{2} \times (\frac{\varepsilon_{ccu}}{c})) = -3.31\ \frac{kN}{mm}$

$H = b \times f'_c \times (c - \frac{h}{2}) = 120.225$ kN

$I = -(\frac{b \times c^2}{2} \times f'_c - b \times c \times f'_c \times \left(c - \frac{h}{2}\right) + \frac{b \times c^2 \times E_2}{3} \times \varepsilon_{ccu} - \frac{b \times c \times E_2}{2} \times \left(c - \frac{h}{2}\right) \times \varepsilon_{ccu})$

$= 8122$ kN.mm

$A_{s1} = 164\ mm^2$	$A_{s2} = 0\ mm^2$	$A_{s3} = 0\ mm^2$	$A_{s4} = 164\ mm^2$
$f_{s1} = 391$ MPa	$f_{s2} = 0$ MPa	$f_{s3} = 0$ MPa	$f_{s4} = -391$ MPa
$d_1 = 35$ mm	$d_2 = 0$ mm	$d_3 = 0$ mm	$d_4 = -35$ mm

$ØP_n (b) = Ø \times (A \times (y_t)^3 + B \times (y_t)^2 + C \times (y_t) + D + (A_{s1} \times f_{s1} + A_{s2} \times f_{s2} + A_{s3} \times f_{s3})) = 241$ kN

$ØM_n (b) = Ø \times (E \times (y_t)^4 + F \times (y_t)^3 + G \times (y_t)^2 + H \times (y_t) + I + (A_{s1} \times f_{s1} \times d_1 + A_{s2} \times f_{s2} \times d_2 + A_{s3} \times f_{s3} \times d_3)) = 8$ kN.m

Point C (Balance Point)

$\varepsilon f_e = 0.004$

$f_l = \frac{(2 \times E_f \times n \times t_f \times \varepsilon f_e)}{D_e} = 1.005$ MPa

Confinement $= \frac{f_l}{f'_c} = 0.04$

$f'_{cc} = f'_c + \psi_f \times 3.3 \times ka \times f_l = 24.69$ MPa

$\varepsilon_{cuu} = \varepsilon'_c \times (1.50 + 12 \times k_b \times \frac{f_l}{f'_c} \times \left(\frac{\varepsilon f_e}{\varepsilon'_c}\right)^{0.45}) = 0.0038 < 0.01$ in

$E_2 = \frac{(f'_{cc} - f'_c)}{\varepsilon_{ccu}} = 468.077$ MPa

$\varepsilon'_t = \frac{2f'_c}{E_c - E_2} = 0.003$

$c = d \text{ x } \frac{\varepsilon_{ccu}}{(\varepsilon_{sy} + \varepsilon_{ccu})} = 72.797$ mm

$y_t = c \text{ x } \frac{\varepsilon'_t}{\varepsilon_{ccu}} = 50$ mm

$A = \frac{-b \text{ x } (E_c - E_2)^2}{12 f'_c} \text{ x } (\frac{\varepsilon_{ccu}}{c})^2 = -4.58 \text{ x } 10^{-4} \frac{kN}{mm^3}$

$B = \frac{bx\,(E_c - E_2)}{2} \text{ x } (\frac{\varepsilon_{ccu}}{c}) = 68.704$ MPa

$C = -b \text{ x } f'_c = -3.435 \frac{kN}{mm}$

$D = b \text{ x } c \text{ x } f'_c + \frac{b \text{ x } c \text{ x } E_2}{2} \text{ x } \varepsilon_{ccu} = 260$ kN

$E = \frac{-b \text{ x } (E_c - E_2)^2}{16x\, f'_c} \text{ x } (\frac{\varepsilon_{ccu}}{c})^2 = -3.435 \text{ x } 10^{-4} \frac{kN}{mm^3}$

$F = (b \text{ x } \left(c - \frac{h}{2}\right) x \frac{(E_c - E_2)^2}{12 f'_c} \text{ x } \left(\frac{\varepsilon_{ccu}}{c}\right)^2 + \frac{bx\,(E_c - E_2)}{3} \text{ x } (\frac{\varepsilon_{ccu}}{c})) = 44.793$ MPa

$G = -(\frac{b \text{ x } f'_c}{2} + b \text{ x} \left(c - \frac{h}{2}\right) x \frac{(E_c - E_2)}{2} \text{ x}(\frac{\varepsilon_{ccu}}{c})) = -1.57 \frac{kN}{mm}$

$H = b \text{ x } f'_c \text{ x } (c - \frac{h}{2}) = -7.568$ kN

$I = -(\frac{b \text{ x } c^2}{2} \text{ x } f'_c - b \text{ x } c \text{ x } f'_c \text{ x} \left(c - \frac{h}{2}\right) + \frac{b \text{ x } c^2 \text{ x } E_2}{3} \text{ x } \varepsilon_{ccu} - \frac{b \text{ x } c \text{ x } E_2}{2} \text{ x} \left(c - \frac{h}{2}\right) \text{ x } \varepsilon_{ccu})$

= 10147 kN.mm

$A_{s1} = 164\ mm^2$	$A_{s2} = 0\ mm^2$	$A_{s3} = 0\ mm^2$	$A_{s4} = 164\ mm^2$
$f_{s1} = 342$ MPa	$f_{s2} = 0$ MPa	$f_{s3} = 0$ MPa	$f_{s4} = -391$ MPa
$d_1 = 35$ mm	$d_2 = 0$ mm	$d_3 = 0$ mm	$d_4 = -35$ mm

$ØP_n(c) = Ø \text{ x } (A \text{ x } (y_t)^3 + B \text{ x } (y_t)^2 + C \text{ x } (y_t) + D + (A_{s1} \text{ x } f_{s1} + A_{s2} \text{ x } f_{s2} + A_{s3} \text{ x } f_{s3} + A_{s4} \text{ x } f_{s4}))$
= 126 kN

$ØM_n(c) = Ø \times (E \times (y_t)^4 + F \times (y_t)^3 + G \times (y_t)^2 + H \times (y_t) + I + (A_{s1} \times f_{s1} \times d_1 + A_{s2} \times f_{s2} \times d_2 + A_{s3} \times f_{s3} \times d_3 + A_{s4} \times f_{s4} \times d_4)) = 9$ kN.m

Calculation for Column 17RC2-90

Table A. 2: Geometric and Mechanical Properties

$f'_c = 22.90$ MPa	$\varepsilon f_u = 0.021$
$f_y = 333$ MPa	$E_f = 240$ GPa
$\gamma_c = 15$ mm	$C_E = 0.95$
$b = 150$ mm	$k\varepsilon = 0.55$
$h = 225$ mm	$n = 1$
$A_{st} = 408$ mm^2	$\psi_f = 0.95$
$\rho_g = 0.012$	$E_c = 17945$ MPa
$Ø = 0.65$	$d' = 40$ mm
$\varepsilon'_c = 0.002$	$E_y = 186$ GPa
$t_f = 0.111$ mm	$\varepsilon_{sy} = 0.00179$
$f_{fu} = 4900$ MPa	

$d = h - d' = 185$ mm

$D_e = \sqrt{b^2 + h^2} = 270.416$ mm

$A_g = b \times h = (3.375 \times 10^4)$ mm^2

$\varepsilon f_e = k\varepsilon \times \varepsilon f_u \times C_E = 0.011$

$$A_e = 1 - \frac{\left(\left(\frac{b}{h}\right) \times (h - 2 \times r_c)^2 + \left(\frac{h}{b}\right) \times (b - 2 \times r_c)^2\right)}{3A_g} - \rho_g = 0.524$$

$A_c = 1 - \rho_g = 0.988$

$\text{Ratio} = \frac{A_e}{A_c} = 0.531$

$k_a = \text{Ratio} \times \left(\frac{b}{h}\right)^2 = 0.236$

$k_b = \text{Ratio} \times \left(\frac{h}{b}\right)^{0.50} = 0.65$

Point A (Uniform/Max Compression)

$f_l = \frac{(2x\ E_f\ x\ n\ x\ t_f\ x\ \varepsilon f_e)}{D_e} = 2.162$ MPa

Confinement $= \frac{f_l}{f'_c} = 0.09$

$f'_{cc} = f'_c + \psi_f$ x 3.3 x ka x $f_l = 24.5$ MPa

$\varepsilon_{cuu} = \varepsilon'_c \text{ x } (1.50 + 12 \text{ x } k_b \text{ x } \frac{f_l}{f'_c} \text{ x } \left(\frac{\varepsilon f_e}{\varepsilon'_c}\right)^{0.45}) = 0.0062 < 0.01$ in

$ØP_n$ (a) = 0.8 Ø x (0.85f'_{cc} x (A_g - A_{st}) + $f_{y.}$ x A_{st}) = 432 kN

Point B (ε_t = 0; f_s =0)

$\varepsilon f_e = 0.004$ (Minimum)

$f_l = \frac{(2x\ E_f\ x\ n\ x\ t_f\ x\ \varepsilon f_e)}{D_e} = 0.788$ MPa

Confinement $= \frac{f_l}{f'_c} = 0.03$

$f'_{cc} = f'_c + \psi_f$ x 3.3 x k_a x $f_l = 23.48$ MPa

$\varepsilon_{cuu} = \varepsilon'_c \text{ x } (1.50 + 12 \text{ x } k_b \text{ x } \frac{f_l}{f'_c} \text{ x } \left(\frac{\varepsilon f_e}{\varepsilon'_c}\right)^{0.45}) = 0.0037 < 0.01$ in

$E_2 = \frac{(f'_{cc} - f'_c)}{\varepsilon_{ccu}} = 156.088$ MPa

$\varepsilon'_t = \frac{2f'_c}{E_c - E_2} = 0.003$

c = d = 185 mm

$y_t = c \text{ x } \frac{\varepsilon'_t}{\varepsilon_{ccu}} = 127.58$ mm

$A = \frac{-b \text{ x } (E_c - E_2)^2}{12\ f'_c} \text{ x } (\frac{\varepsilon_{ccu}}{c})^2 = -7.034 \text{ x } 10^{-5} \frac{kN}{mm^3}$

$B = \frac{b \text{ x } (E_c - E_2)}{2} \text{ x } (\frac{\varepsilon_{ccu}}{c}) = 26.924$ MPa

C = -b x f’$_c$ = -3.435 $\frac{kN}{mm}$

D = b x c x $f'_c + \frac{b \text{ x } c \text{ x } E_2}{2}$ x ε_{ccu} = 644 kN

E = $\frac{-b \text{ x } (E_c - E_2)^2}{16 \text{ x } f'_c}$ x$(\frac{\varepsilon_{ccu}}{c})^2$ = -5.276 x 10^{-5} $\frac{kN}{mm^3}$

F = (b x $\left(c - \frac{h}{2}\right)$ x $\frac{(E_c - E_2)^2}{12 f'_c}$ x $(\frac{\varepsilon_{ccu}}{c})^2 + \frac{b \text{ x } (E_c - E_2)}{3}$ x $(\frac{\varepsilon_{ccu}}{c})$) = 23.049 MPa

G = $-(\frac{b \text{ x } f'_c}{2}$ + b x $\left(c - \frac{h}{2}\right)$ x $\frac{(E_c - E_2)}{2}$ x $(\frac{\varepsilon_{ccu}}{c})$) = -3.67 $\frac{kN}{mm}$

H = b x f'_c x $(c - \frac{h}{2})$ = 249.038 kN

I = $-(\frac{b \text{ x } c^2}{2}$ x f'_c − b x c x f'_c x $\left(c - \frac{h}{2}\right) + \frac{b \text{ x } c^2 \text{ x } E_2}{3}$ x $\varepsilon_{ccu} - \frac{b \text{ x } c \text{ x } E_2}{2}$ x $\left(c - \frac{h}{2}\right)$ x ε_{ccu})

= 13121 kN.mm

A_{s1} = 204 mm^2	A_{s2} = 0 mm^2	A_{s3} = 0 mm^2	A_{s4} = 204 mm^2
f_{s1} = 333 MPa	f_{s2} = 0 MPa	f_{s3} = 0 MPa	f_{s4} = -333 MPa
d_1 = 73 mm	d_2 = 0 mm	d_3 = 0 mm	d_4 = -73 mm

ØP_n (b) =Ø x (A x $(y_t)^3$+ B x $(y_t)^2$+ C x (y_t) +D+ (A_{s1} x f_{s1} + A_{s2} x f_{s2} + A_{s3} x f_{s3})) = 368 kN

ØM_n (b) =Ø x (E x $(y_t)^4$+ F x $(y_t)^3$+ G x $(y_t)^2$ + H x (y_t) +I+ (A_{s1} x f_{s1} x d_1 + A_{s2} x f_{s2} x d_2 + A_{s3} x f_{s3} x d_3)) = 16 kN.m

Point C (Balance Point)

εf_e = 0.004

$f_l = \frac{(2 \text{x } E_f \text{ x } n \text{ x } t_f \text{ x } \varepsilon f_e)}{D_e}$ = 0.788 MPa

Confinement = $\frac{f_l}{f'_c}$ = 0.03

f’$_{cc}$ = f’$_c$ + ψ_f x 3.3 x ka x f_l = 23.48 MPa

ε_{cuu} = ε'_c x (1.50 + 12 x k_b x $\frac{f_l}{f'_c}$ x $\left(\frac{\varepsilon f_e}{\varepsilon'_c}\right)^{0.45}$) = 0.0037 < 0.01 in

$E_2 = \frac{(f'_{cc} - f'_c)}{\varepsilon_{ccu}}$ = 156.088 MPa

$\varepsilon'_t = \frac{2f'_c}{E_c - E_2}$ = 0.003

$c = d \text{ x } \frac{\varepsilon_{ccu}}{(\varepsilon_{sy} + \varepsilon_{ccu})}$ = 125.045 mm

$y_t = c \text{ x } \frac{\varepsilon'_t}{\varepsilon_{ccu}}$ = 86.24 mm

$A = \frac{-b \text{ x } (E_c - E_2)^2}{12 f'_c} \text{ x } (\frac{\varepsilon_{ccu}}{c})^2 = -1.54 \text{ x } 10^{-4} \frac{kN}{mm^3}$

$B = \frac{b\text{x } (E_c - E_2)}{2} \text{ x } (\frac{\varepsilon_{ccu}}{c})$ = 39.833 MPa

$C = -b \text{ x } f'_c = -3.435 \frac{kN}{mm}$

$D = b \text{ x } c \text{ x } f'_c + \frac{b \text{ x } c \text{ x } E_2}{2} \text{ x } \varepsilon_{ccu}$ = 435 kN

$E = \frac{-b \text{ x } (E_c - E_2)^2}{16\text{x } f'_c} \text{ x } (\frac{\varepsilon_{ccu}}{c})^2 = -1.155 \text{ x } 10^{-4} \frac{kN}{mm^3}$

$F = (b \text{ x } \left(c - \frac{h}{2}\right) \text{x} \frac{(E_c - E_2)^2}{12 f'_c} \text{ x } \left(\frac{\varepsilon_{ccu}}{c}\right)^2 + \frac{b\text{x } (E_c - E_2)}{3} \text{ x } (\frac{\varepsilon_{ccu}}{c}))$ = 28.487 MPa

$G = -(\frac{b \text{ x } f'_c}{2} + b \text{ x} \left(c - \frac{h}{2}\right) \text{x} \frac{(E_c - E_2)}{2} \text{ x} (\frac{\varepsilon_{ccu}}{c})) = -2.22 \frac{kN}{mm}$

$H = b \text{ x } f'_c \text{ x } (c - \frac{h}{2})$ = 43.093 kN

$I = -(\frac{b \text{ x } c^2}{2} \text{x } f'_c - b \text{ x } c \text{ x } f'_c \text{ x} \left(c - \frac{h}{2}\right) + \frac{b \text{ x } c^2 \text{ x } E_2}{3} \text{x } \varepsilon_{ccu} - \frac{b \text{ x } c \text{ x } E_2}{2} \text{x} \left(c - \frac{h}{2}\right) \text{x } \varepsilon_{ccu})$

= 21854 kN.mm

A_{s1} = 204 mm^2	A_{s2} = 0 mm^2	A_{s3} = 0 mm^2	A_{s4} = 204 mm^2
f_{s1} = 333 MPa	f_{s2} = 0 MPa	f_{s3} = 0 MPa	f_{s4} = -333 MPa
d_1 = 73 mm	d_2 = 0 mm	d_3 = 0 mm	d_4 = -73 mm

$ØP_n (c) = Ø \text{ x } (A \text{ x } (y_t)^3 + B \text{ x } (y_t)^2 + C \text{ x } (y_t) + D + (A_{s1} \text{ x } f_{s1} + A_{s2} \text{ x } f_{s2} + A_{s3} \text{ x } f_{s3} + A_{s4} \text{ x } f_{s4}))$
= 219 kN

$ØM_n(c) = Ø \times (E \times (y_t)^4 + F \times (y_t)^3 + G \times (y_t)^2 + H \times (y_t) + I + (A_{s1} \times f_{s1} \times d_1 + A_{s2} \times f_{s2} \times d_2 + A_{s3} \times f_{s3} \times d_3 + A_{s4} \times f_{s4} \times d_4)) = 20$ kN.m

Calculation for Column 10RC1-45

Table A. 3: Geometric and Mechanical Properties

f'_c = 15.29 MPa	εf_u = 0.021
f_y = 391 MPa	E_f = 240 GPa
γ_c = 15 mm	C_E = 0.95
b = 150 mm	$k\varepsilon$ = 0.55
h = 150 mm	n = 1
A_{st} = 328 mm^2	ψ_f = 0.95
ρ_g = 0.0145	E_c = 14663 MPa
Ø = 0.65	d'= 40 mm
ε'_c = 0.002	E_y = 200 GPa
t_f = 0.111 mm	ε_{sy} = 0.00195
f_{fu} = 4900 MPa	

d = h-d'=110 mm

$D_e = \sqrt{b^2 + h^2} = 212.132$ mm

$A_g = b \times h = (2.25 \times 10^4)$ mm^2

$\varepsilon f_e = k\varepsilon \times \varepsilon f_u \times C_E = 0.011$

$$A_e = 1 - \frac{\left(\left(\frac{b}{h}\right) \times (h - 2 \times r_c)^2 + \left(\frac{h}{b}\right) \times (b - 2 \times r_c)^2\right)}{3A_g} - \rho_g = 0.559$$

$A_c = 1 - \rho_g = 0.986$

$\text{Ratio} = \frac{A_e}{A_c} = 0.567$

$k_a = \text{Ratio} \times \left(\frac{b}{h}\right)^2 = 0.567$

$k_b = \text{Ratio} \times \left(\frac{h}{b}\right)^{0.50} = 0.567$

Point A (Uniform/Max Compression)

$f_l = \frac{(2x\ E_f\ x\ n\ x\ t_f\ x\ \varepsilon f_e)}{D_e} = 2.756$ MPa

Confinement $= \frac{f_l}{f_c'} = 0.18$

$f'_{cc} = f'_c + \psi_f$ x 3.3 x ka x $f_l = 20.19$ MPa

$\varepsilon_{cuu} = \varepsilon_c'$ x $(1.50 + 12$ x k_b x $\frac{f_l}{f_c'}$ x $\left(\frac{\varepsilon f_e}{\varepsilon_c'}\right)^{0.45})$ = 0.0083 < 0.01 in

$ØP_n$ (a) = 0.8 Ø x (0.85f'_{cc} x (A_g - A_{st}) + f_y. x A_{st}) = 265 kN

Point B ($\varepsilon_t = 0$; $f_s = 0$)

$\varepsilon f_e = 0.004$ (Minimum)

$f_l = \frac{(2x\ E_f\ x\ n\ x\ t_f\ x\ \varepsilon f_e)}{D_e} = 1.005$ MPa

Confinement $= \frac{f_l}{f_c'} = 0.07$

$f'_{cc} = f'_c + \psi_f$ x 3.3 x ka x $f_l = 17.08$ MPa

$\varepsilon_{cuu} = \varepsilon_c'$ x $(1.50 + 12$ x k_b x $\frac{f_l}{f_c'}$ x $\left(\frac{\varepsilon f_e}{\varepsilon_c'}\right)^{0.45})$ = 0.0042 < 0.01 in

$E_2 = \frac{(f_{cc}' - f_c')}{\varepsilon_{ccu}} = 423.067$ MPa

$\varepsilon'_t = \frac{2f_c'}{E_c - E_2} = 0.002$

c = d = 110 mm

$y_t = c$ x $\frac{\varepsilon_t'}{\varepsilon_{ccu}} = 55.96$ mm

$A = \frac{-b\ x\ (E_c - E_2)^2}{12\ f_c'}$ x $(\frac{\varepsilon_{ccu}}{c})^2 = -2.442$ x $10^{-4}\ \frac{kN}{mm^3}$

$B = \frac{b\ x\ (E_c - E_2)}{2}$ x $(\frac{\varepsilon_{ccu}}{c}) = 40.987$ MPa

$C = -b \text{ x } f'_c = -2.294 \frac{kN}{mm}$

$D = b \text{ x } c \text{ x } f'_c + \frac{b \text{ x } c \text{ x } E_2}{2} \text{ x } \varepsilon_{ccu} = 267 \text{ kN}$

$E = \frac{-b \text{ x } (E_c - E_2)^2}{16 \text{ x } f'_c} \text{ x} (\frac{\varepsilon_{ccu}}{c})^2 = -1.831 \text{ x } 10^{-4} \frac{kN}{mm^3}$

$F = (b \text{ x} \left(c - \frac{h}{2}\right) \text{x} \frac{(E_c - E_2)^2}{12 f'_c} \text{ x } (\frac{\varepsilon_{ccu}}{c})^2 + \frac{b \text{ x } (E_c - E_2)}{3} \text{ x } (\frac{\varepsilon_{ccu}}{c})) = 35.87 \text{ MPa}$

$G = -(\frac{b \text{ x } f'_c}{2} + b \text{ x} \left(c - \frac{h}{2}\right) \text{x} \frac{(E_c - E_2)}{2} \text{ x } (\frac{\varepsilon_{ccu}}{c})) = -2.58 \frac{kN}{mm}$

$H = b \text{ x } f'_c \text{ x } (c - \frac{h}{2}) = 80.273 \text{ kN}$

$I = -(\frac{b \text{ x } c^2}{2} \text{x } f'_c - b \text{ x } c \text{ x } f'_c \text{ x} \left(c - \frac{h}{2}\right) + \frac{b \text{ x } c^2 \text{x } E_2}{3} \text{x } \varepsilon_{ccu} - \frac{b \text{ x } c \text{ x } E_2}{2} \text{x} \left(c - \frac{h}{2}\right) \text{x } \varepsilon_{ccu})$

$= 5611 \text{ kN.mm}$

$A_{s1} = 164 \text{ mm}^2$	$A_{s2} = 0 \text{ mm}^2$	$A_{s3} = 0 \text{ mm}^2$	$A_{s4} = 164 \text{ mm}^2$
$f_{s1} = 391$ MPa	$f_{s2} = 0$ MPa	$f_{s3} = 0$ MPa	$f_{s4} = -391$ MPa
$d_1 = 35$ mm	$d_2 = 0$ mm	$d_3 = 0$ mm	$d_4 = -35$ mm

$ØP_n$ (b) $= Ø \text{ x } (A \text{ x } (y_t)^3 + B \text{ x } (y_t)^2 + C \text{ x } (y_t) + D + (A_{s1} \text{ x } f_{s1} + A_{s2} \text{ x } f_{s2} + A_{s3} \text{ x } f_{s3})) = 187$ kN

$ØM_n$ (b) $= Ø \text{ x } (E \text{ x } (y_t)^4 + F \text{ x } (y_t)^3 + G \text{ x } (y_t)^2 + H \text{ x } (y_t) + I + (A_{s1} \text{ x } f_{s1} \text{ x } d_1 + A_{s2} \text{ x } f_{s2} \text{ x } d_2 + A_{s3} \text{ x } f_{s3} \text{ x } d_3)) = 6$ kN.m

Point C (Balance Point)

$\varepsilon f_e = 0.004$

$f_l = \frac{(2 \text{x } E_f \text{ x } n \text{ x } t_f \text{ x } \varepsilon f_e)}{D_e} = 1.005$ MPa

Confinement $= \frac{f_l}{f'_c} = 0.07$

$f'_{cc} = f'_c + \psi_f \text{ x } 3.3 \text{ x } ka \text{ x } f_l = 17.08$ MPa

$\varepsilon_{cuu} = \varepsilon'_c \text{ x } (1.50 + 12 \text{ x } k_b \text{ x } \frac{f_l}{f'_c} \text{ x} \left(\frac{\varepsilon f_e}{\varepsilon'_c}\right)^{0.45}) = 0.0042 < 0.01$ in

$E_2 = \frac{(f'_{cc} - f'_c)}{\varepsilon_{ccu}} = 423.067$ MPa

$\varepsilon'_t = \frac{2f'_c}{E_c - E_2} = 0.002$

$c = d \text{ x } \frac{\varepsilon_{ccu}}{(\varepsilon_{sy} + \varepsilon_{ccu})} = 75.244$ mm

$y_t = c \text{ x } \frac{\varepsilon'_t}{\varepsilon_{ccu}} = 38.28$ mm

$A = \frac{-b \text{ x } (E_c - E_2)^2}{12 f'_c} \text{ x } (\frac{\varepsilon_{ccu}}{c})^2 = -5.218 \text{ x } 10^{-4} \frac{\text{kN}}{\text{mm}^3}$

$B = \frac{b\text{x } (E_c - E_2)}{2} \text{ x } (\frac{\varepsilon_{ccu}}{c}) = 59.92$ MPa

$C = -b \text{ x } f'_c = -2.294 \frac{\text{kN}}{\text{mm}}$

$D = b \text{ x } c \text{ x } f'_c + \frac{b \text{ x } c \text{ x } E_2}{2} \text{ x } \varepsilon_{ccu} = 183$ kN

$E = \frac{-b \text{ x } (E_c - E_2)^2}{16\text{x } f'_c} \text{ x } (\frac{\varepsilon_{ccu}}{c})^2 = -3.914 \text{ x } 10^{-4} \frac{\text{kN}}{\text{mm}^3}$

$F = (b \text{ x } \left(c - \frac{h}{2}\right) \text{x} \frac{(E_c - E_2)^2}{12 f'_c} \text{ x } \left(\frac{\varepsilon_{ccu}}{c}\right)^2 + \frac{b\text{x } (E_c - E_2)}{3} \text{ x } (\frac{\varepsilon_{ccu}}{c})) = 40.074$ MPa

$G = -(\frac{b \text{ x } f'_c}{2} + b \text{ x} \left(c - \frac{h}{2}\right) \text{x} \frac{(E_c - E_2)}{2} \text{ x} (\frac{\varepsilon_{ccu}}{c})) = -1.16 \frac{\text{kN}}{\text{mm}}$

$H = b \text{ x } f'_c \text{ x } (c - \frac{h}{2}) = 0.559$ kN

$I = -(\frac{b \text{ x } c^2}{2} \text{x } f'_c - b \text{ x } c \text{ x } f'_c \text{ x} \left(c - \frac{h}{2}\right) + \frac{b \text{ x } c^2 \text{ x } E_2}{3} \text{x } \varepsilon_{ccu} - \frac{b \text{ x } c \text{ x } E_2}{2} \text{x} \left(c - \frac{h}{2}\right) \text{x } \varepsilon_{ccu})$

$= 6954$ kN.mm

$A_{s1} = 164$ mm^2	$A_{s2} = 0$ mm^2	$A_{s3} = 0$ mm^2	$A_{s4} = 164$ mm^2
$f_{s1} = 391$ MPa	$f_{s2} = 0$ MPa	$f_{s3} = 0$ MPa	$f_{s4} = -391$ MPa
$d_1 = 35$ mm	$d_2 = 0$ mm	$d_3 = 0$ mm	$d_4 = -35$ mm

$ØP_n(c) = Ø \text{ x } (A \text{ x } (y_t)^3 + B \text{ x } (y_t)^2 + C \text{ x } (y_t) + D + (A_{s1} \text{ x } f_{s1} + A_{s2} \text{ x } f_{s2} + A_{s3} \text{ x } f_{s3} + A_{s4} \text{ x } f_{s4}))$
$= 100$ kN

$ØM_n(c) = Ø \times (E \times (y_t)^4 + F \times (y_t)^3 + G \times (y_t)^2 + H \times (y_t) + I + (A_{s1} \times f_{s1} \times d_1 + A_{s2} \times f_{s2} \times d_2 + A_{s3} \times f_{s3} \times d_3 + A_{s4} \times f_{s4} \times d_4)) = 7$ kN.m

Calculation for Column 10RC2-90

Table A. 4: Geometric and Mechanical Properties

$f'_c = 15.29$ MPa	$\varepsilon f_u = 0.021$
$f_y = 333$ MPa	$E_f = 240$ GPa
$\gamma_c = 15$ mm	$C_E = 0.95$
$b = 150$ mm	$k\varepsilon = 0.55$
$h = 225$ mm	$n = 1$
$A_{st} = 408$ mm^2	$\psi_f = 0.95$
$\rho_g = 0.012$	$E_c = 14663$ MPa
$Ø = 0.65$	$d' = 40$ mm
$\varepsilon'_c = 0.002$	$E_y = 186$ GPa
$t_f = 0.111$ mm	$\varepsilon_{sy} = 0.00179$
$f_{fu} = 4900$ MPa	

$d = h - d' = 185$ mm

$D_e = \sqrt{b^2 + h^2} = 270.416$ mm

$A_g = b \times h = (3.375 \times 10^4)$ mm^2

$\varepsilon f_e = k\varepsilon \times \varepsilon f_u \times C_E = 0.011$

$$A_e = 1 - \frac{\left(\left(\frac{b}{h}\right) \times (h - 2 \times r_c)^2 + \left(\frac{h}{b}\right) \times (b - 2 \times r_c)^2\right)}{3A_g} - \rho_g = 0.524$$

$A_c = 1 - \rho_g = 0.988$

$\text{Ratio} = \frac{A_e}{A_c} = 0.531$

$k_a = \text{Ratio} \times \left(\frac{b}{h}\right)^2 = 0.236$

$k_b = \text{Ratio} \times \left(\frac{h}{b}\right)^{0.50} = 0.65$

Point A (Uniform/Max Compression)

$f_l = \frac{(2x\ E_f\ x\ n\ x\ t_f\ x\ \varepsilon f_e)}{D_e} = 2.162$ MPa

Confinement $= \frac{f_l}{f'_c} = 0.14$

$f'_{cc} = f'_c + \psi_f$ x 3.3 x ka x $f_l = 16.89$ MPa

$\varepsilon_{cuu} = \varepsilon'_c \text{ x } (1.50 + 12 \text{ x } k_b \text{ x } \frac{f_l}{f'_c} \text{ x } \left(\frac{\varepsilon f_e}{\varepsilon'_c}\right)^{0.45}) = 0.0077 < 0.01$ in

$\text{Ø}P_n$ (a) = 0.8 Ø x (0.85f'_{cc} x (A_g - A_{st}) + f_y. x A_{st}) = 320 kN

Point B ($\varepsilon_t = 0$; $f_s = 0$)

$\varepsilon f_e = 0.004$ (Minimum)

$f_l = \frac{(2x\ E_f\ x\ n\ x\ t_f\ x\ \varepsilon f_e)}{D_e} = 0.788$ MPa

Confinement $= \frac{f_l}{f'_c} = 0.05$

$f'_{cc} = f'_c + \psi_f$ x 3.3 x k_a x $f_l = 15.87$ MPa

$\varepsilon_{cuu} = \varepsilon'_c \text{ x } (1.50 + 12 \text{ x } k_b \text{ x } \frac{f_l}{f'_c} \text{ x } \left(\frac{\varepsilon f_e}{\varepsilon'_c}\right)^{0.45}) = 0.0041 < 0.01$ in

$E_2 = \frac{(f'_{cc} - f'_c)}{\varepsilon_{ccu}} = 142.188$ MPa

$\varepsilon'_t = \frac{2f'_c}{E_c - E_2} = 0.002$

c = d = 185 mm

$y_t = c \text{ x } \frac{\varepsilon'_t}{\varepsilon_{ccu}} = 95.06$ mm

$A = \frac{-b \text{ x } (E_c - E_2)^2}{12\ f'_c} \text{ x } (\frac{\varepsilon_{ccu}}{c})^2 = -8.46 \text{ x } 10^{-5} \frac{kN}{mm^3}$

$B = \frac{b \text{ x } (E_c - E_2)}{2} \text{ x } (\frac{\varepsilon_{ccu}}{c}) = 24.126$ MPa

$C = -b \times f'_c = -2.294 \frac{kN}{mm}$

$D = b \times c \times f'_c + \frac{b \times c \times E_2}{2} \times \varepsilon_{ccu} = 432$ kN

$E = \frac{-b \times (E_c - E_2)^2}{16 \times f'_c} \times (\frac{\varepsilon_{ccu}}{c})^2 = -6.345 \times 10^{-5} \frac{kN}{mm^3}$

$F = (b \times \left(c - \frac{h}{2}\right) \times \frac{(E_c - E_2)^2}{12 f'_c} \times (\frac{\varepsilon_{ccu}}{c})^2 + \frac{b \times (E_c - E_2)}{3} \times (\frac{\varepsilon_{ccu}}{c})) = 22.217$ MPa

$G = -(\frac{b \times f'_c}{2} + b \times \left(c - \frac{h}{2}\right) \times \frac{(E_c - E_2)}{2} \times (\frac{\varepsilon_{ccu}}{c})) = -2.9 \frac{kN}{mm}$

$H = b \times f'_c \times (c - \frac{h}{2}) = 166.279$ kN

$I = -(\frac{b \times c^2}{2} \times f'_c - b \times c \times f'_c \times \left(c - \frac{h}{2}\right) + \frac{b \times c^2 \times E_2}{3} \times \varepsilon_{ccu} - \frac{b \times c \times E_2}{2} \times \left(c - \frac{h}{2}\right) \times \varepsilon_{ccu})$

$= 8897$ kN.mm

$A_{s1} = 204$ mm^2	$A_{s2} = 0$ mm^2	$A_{s3} = 0$ mm^2	$A_{s4} = 204$ mm^2
$f_{s1} = 333$ MPa	$f_{s2} = 0$ MPa	$f_{s3} = 0$ MPa	$f_{s4} = -333$ MPa
$d_1 = 75$ mm	$d_2 = 0$ mm	$d_3 = 0$ mm	$d_4 = -73$ mm

$ØP_n (b) = Ø \times (A \times (y_t)^3 + B \times (y_t)^2 + C \times (y_t) + D + (A_{s1} \times f_{s1} + A_{s2} \times f_{s2} + A_{s3} \times f_{s3})) = 278$ kN

$ØM_n (b) = Ø \times (E \times (y_t)^4 + F \times (y_t)^3 + G \times (y_t)^2 + H \times (y_t) + I + (A_{s1} \times f_{s1} \times d_1 + A_{s2} \times f_{s2} \times d_2 + A_{s3} \times f_{s3} \times d_3)) = 11$ kN.m

Point C (Balance Point)

$\varepsilon f_e = 0.004$

$f_l = \frac{(2 \times E_f \times n \times t_f \times \varepsilon f_e)}{D_e} = 0.788$ MPa

Confinement $= \frac{f_l}{f'_c} = 0.05$

$f'_{cc} = f'_c + \psi_f \times 3.3 \times ka \times f_l = 15.87$ MPa

$\varepsilon_{cuu} = \varepsilon'_c \times (1.50 + 12 \times k_b \times \frac{f_l}{f'_c} \times \left(\frac{\varepsilon f_e}{\varepsilon'_c}\right)^{0.45}) = 0.0041 < 0.01$ in

$E_2 = \frac{(f'_{cc} - f'_c)}{\varepsilon_{ccu}} = 142.188$ MPa

$\varepsilon'_t = \frac{2f'_c}{E_c - E_2} = 0.002$

$c = d \times \frac{\varepsilon_{ccu}}{(\varepsilon_{sy} + \varepsilon_{ccu})} = 128.761$ mm

$y_t = c \times \frac{\varepsilon'_t}{\varepsilon_{ccu}} = 66.16$ mm

$A = \frac{-b \times (E_c - E_2)^2}{12\, f'_c} \times (\frac{\varepsilon_{ccu}}{c})^2 = -1.746 \times 10^{-4}\ \frac{kN}{mm^3}$

$B = \frac{b\times (E_c - E_2)}{2} \times (\frac{\varepsilon_{ccu}}{c}) = 34.663$ MPa

$C = -b \times f'_c = -2.294\ \frac{kN}{mm}$

$D = b \times c \times f'_c + \frac{b \times c \times E_2}{2} \times \varepsilon_{ccu} = 301$ kN

$E = \frac{-b \times (E_c - E_2)^2}{16 \times f'_c} \times (\frac{\varepsilon_{ccu}}{c})^2 = -1.31 \times 10^{-4}\ \frac{kN}{mm^3}$

$F = (b \times \left(c - \frac{h}{2}\right) \times \frac{(E_c - E_2)^2}{12\, f'_c} \times \left(\frac{\varepsilon_{ccu}}{c}\right)^2 + \frac{b\times (E_c - E_2)}{3} \times (\frac{\varepsilon_{ccu}}{c})) = 25.949$ MPa

$G = -(\frac{b \times f'_c}{2} + b \times \left(c - \frac{h}{2}\right) \times \frac{(E_c - E_2)}{2} \times (\frac{\varepsilon_{ccu}}{c})) = -1.71\ \frac{kN}{mm}$

$H = b \times f'_c \times (c - \frac{h}{2}) = 37.296$ kN

$I = -(\frac{b \times c^2}{2} \times f'_c - b \times c \times f'_c \times \left(c - \frac{h}{2}\right) + \frac{b \times c^2 \times E_2}{3} \times \varepsilon_{ccu} - \frac{b \times c \times E_2}{2} \times \left(c - \frac{h}{2}\right) \times \varepsilon_{ccu})$

$= 14602$ kN.mm

$A_{s1} = 204\ mm^2$	$A_{s2} = 0\ mm^2$	$A_{s3} = 0\ mm^2$	$A_{s4} = 204\ mm^2$
$f_{s1} = 333$ MPa	$f_{s2} = 0$ MPa	$f_{s3} = 0$ MPa	$f_{s4} = -333$ MPa
$d_1 = 73$ mm	$d_2 = 0$ mm	$d_3 = 0$ mm	$d_4 = -73$ mm

$ØP_n(c) = Ø \times (A \times (y_t)^3 + B \times (y_t)^2 + C \times (y_t) + D + (A_{s1} \times f_{s1} + A_{s2} \times f_{s2} + A_{s3} \times f_{s3} + A_{s4} \times f_{s4}))$
$= 163$ kN

$\emptyset M_n(c) = \emptyset \times (E \times (y_t)^4 + F \times (y_t)^3 + G \times (y_t)^2 + H \times (y_t) + I + (A_{s1} \times f_{s1} \times d_1 + A_{s2} \times f_{s2} \times d_2 + A_{s3} \times f_{s3} \times d_3 + A_{s4} \times f_{s4} \times d_4)) = 16$ kN.m

Calculation for column 17RW1-45

Table A. 5: Geometric and Mechanical Properties

$b = 150$ mm	$E_c = 17945$ MPa
$h = 150$ mm	$\varepsilon_u = 0.003$
$Ag_t = 22500$ mm^2	$E_y = 200000$ MPa
$A_{st} = 328$ mm^2	$\varepsilon_{sy} = 0.001955$
$\rho_g = 0.0145$	$\beta_1 = 0.85$
$f'_c = 22.9$ MPa	Axial compression, (a) = 0.80
$f_y = 391$ MPa	Tension controlled ϕ, (b) = 0.90
d'= 40 mm	Compression controlled ϕ, (c) = 0.65

Table A. 6: Factored loads and moments with corresponding capacities

No	P_u	M_{ux}	ϕM_{nx}	$\phi M_n/M_u$	NA Depth	d_t Depth	ε_t	ϕ	
	kN	kNm	kNm		mm	mm			
1	249.00	12.16	5.19	0.427	128	111	-0.00041	0.650	#

Section capacity exceeded. Revise design!

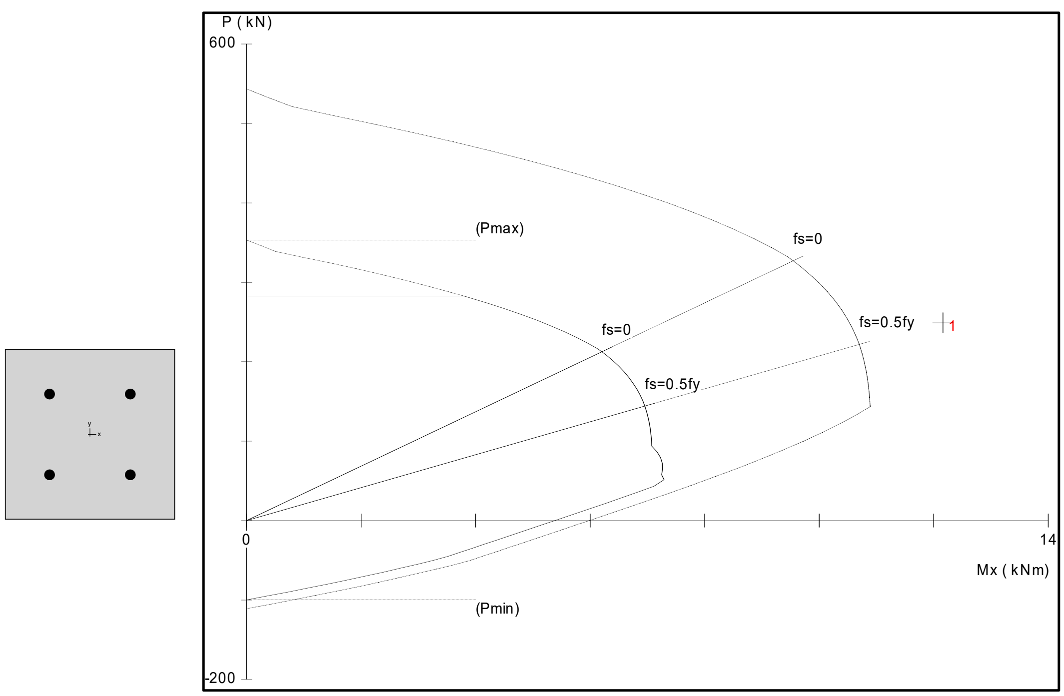

Fig. A.1: Interaction diagram for 150 x 150 column 17RW1-45.

Calculation for column 17RW2-90

Table A. 7: Geometric and Mechanical Properties

b = 150 mm	E_c = 17945 MPa
h = 225 mm	ε_u = 0.003
Ag_t = 33750 mm^2	E_y = 186000 MPa
A_{st} = 408 mm^2	ε_{sy} = 0.00179
ρ_g = 0.012	β_1 = 0.85
f'_c = 22.9 MPa	Axial compression, (a) = 0.80
f_y = 333 MPa	Tension controlled ϕ, (b) = 0.90
d'= 40 mm	Compression controlled ϕ, (c) = 0.65

Table A. 8: Factored loads and moments with corresponding capacities

No	P_u	M_{ux}	ϕM_{nx}	$\phi M_n/M_u$	NA Depth	d_t Depth	ε_t	ϕ	
	kN	kNm	kNm		mm	mm			
1	291.00	27.44	16.47	0.600	158	184	0.00051	0.650	#

Section capacity exceeded. Revise design!

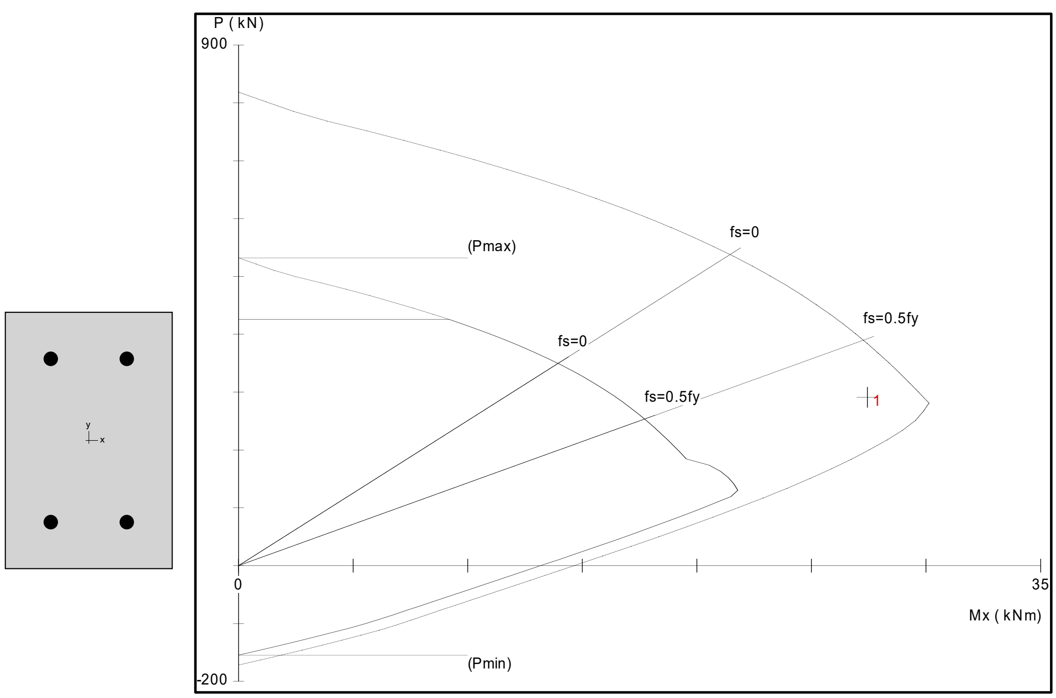

Fig. A.2: Interaction diagram for 150 x 225 mm column 17RW2-90.

Calculation for column 10RW1-45

Table A. 9: Geometric and Mechanical Properties

$b = 150$ mm	$E_c = 14663$ MPa
$h = 150$ mm	$\varepsilon_u = 0.003$
$Ag_t = 22500$ mm^2	$E_y = 200000$ MPa
$A_{st} = 328$ mm^2	$\varepsilon_{sy} = 0.001955$
$\rho_g = 0.0145$	$\beta_1 = 0.85$
$f'_c = 15.29$ MPa	Axial compression, (a) = 0.80
$f_y = 391$ MPa	Tension controlled ϕ, (b) = 0.90
$d' = 40$ mm	Compression controlled ϕ, (c) = 0.65

Table A. 10: Factored loads and moments with corresponding capacities

No	P_u	M_{ux}	ϕM_{nx}	$\phi M_n/M_u$	NA Depth	d_t Depth	ε_t	ϕ	
	kN	kNm	kNm		mm	mm			
1	194.00	9.67	3.30	0.341	139	111	-0.00060	0.650	#

Section capacity exceeded. Revise design!

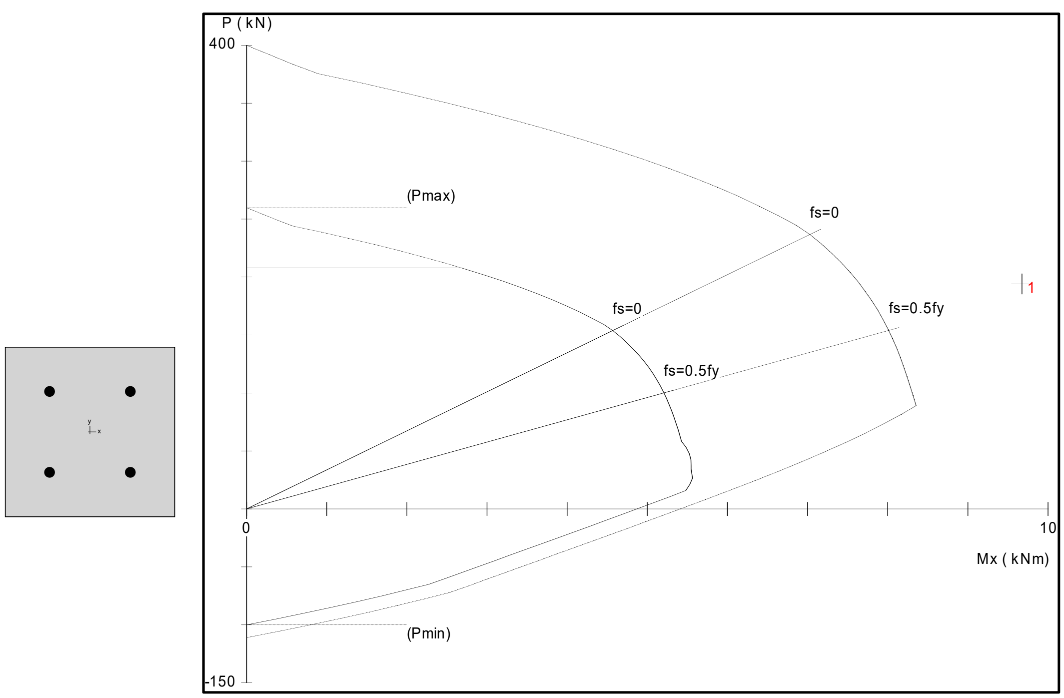

Fig. A.3: Interaction diagram for 150 x 150 mm column 10RW1-45.

Calculation for column 10RW2-90

Table A. 11: Geometric and Mechanical Properties

b = 150 mm	E_c = 14663 MPa
h = 225 mm	ε_u = 0.003
Ag_t = 33750 mm^2	E_y = 186000 MPa
A_{st} = 408 mm^2	ε_{sy} = 0.00179
ρ_g = 0.012	β_1 = 0.85
f'_c = 15.29 MPa	Axial compression, (a) = 0.80
f_y = 333 MPa	Tension controlled ϕ, (b) = 0.90
d'= 40 mm	Compression controlled ϕ, (c) = 0.65

Table A. 12: Factored loads and moments with corresponding capacities

No	P_u	M_{ux}	ϕM_{nx}	$\phi M_n/M_u$	NA Depth	d_t Depth	ε_t	ϕ	
	kN	kNm	kNm		mm	mm			
1	256.00	23.69	10.42	0.440	187	184	-0.00004	0.650	#

Section capacity exceeded. Revise design!

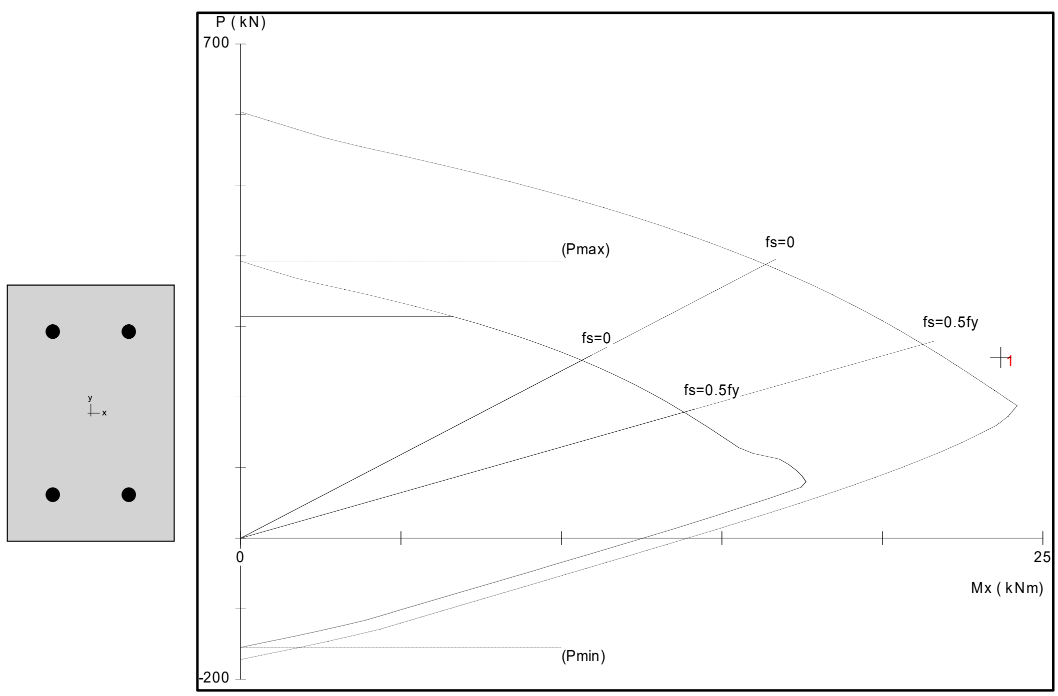

Fig. A.4: Interaction diagram for 150 x 225 mm column 10RW2-90.

APPENDIX B
CONCRETE MIX DESIGN

Mix Design by ACI 211.1-91 (1991) Method for 1 m^3 of Concrete

Specified compressive strength of concrete (f'_c) is 10 MPa.

Table B. 1: Physical properties of aggregates and cement

Variables	Unit	FA	CA	Cement
Fineness modulus	-	2.16	6.99	-
Apparent specific gravity	-	2.75	2.47	2.95
Bulk specific gravity (SSD)	-	2.66	2.01	-
Bulk specific gravity (OD)	-	2.62	1.69	-
Absorption capacity (%D)	%	1.80	18.68	-
Loose condition unit weight (SSD)	kg/m^3	1521	1093	-
Compact condition unit weight (SSD)	kg/m^3	1607	1262	-
Loose condition % of voids	%	39	46	-
Compact condition % of voids	%	36	37	-
L.A. abrasion value	%	-	45	-

Step 1: The desired slump is 25 mm to 50 mm.

Step 2: Nominal maximum sizes of aggregates is 19 mm.

Table B. 2: Approximate mixing water and air content requirements for different slumps and nominal maximum sizes of aggregates

Slump, mm	Water, Kg/m^3 of concrete for indicated nominal maximum sizes of aggregate							
	9.5	12.5	19	25	37.5	50	75	150
Non-air-entrained concrete								
25 to 50	207	199	190	179	166	154	130	113
75 to 100	228	216	205	193	181	169	145	124
150 to 175	243	228	216	202	190	178	160	-
Approximate amount of entrapped air in non-air-entrained concrete, percent	3	2.5	2	1.5	1	0.5	0.3	0.2

Source: Table A1.5.3.3 of ACI 211.1-91 (1991) standard.

Step 3: Since the proposed specimen will be used for experimental study and will not be exposed to severe weathering, non-air-entrained concrete will be used. The approximate amount of mixing water to produce 25 mm to 50 mm slump in non-air-entrained concrete with maximum size of aggregate (19 mm) is found from Table A1.5.3.3 of ACI 211.1-91 (1991) standard to be 190 kg/m^3. Estimated entrapped air is shown as 2 percent.

Step 4: Required average compressive strength of concrete used as the basis for selection of concrete proportions ($f'_{cr} = f'_c + 7$ MPa i.e 17 MPa). From Table A1.5.3.4(a) of ACI 211.1-91 (1991) standard, the water-cement ratio needed to produce a strength of 17 MPa in non-air-entrained concrete is found to be about 0.75 but selected Water-Cement ratio (W/C) is 0.65.

Table B. 3: Relationships between water-cement ratio and compressive strength of concrete

Compressive strength At 28 days, MPa	Water-cement ratio, by mass	
	Non-air-entrained concrete	Air-entrained concrete
40	0.42	–
35	0.47	0.39
30	0.54	0.45
25	0.61	0.52
20	0.69	0.60
15	0.79	0.70

Source: Table A1.5.3.4(a) of ACI 211.1-91 (1991) standard.

Step 5: From the information derived in Steps 3 and 4, the required cement content is found to be 190/0.65 = 292 kg/m^3.

Step 6: The quantity of coarse aggregate is estimated from Table A1.5.3.6 of ACI 211.1-91 (1991) standard. For a fine aggregate having a fineness modulus of 2.16 and a 19 mm nominal maximum size of coarse aggregate, the table indicates that 0.683 m^3 of coarse aggregate, on a dry-rodded basis, may be used in each m^3 of concrete. Since it weighs 1262 kg/m^3, the dry weight of coarse aggregate is 0.683 x 1262 = 862 kg/m^3.

Table B. 4: Volume of coarse aggregate per unit of volume of Concrete

Nominal maximum size of aggregate, mm	Volume of dry-rodded coarse aggregate per unit volume of concrete for different fineness moduli of fine aggregate			
	2.40	2.60	2.80	3.00
9.5	0.50	0.48	0.46	0.44
12.5	0.59	0.57	0.55	0.53
19	0.66	0.64	0.62	0.60
25	0.71	0.69	0.67	0.65
37.5	0.75	0.73	0.71	0.69
50	0.78	0.76	0.74	0.72
75	0.82	0.80	0.78	0.76
150	0.87	0.85	0.83	0.81

Source: Table A1.5.3.6 of ACI 211.1-91 (1991) standard.

Step 7: Determination of fine aggregate on the basis of absolute volume method:

Variables	Calculation	Value	Unit
Volume of water	190 / 1000	0.190	m^3
Solid volume of cement	292 / (2.95x1000)	0.099	m^3
Solid volume of coarse aggregate	862 / (2.01x1000)	0.429	m^3
Volume of entrapped air	0.02 x 1	0.020	m^3
Total solid volume of ingredients except fine aggregate	-	0.738	m^3

Solid volume of fine aggregate required = 1 – 0.738 = 0.262 m^3

Required weight of dry fine aggregate = 0.262 x 2.66 x 1000 = 697 kg/ m^3.

Table B. 5: Summary of the ingredients for mix proportion of 1 m^3 concrete

W/C Ratio	Water (kg)	Cement (kg)	Coarse Aggregate (kg)	Fine aggregate (kg)	Fresh Density (kg/m^3)	Slump (mm)
0.65	190	292	862	697	2085	115

APPENDIX C
FAILURE MODE OF THE COLUMNS

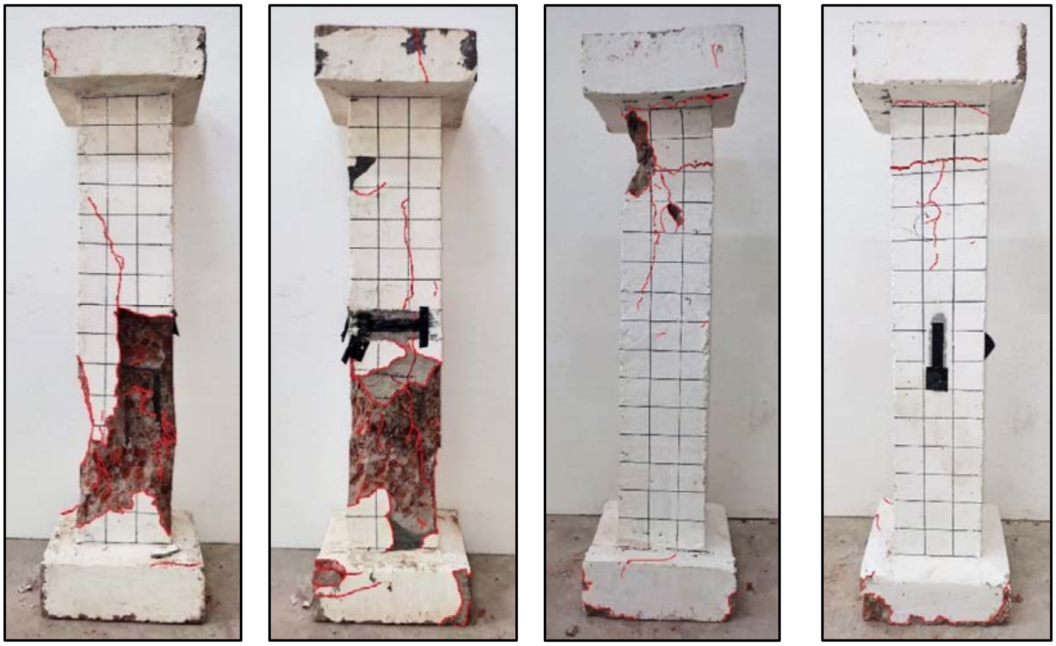

Back Left Back Left

(a) 17RW1-00 (b) 17RW1-45

Back Left Back Left

(c) 17RD1-45 (d) 17RC1-45

Fig. C.1: Failure modes of the concentrically and eccentrically loaded of 150 mm x 150 mm x 950 mm columns with 17 MPa strength.

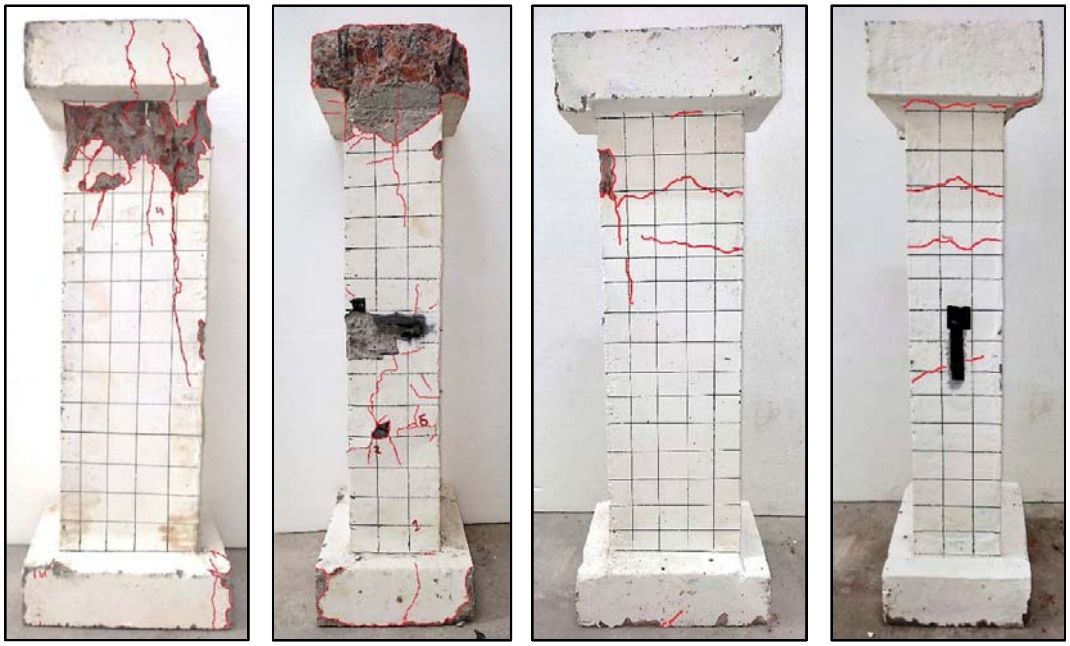

Back Left Back Left

(a) 17RW2-00 (b) 17RW2-90

Back Left Back Left

(c) 17RD2-90 (d) 17RC2-90

Fig. C.2: Failure modes of the concentrically and eccentrically loaded of 150 mm x 225 mm x 950 mm columns with 17 MPa strength.

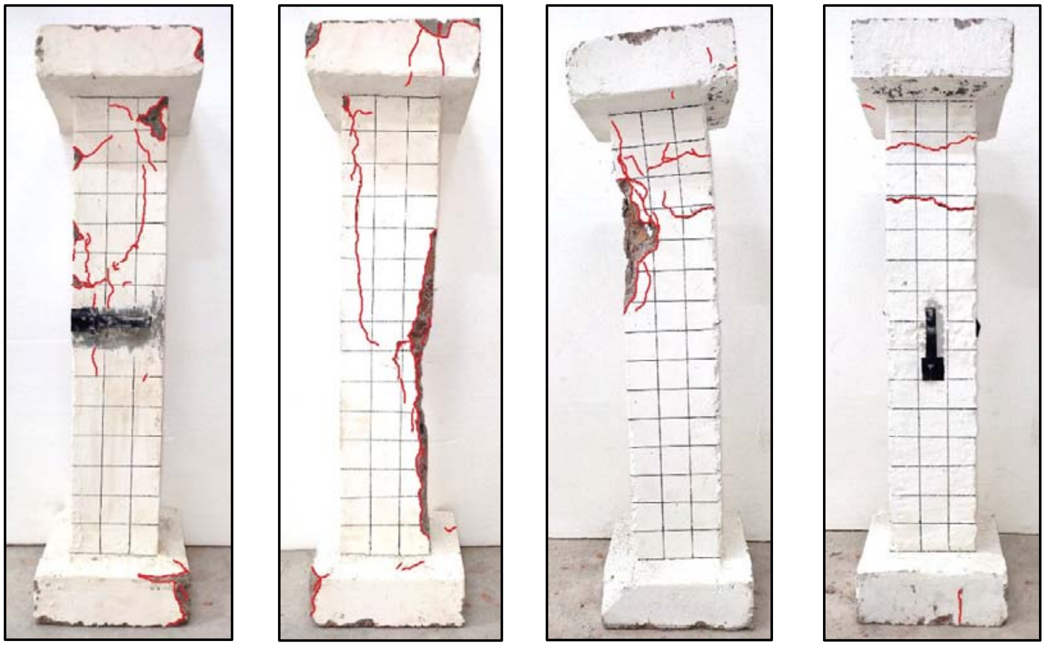

Back Left Back Left

(a) 10RW1-00 (b) 10RW1-45

Back Left Back Left

(c) 10RD1-45 (d) 10RC1-45

Fig. C.3: Failure modes of the concentrically and eccentrically loaded of 150 mm x 150 mm x 950 mm columns with 10 MPa strength.

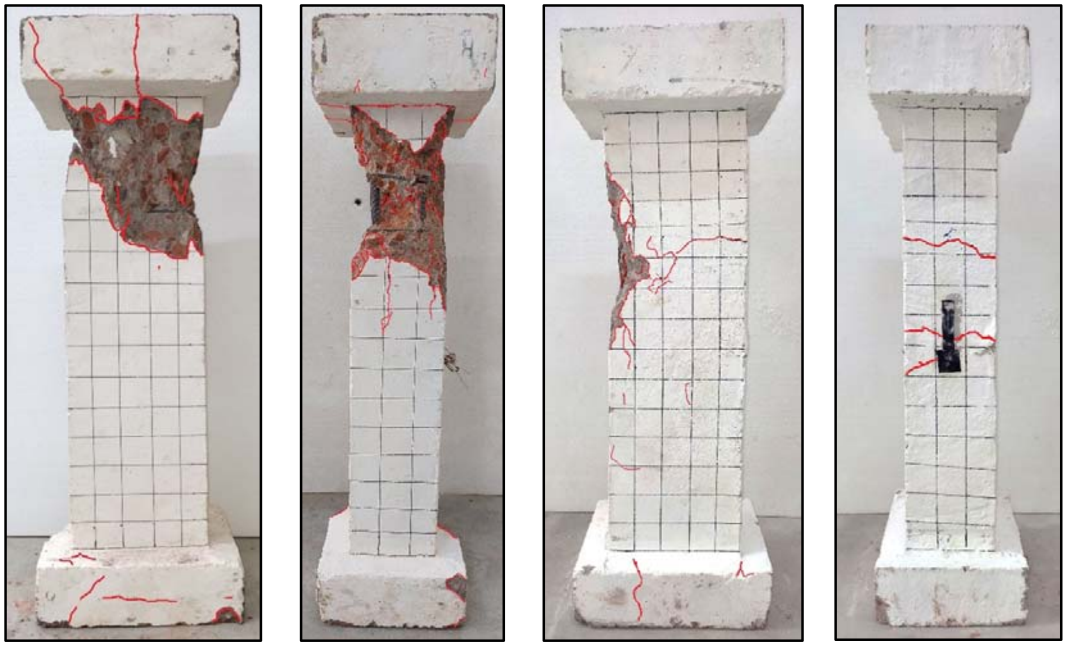

Back Left Back Left

(a) 10RW2-00 (b) 10RW2-90

Back Left Back Left

(c) 10RD2-90 (d) 10RC2-90

Fig. C.4: Failure modes of the concentrically and eccentrically loaded of 150 mm x 225 mm x 950 mm columns with 10 MPa strength.

APPENDIX D
LATERAL DEFORMATION OF THE COLUMNS

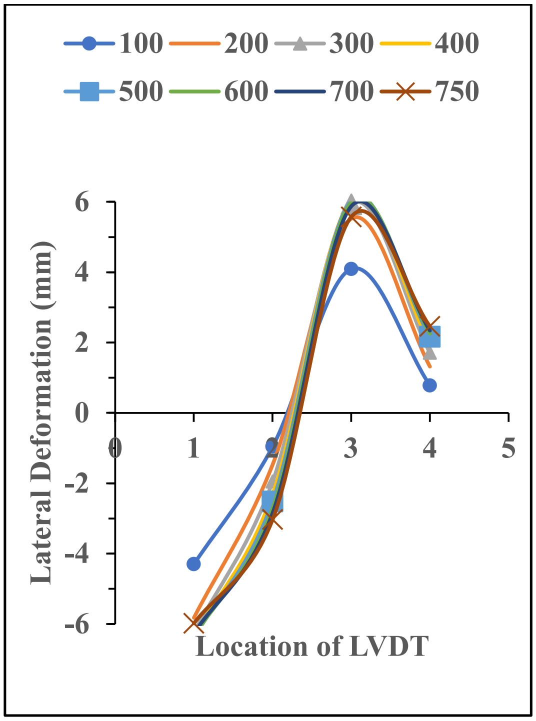

(a) 17RW1-00

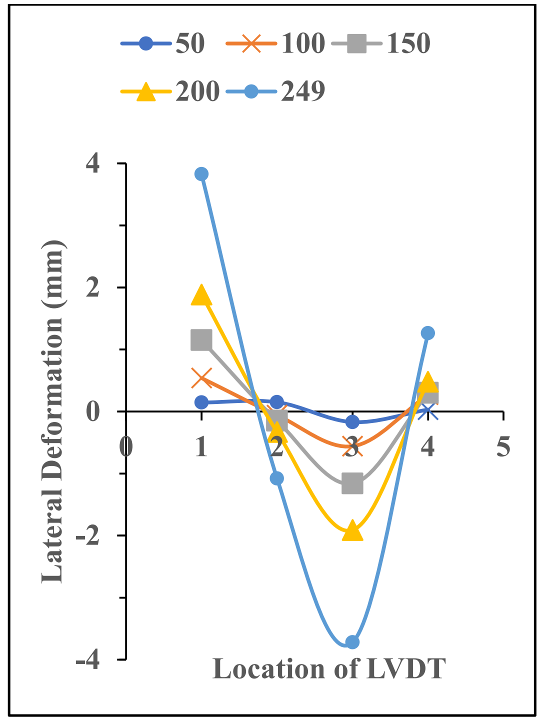

(b) 17RW1-45

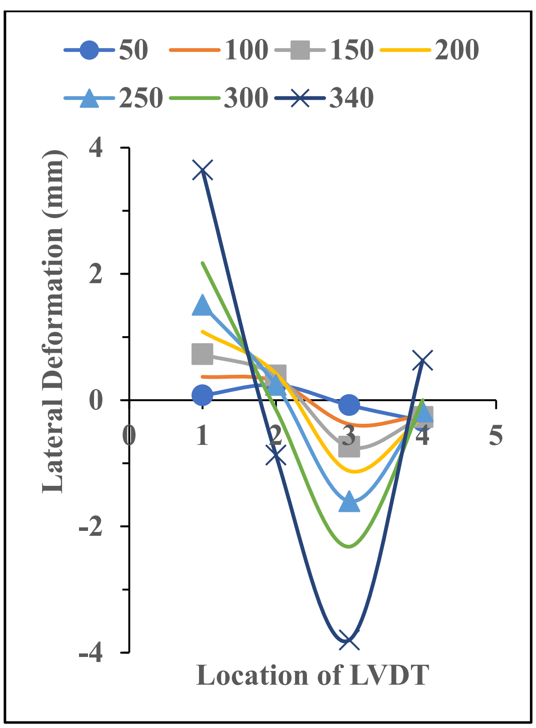

(c) 17RD1-45

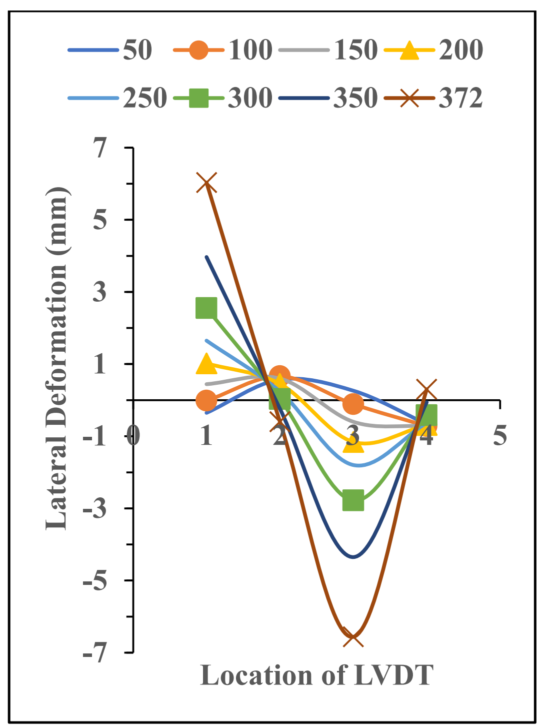

(d) 17RC1-45

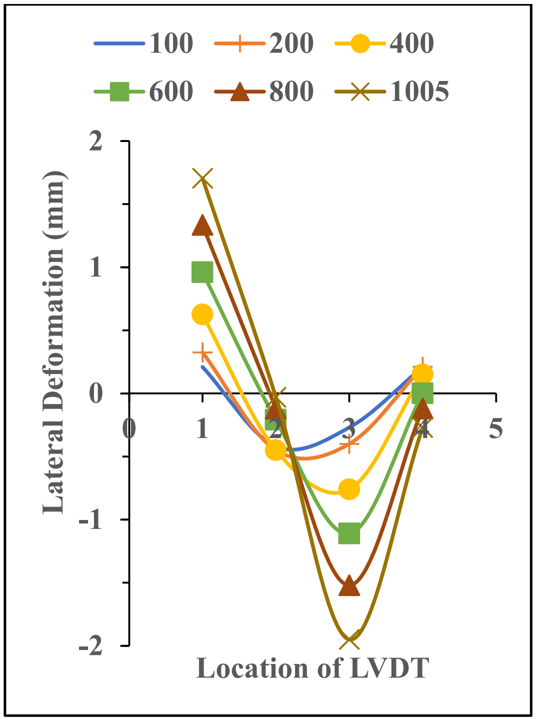

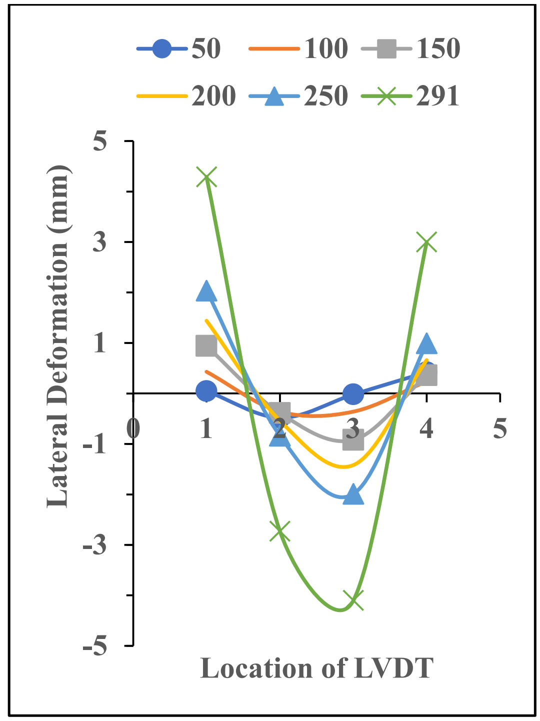

(e) 17RW2-00

(f) 17RW2-90

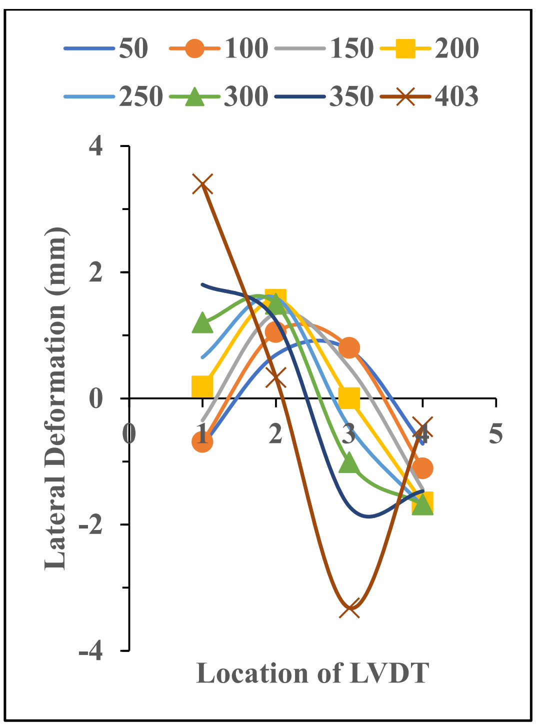

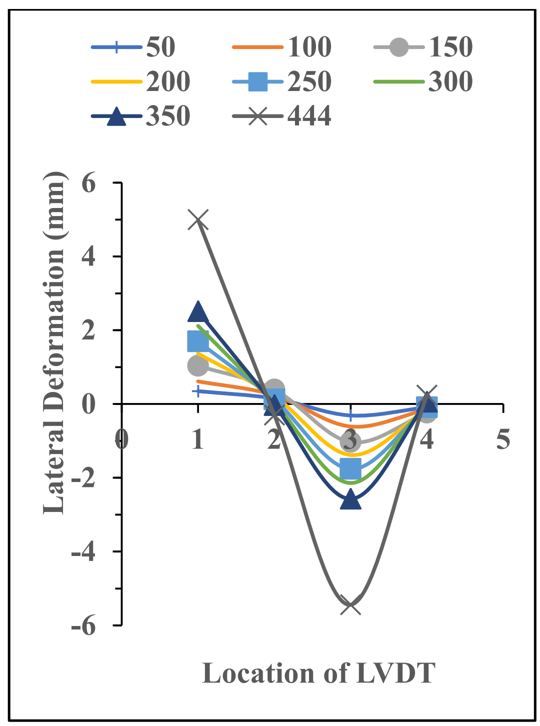

(g) 17RD2-90

(h) 17RC2-90

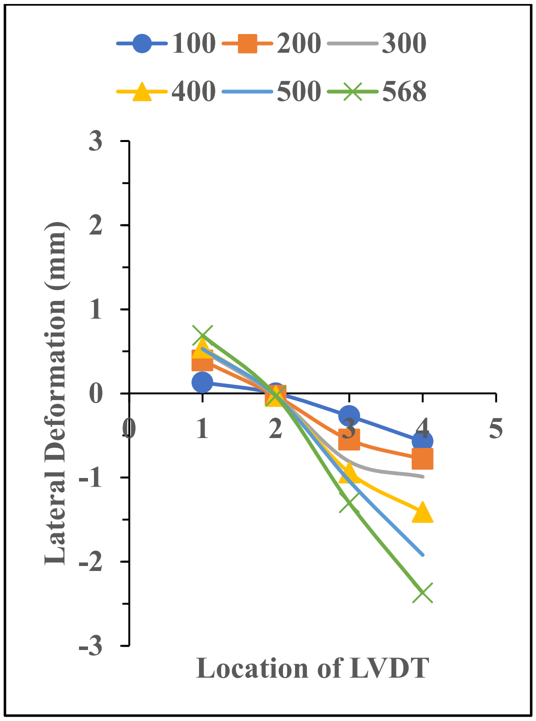

(i) 10RW1-00

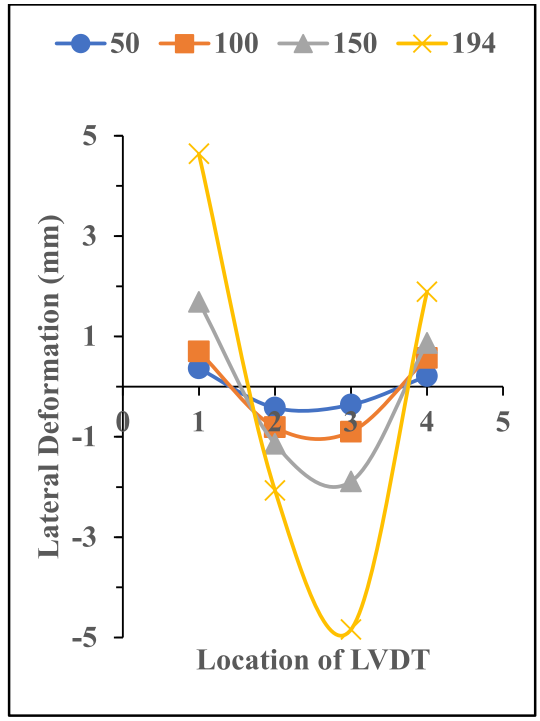

(j) 10RW1-45

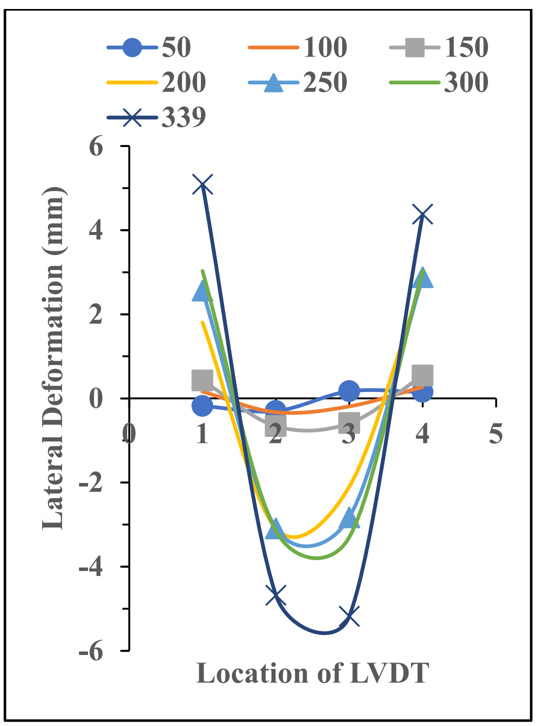

(k) 10RD1-45

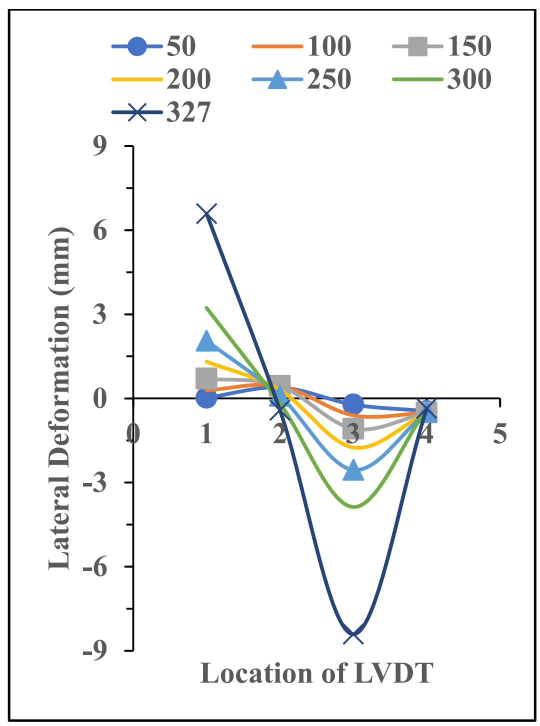

(l) 10RC1-45

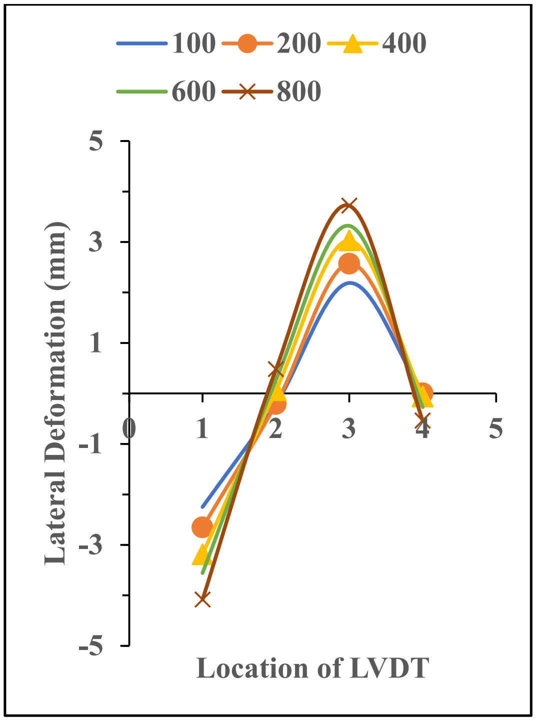

(m)10RW2-00

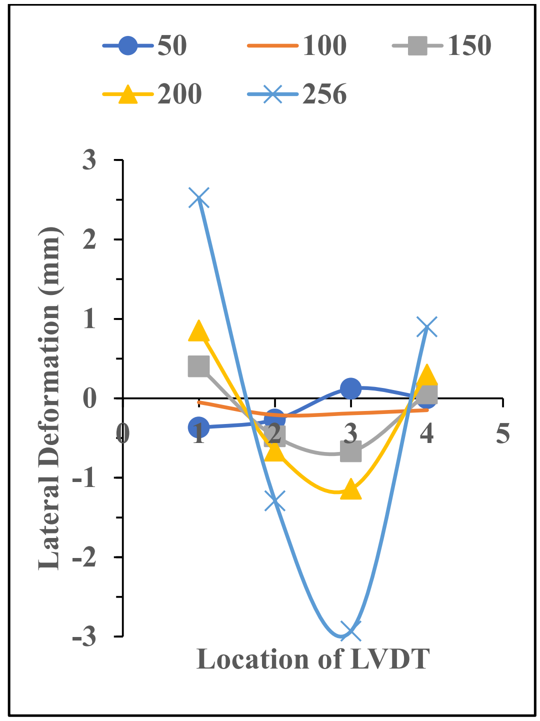

(n) 10RW2-90

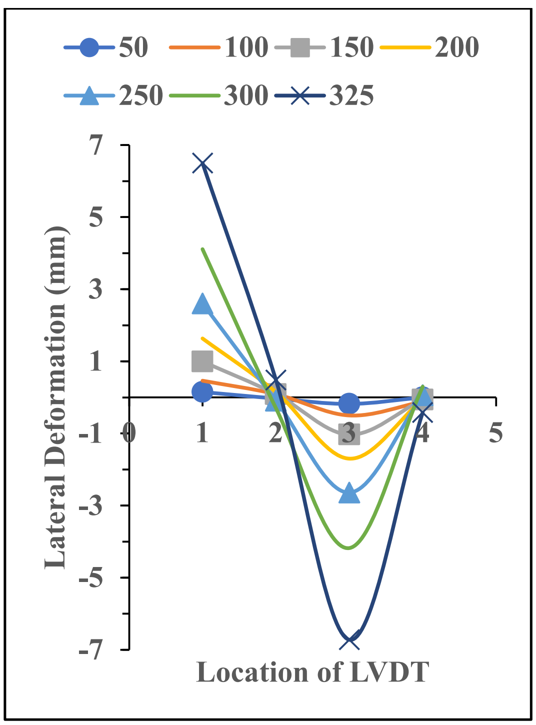

(o) 10RD2-90

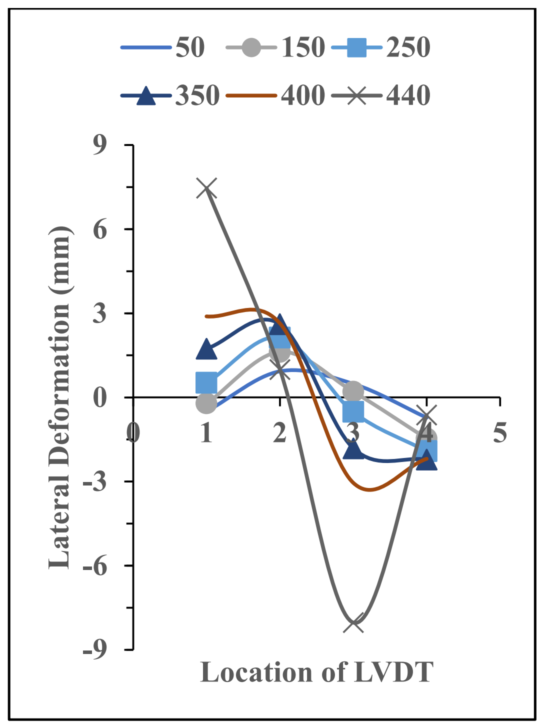

(p) 10RC2-90

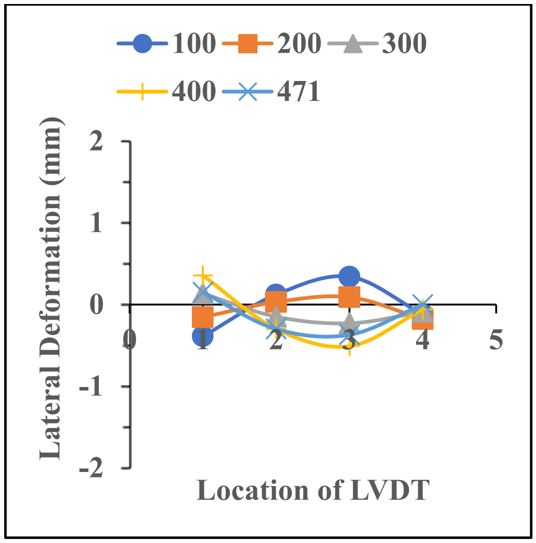

(q) 10RU1-00

Fig. D.1: Lateral deformation at the midpoint of the columns on different surfaces.

Table D.1: Lateral deformation at the midpoint of the column at peak load

S/N	Designation of column	Ppeak (kN)	Lateral deformation at mid-point (mm)				Dilation
			LVDT-1	LVDT-2	LVDT-3	LVDT-4	
1	17RW1-00	750	-5.980	-3.030	5.570	2.460	0.65%
2	17RW1-45	249	3.825	-1.080	-3.720	1.260	0.19%
3	17RD1-45	340	3.645	-0.870	-3.800	0.630	0.26%
4	17RC1-45	372	6.030	-0.600	-6.560	0.300	0.55%
5	17RW2-00	1005	1.705	-0.030	-1.950	-0.270	0.31%
6	17RW2-90	291	4.290	-2.730	-4.100	3.000	0.26%
7	17RD2-90	403	3.400	0.330	-3.320	-0.450	0.12%
8	17RC2-90	444	4.995	-0.300	-5.440	0.240	0.24%
9	10RW1-00	568	0.690	-0.030	-1.300	-2.370	2.01%
10	10RW1-45	194	0.640	-2.070	-4.840	1.890	0.25%
11	10RD1-45	299	5.090	-4.680	-5.180	4.380	0.26%
12	10RC1-45	327	6.590	-0.420	-8.410	-0.360	1.74%
13	10RW2-00	801	-4.085	0.480	3.720	-0.540	0.20%
14	10RW2-90	256	2.525	-1.290	-2.930	0.900	0.44%
15	10RD2-90	325	6.500	0.480	-6.720	-0.420	0.14%
16	10RC2-90	440	7.465	0.990	-8.030	-0.630	0.49%
17	10RU1-00	471	0.150	-0.300	-0.370	0.000	0.35%